Optical light manipulation and imaging through scattering media

Thesis by

Jian Xu

In Partial Fulfillment of the Requirements for the

Degree of

Doctor of Philosophy

CALIFORNIA INSTITUTE OF TECHNOLOGY

Pasadena, California

2020

Defended September 2, 2020

Jian Xu
ORCID: 0000-0002-4743-2471

ACKNOWLEDGEMENTS

Foremost, I would like to express my sincere thanks to my advisor Prof. Changhuei Yang, for his constant support and guidance during my PhD journey. He created a research environment with a high degree of freedom and encouraged me to explore fields with a lot of unknowns. From his ethics of research, I learned how to be a great scientist and how to do independent research. I also benefited greatly from his high standards and rigorous attitude towards work, with which I will keep in my future path.

My committee members, Professor Andrei Faraon, Professor Yanbei Chen, and Professor Palghat P. Vaidyanathan, were extremely supportive. I am grateful for the collaboration and research support from Professor Andrei Faraon and his group, the helpful discussions in optics and statistics with Professor Yanbei Chen, and the great courses and solid knowledge of signal processing from Professor Palghat P. Vaidyanathan.

I would also like to thank the members from our lab. Dr. Haojiang Zhou introduced me to the wavefront shaping field and taught me a lot of background knowledge when I was totally unfamiliar with the field. Dr. Haowen Ruan shared many innovative ideas and designs with me, from which I could understand the research field from a unique perspective. Dr. Yan Liu provided me with enormous help and advice in research and scientific writing, which benefited me throughout my PhD journey. The training experiments together with Prof. Yidong Tan in my first few months in the lab built up my experimental skills. The close collaboration with Dr. Joshua Brake, Dr. Ali Jahromi, Michelle Cua, Ruizhi Cao and Mingshu Liang made many projects progress smoothly. I also thank other lab members for providing their valuable knowledge, technical help, suggestions, and critiques to me: Dr. Atsushi Shibukawa, Hangwen Lu, Dr. Jaebum Chung, Daniel Martin, Dr. Jinho Kim, Dr. Chi Shing (Antony) Chan, Dr. Baptiste Blochet, Cheng Shen, Dr. An Pan, Chao Qian, Yujia Huang, Changsoon Choi, Dr. Xiaoyu Lyu, Dr. Liheng Bian, and Frédéric de Goumoëns. I would especially like to thank Anne Sullivan for her help with ordering lab stuff and organizing the group operations.

People from outside the lab also offered me much help in research from different perspectives. I would like to thank Dr. Anatoly Khina, Peida Tian, Jin Sima, Dr. Yiqiu Ma, Fengyu Zhou, and Chen Liang for sharing with me their knowledge

of statistics, signal processing, information theory, mathematical optimization, and physics.

I also thank all my friends who make my life in Southern California colorful and enjoyable. Badminton, hiking, road trips, and other fun activities are also important components of my PhD life.

Finally, I want to express my sincerest gratitude to my family for their constant and unconditional love, supports and understanding throughout the years.

ABSTRACT

Typical optical systems are designed to be implemented in free space or clean media. However, the presence of optical scattering media scrambles light waves and becomes a problem in light field control, optical imaging, and sensing.

To address the problem caused by optical scattering media, we discuss two types of solutions in this thesis. One type of solution is active control, where active modulators are used to modulate the light wave to compensate the wave distortion caused by optical scattering. The other type of solution is computational optics, where physical and mathematical models are built to computationally reconstruct the information from the measured distorted wavefront.

In the part of active control, we first demonstrate coherent light focusing through scattering media by transmission matrix inversion. The transmission matrix inversion approach can realize coherent light control through scattering media with higher fidelity compared to conventional transmission matrix approaches. Then, by combining the pre-designed scattering metasurface with wavefront shaping, we demonstrate a beam steering system with large angular and high angular resolution. Next, we present optical-channel-based intensity streaming (OCIS), which uses only intensity information of light fields to realize light control through scattering media. This solution can be used to control spatially incoherent light propagating through scattering media. In the part of computational optics, we first demonstrate the idea of interferometric speckle visibility spectroscopy (ISVS) to measure the information cerebral blood flow. In ISVS, a camera records the speckle frames of diffused light from the human subject interferometrically, and the speckle statistics is used to calculate the speckle decorrelation time and consequently the blood flow index. Then, we compare the two methods of decorrelation time measurements - temporal sampling methods and spatial ensemble methods - and derive unified mathematical expressions for them in terms of measurement accuracy. Based on current technology of camera sensors and single detectors, our results indicate that spatial ensemble methods can have higher decorrelation time measurement accuracy compared to commonly used temporal sampling methods.

PUBLISHED CONTENT AND CONTRIBUTIONS

[1] Haowen Ruan[†], Jian Xu[†], and Changhuei Yang. Controlling light through complex scattering media with optical-channel-based intensity streaming. *Submitted to Nature Communications*.
[†] indicates equal contribution. J.X. participated in designing the experiments, analyzing the results, and writing the manuscript. J.X. conducted the experiments.

[2] Jian Xu[†], Ali Jahromi[†], Joshua Brake[†], J. Elliot Robinson, and Changhuei Yang. Interferometric speckle visibility spectroscopy (isvs) for human cerebral blood flow monitoring. *Submitted to APL Photonics*.
[†] indicates equal contribution. J.X. participated in developing the theoretical models, designing the experiments, conducting the experiments, analyzing the data, and writing the manuscript.

[3] Yan Liu, Ruizhi Cao, Jian Xu, Haowen Ruan, and Changhuei Yang. Imaging through highly scattering human skulls with ultrasound-modulated optical tomography. *Optics Letters*, 45(11):2973, May 2020. doi:10.1364/ol.390920.
J.X. participated in conducting the theoretical analysis and writing the manuscript.

[4] Haowen Ruan, Yan Liu, Jian Xu, Yujia Huang, and Changhuei Yang. Fluorescence imaging through dynamic scattering media with speckle-encoded ultrasound-modulated light correlation. *Nature Photonics*, 14(8):511–516, May 2020. doi:10.1038/s41566-020-0630-0.
J.X. participated in conducting the theoretical analysis and writing the manuscript.

[5] Jian Xu, Ruizhi Cao, Michelle Cua, and Changhuei Yang. Single-shot surface 3d imaging by optical coherence factor. *Optics Letters*, 45(7):1734, March 2020. doi:10.1364/ol.384551.
J.X. conceived the project, designed and conducted the experiments, analyzed the results, and wrote the manuscript.

[6] Jian Xu, Michelle Cua, Edward Haojiang Zhou, Yu Horie, Andrei Faraon, and Changhuei Yang. Wide-angular-range and high-resolution beam steering by a metasurface-coupled phased array. *Optics Letters*, 43(21):5255, October 2018. doi:10.1364/ol.43.005255.
J.X. participated in the conception of the project. J.X. designed and conducted the experiments, analyzed the results, and wrote the manuscript.

[7] Jian Xu, Haowen Ruan, Yan Liu, Haojiang Zhou, and Changhuei Yang. Focusing light through scattering media by transmission matrix inversion. *Optics Express*, 25(22):27234, October 2017. doi:10.1364/oe.25.027234.
J.X. conceived the project, designed and conducted the experiments, analyzed the results, and wrote the manuscript.

TABLE OF CONTENTS

LIST OF ILLUSTRATIONS

LIST OF TABLES

Chapter 1

INTRODUCTION

Optics have accompanied human beings for a long time. From copper mirrors thousands of years ago, to simple lenses and prisms a few hundred years ago, until microscopy, photography, and lithography systems nowadays, optical systems have experienced a great evolution. Most of the above mentioned systems are designed for free space or clear media. In other words, typically there is no scatterer in between the optical system and the target, and light travels along straight lines between them.

However, as optical systems are implemented in broader areas, the presence of scattering media breaks the free space or clear media assumption. For instance, when driving in a foggy day, the object from far away cannot be seen clearly. This is because the light is scattered by the fog particles in between our eyes and the object, and no longer follows the straight line propagation in certain levels. In fact, the fog particle here is a type of scattering medium that prevents the optical system from imaging the object correctly. This light scattering problem actually exists in many research and engineering areas, such as deep tissue imaging, remote sensing, and astronomy.

In this chapter, we will discuss the physics of light, the phenomena of optical scattering, the mathematical models, as well as the engineering approaches to overcome the problems caused by optical scattering media.

We first discuss the physics of light in two perspectives: classical Maxwell's equations and quantum optics. The Maxwell's equations describe the light propagation, while the quantum optics describe the quantum nature of photons. We then discuss the temporal coherence and spatial coherence of light. Next, we discuss the interaction between light and scattering media in two manners, absorption and scattering. The scattered light consequently generates the scattered light patterns with certain statistical properties, termed speckle patterns. After that, we introduce the transmission matrix theory for modeling the input-output relation of light propagating through scattering media. Based on the transmission matrix, optical wavefront shaping can be used to control light propagation through or inside scattering media. Light propagation inside scattering media can also be modeled by the diffusion equation, and it has broad applications especially when transmission matrix char-

acterization is not applicable. Finally, we discuss the case where the scattering medium is dynamic and introduce corresponding models to describe the dynamic case.

1.1 Maxwell's equations

Maxwell's equations are a set of partial differential equations that provide a mathematical model for electromagnetic fields. For the elctromagnetic waves in free space or clear media, the space-time coupled equation set has the following expressions [1]:

$$\begin{aligned} \nabla \cdot \mathbf{E} &= 0, \\ \nabla \cdot \mathbf{B} &= 0, \\ \nabla \times \mathbf{E} &= -\frac{\partial \mathbf{B}}{\partial t}, \\ \nabla \times \mathbf{B} &= -\mu\epsilon \frac{\partial \mathbf{E}}{\partial t}, \end{aligned} \tag{1.1}$$

where t is the time variable, $\mathbf{E}$ is the electric field, $\mathbf{B}$ is the magnetic field, and ϵ and μ are the permittivity and permeability of the media.

By using the curl of curl identity $\nabla \times (\nabla \times \mathbf{E}) = \nabla(\nabla \cdot \mathbf{E}) - \nabla^2 \mathbf{E}$, we can obtain the wave equation for the electrical field:

$$\nabla^2 \mathbf{E} = \mu\epsilon \frac{\partial^2 \mathbf{E}}{\partial t^2} = \frac{1}{v^2} \frac{\partial^2 \mathbf{E}}{\partial t^2}, \tag{1.2}$$

where $v = \frac{1}{\sqrt{\mu\epsilon}}$ is the propagation speed of the wave. Similarly, the magnetic field also follows the same wave equation. Without loosing generality, here we use the electric field to represent the electromagnetic waves.

Since the different components of $\mathbf{E}$ (i.e. E_x, E_y, and E_z) are not coupled, the wave equations can be expressed by a complex scalar function $\psi(\mathbf{r}, t)$ which represents the components of $\mathbf{E}$:

$$\nabla^2 \psi(\mathbf{r}, t) = \frac{1}{v^2} \frac{\partial^2 \psi(\mathbf{r}, t)}{\partial t^2}. \tag{1.3}$$

Assuming that the wave function $\psi(\mathbf{r}, t)$ is time-harmonic, we have $\psi(\mathbf{r}, t) = A(\mathbf{r}) e^{i\omega t}$, where $A(\mathbf{r})$ is the amplitude of the wave function, and ω is the frequency of the wave function. Then, we obtain the Helmholtz equation:

$$\nabla^2 A(\mathbf{r}) + k^2 A(\mathbf{r}) = 0, \tag{1.4}$$

where $k = \omega / v$. From the structure of the Helmholtz equation, we can easily obtain the eigen solution (plane wave solution) of Eq. 1.3:

$$\psi(\mathbf{r}, t) = A_{\mathbf{k}} e^{i(\omega t - \mathbf{k} \cdot \mathbf{r})}, \tag{1.5}$$

where $\mathbf{k}$ is the wave vector of the plane wave and it follows $|\mathbf{k}| = k$, and $A_{\mathbf{k}}$ is the amplitude of the plane wave. The amplitude $A_{\mathbf{k}}$ is determined by the initial values and the boundary condition of the physical system. Therefore, given the initial values and boundary condition of a physical system, we can decompose the electromagnetic wave into the plane wave basis, and the wave evolution can be described analytically by propagating the different plane wave basis independently.

1.2 Quantum nature of light

In many experiments, lasers are used as light sources. The light field from lasers can be described as coherent states. A coherent state $|\alpha\rangle$ is defined as the eigenstate of the annihilation operator $\hat{a}$ with the corresponding eigenvalue α. The coherent state can be expressed as [2, 3]:

$$|\alpha\rangle = e^{-\frac{1}{2}|\alpha|^2} \sum_{n=0}^{\infty} \frac{\alpha^n}{\sqrt{n!}} |n\rangle \,, \tag{1.6}$$

with α a complex number. Here, $|n\rangle$ is the energy eigenstate of the Hamiltonian $H = \hbar\omega(\hat{a}^\dagger\hat{a} + \frac{1}{2})$, where $\hbar$ is the reduced Planck constant, $\dagger$ denotes the Hermitian transpose, and ω is the angular frequency of the photon. Therefore, the probability of finding a certain photon numbers in the coherent state $|\alpha\rangle$ follows Poisson distribution:

$$P(n) = |\langle n|\alpha\rangle|^2 = e^{-|\alpha|^2} \frac{|\alpha|^{2n}}{n!}. \tag{1.7}$$

The average photon number $\langle n\rangle$ in a coherent state is

$$\langle n\rangle = \langle \hat{a}^\dagger\hat{a}\rangle = |\alpha|^2, \tag{1.8}$$

and the variance $(\Delta n)^2$ is

$$(\Delta n)^2 = \langle \hat{a}^\dagger\hat{a}\hat{a}^\dagger\hat{a}\rangle - \langle \hat{a}^\dagger\hat{a}\rangle^2 = |\alpha|^2. \tag{1.9}$$

The Δn term sometimes is termed shot noise. It describes the statistical uncertainty of the number of photons in a coherent state. For a given coherent state with the average photon number $\langle n\rangle$, the ideal measurement signal-to-noise ratio (SNR) of the average number of photons is

$$SNR = \frac{\langle n\rangle}{\sqrt{(\Delta n)^2}} = \sqrt{\langle n\rangle}. \tag{1.10}$$

This implies that the measurement SNR is scaling up with the average number of photons in a square root relationship. A larger average number of photons can yield a higher measurement SNR of the average number of photons.

1.3 Temporal coherence and spatial coherence

In practice, light waves may not be strictly monochromatic, and the phase difference at different locations may not be a constant. Hence temporal coherence and spatial coherence are introduced to quantify the properties of light waves.

In optics, the degree of coherence is typically quantified by the correlation coefficient Γ of two electric fields, which is defined as

$$\Gamma = \frac{\langle E_1 E_2^* \rangle}{\sqrt{\langle |E_1|^2 \rangle \langle |E_2|^2 \rangle}}, \tag{1.11}$$

where E_1 and E_2 are the electric fields, and $\langle \cdot \rangle$ is the expected value operator. Temporal coherence and spatial coherence investigate Eq. 1.11 from two perspectives - time domain and spatial domain.

Temporal coherence can be described by the autocorrelation function $\Gamma(\tau)$ of an optical wave $E(t)$ with respect to time delay Δt, i.e.,

$$\Gamma(\Delta t) = \frac{\langle E(t)E(t+\Delta t)^* \rangle}{\sqrt{\langle |E(t)|^2 \rangle \langle |E(t+\Delta t)|^2 \rangle}} = \frac{\langle E(t)E(t+\Delta t)^* \rangle}{\langle |E(t)|^2 \rangle}, \tag{1.12}$$

where E_1 and E_2 in Eq. 1.11 are replaced by $E(t)$ and $E(t+\Delta t)$. $\Gamma(\Delta t)$ usually has a shape similar to a bell shaped curve, with $\Gamma(0) = 1$ and gradually decreasing to 0 as $|\Delta t|$ increases. Coherence time τ_c is defined as the time delay over which $\Gamma(\Delta t)$ drops below a specific value, such as $1/e$. In practice, coherence length $l_c = c\tau_c$ is more commonly used. From a physics perspective, l_c gives an intuitive sense of how long the wave packet is. If the wave packets have relative delays less than l_c, they can interfere with each other and provide high contrast interference fringes.

Similarly, spatial coherence can be described by the autocorrelation function $\Gamma(\tau)$ of an optical wave $E(t)$ with respect to spatial shift Δr, i.e.,

$$\Gamma(\Delta r) = \frac{\langle E(r)E(r+\Delta r)^* \rangle}{\langle |E(r)|^2 \rangle}, \tag{1.13}$$

where E_1 and E_2 in Eq. 1.11 are replaced by $E(r)$ and $E(r+\Delta r)$. Typically, in a common optical system, $\Gamma(\Delta r)$ decreases from 1 to 0 as Δr increases from 0 to ∞. The coherence area A is an empirical notation within which $\Gamma(\Delta r)$ is larger than a specific threshold. From a physics perspective, coherence area A means that if points in the light field are located within the area A, they have static phase difference. Light emitting from these points can interfere with each other and provide high contrast interference fringes. The spatial coherence can vary as the light field propagates. Van Cittert–Zernike theorem [4, 5, 6] provides detailed analysis on the propagation of spatial coherence.

1.4 Light absorption

Light absorption occurs when the photon energy matches the energy spacing between different energy levels of electron-atom systems. The absorption of a bulky macroscopic material can be characterized by a coefficient termed absorption coefficient (μ_a). The light intensity I along the light propagation direction z can be quantified as [7]

$$I(z + dz) - I(z) = -\mu_a dz. \tag{1.14}$$

After mathematical derivation, Eq. 1.14 can be written as

$$I(z) = I_0 e^{-\mu_a z}, \tag{1.15}$$

where I_0 denotes the light intensity at the location of $z = 0$. Equation 1.15 is called the Beer-Lambert-Bouguer law. It indicates that the light intensity during the propagation in a loss medium follows exponential decay.

The absorption coefficient is wavelength dependent. In typical applications of biology, the absorption mostly comes from the major components of biological tissue, such as water and hemoglobin. The 650–950 nm optical window has relatively low absorption from biological tissue, and therefore enables light to penetrate tissue with less loss. Therefore, in most biomedical applications and implementations, this optical window is chosen to acquire more scattered signal light.

1.5 Light scattering – a single particle

Light scattering for a single particle can be strictly solved by Maxwell's equations. Depending on the single particle size (d) and the light wavelength (λ), light scattering can be classified in three regimes: geometrical scattering, Mie scattering, and Rayleigh scattering.

Geometrical scattering is the regime where the particle size is much greater than the light wavelength ($d >> \lambda$). In this case, geometrical light rays (reflection, refraction, and deflection) can be used to approximate the light wave function.

Mie scattering is the regime where the particle size is comparable to the light wavelength ($d \sim \lambda$). In this regime, Maxwell's equations have to be introduced and the analytical solution usually has a form of series summation, where the series basis can be Bessel functions, Hankel functions, or other functions depending on the boundary conditions. Typically, the Mie scattering light energy is proportional to the square of the particle diameter. It should be noted that Mie theory is referred to a collection of solutions, rather than a specific analytical form.

Rayleigh scattering is the regime where the particle size is much smaller than the light wavelength ($d << \lambda$). In this situation, there is a closed form solution to the angular light intensity distribution $I(r, \theta)$ [7, 8]:

$$I(r,\theta) = I_0 \frac{1+\cos^2\theta}{2r^2}(\frac{2\pi}{\lambda})^4(\frac{n_s^2-n_m^2}{n_s^2+2n_m^2})^2 a^6, \tag{1.16}$$

where (r, θ) is coordinate of the field position, I_0 is the light intensity of the incident plane wave, λ is the wavelength of the light, a is the radius of the scatterer, and n_s and n_m are the refractive indices of the scatterer and the background medium, respectively. The inverse dependency on λ^4 indicates preferential scattering of shorter wavelengths.

One important quantity in single particle scattering is the scattering aniostropy factor g, which is defined as [7]

$$g = \int_0^\pi p(\theta) 2\pi \sin(\theta) d\theta \times \cos(\theta) = \langle \cos(\theta) \rangle . \tag{1.17}$$

Here, $p(\theta)$ is the density distribution of the scattering field with respect to scattering angle θ. Intuitively speaking, g is the weighted average of $\cos(\theta)$ with the density distribution function $p(\theta)$. For instance, in the single particle Rayleigh scattering regime, $p(\theta)$ can take the form of Eq. 1.16 with appropriate normalization.

1.6 Light scattering – a collection of particles

In real situations, light typically interacts with scattering media, e.g., light scattering happens with a collection of particles. In this case, we need to use statistical models to model the interaction between the light and the scattering media. Assuming that the light absorption is negligible, a simplified model, which contains the scattering mean free path l_s [mm] and the scattering anisotropy factor g, can be used to describe a collection of particles. Scattering mean free path l_s, or the inverse of the scattering coefficient $l_s = 1/\mu_s$, is defined as the average distance travelled by a photon between successive scattering events. By using this model, when light travels inside the scattering media along the direction z, the intensity of the light field $I(z)$ that is not scattered (called ballistic light) experiences the exponential decay [7]:

$$I(z) = I_0 e^{-\mu_s z}, \tag{1.18}$$

where I_0 is the intensity of the incident light.

However, Eq. 1.18 only models how much of the light is not scattered, but it does not depict how much of the light still follows the original direction or trajectory. For

instance, if the scattering anisotropy factor $g \approx 1$, even if the scattering happens, but it almost does not affect the propagation direction of the light. In this case, it "seems" no scattering happened. By incorporating the scattering anisotropy factor g into the scattering model, typically we use reduced scattering coefficient $\mu_s^{'}$ [mm^{-1}] or transport mean free path $l_s^{'}$ [mm] to describe the scattering media [7, 9]:

$$\mu_s^{'} = (1 - g)\mu_s, \tag{1.19a}$$

$$l^{'} = \frac{1}{\mu_s^{'}}. \tag{1.19b}$$

Equation 1.19 uses a lumped property $\mu_s^{'}$, which incorporates μ_s and g, to describe the light scattering. This equation includes the cases where photons have experience multiple scattering events, but still retain some memory of their original directionality[7].

1.7 Speckles

When monochromatic light interacts with scattering media, the scattered light field is termed speckle field. Consider a point P in the speckle field. The complex field E is the phasor summation of the exit plane of the scattering media (Fig. 1.1), according to Huygens' principle [10]:

$$E = \frac{1}{\sqrt{N}} \sum_{n=1}^{N} a_n e^{i\phi_n}. \tag{1.20}$$

Here, N denotes the number of phasor components in the phasor summation, and a_n and $e^{i\phi_n}$ denotes the amplitude and phase terms of the n-th component phasor on the exit plane, respectively. The scaling factor $\frac{1}{\sqrt{N}}$ is introduced to preserve finite second moments of the sum even when N approaches infinity. Typically, $a_n e^{i\phi_n}$ and $a_m e^{i\phi_m}$ are independent provided $n \neq m$. Therefore, if we assume that the phasor in the exit plane follows a specific distribution, the complex field E is the summation of these random variables $a_n e^{i\phi_n}$'s. The central limit theorem predicts that E follows complex normal distribution if n is large. The probablity density function $p_{R,I}(R, I)$ of the real and imaginary parts (R and I) of the complex field E has the form of [10]

$$p_{R,I}(R, I) = \frac{1}{2\pi\sigma^2} e^{-\frac{R^2+I^2}{2\sigma^2}}, \tag{1.21}$$

where σ is the standard deviation.

Of equal interest are the statistics of the amplitude A and phase θ of the complex field E. The joint distribution of A and θ can be derived from the theory of variable

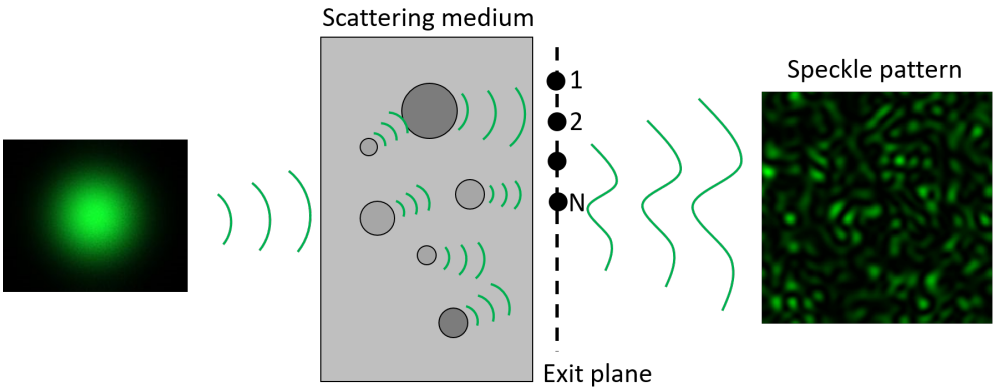

Figure 1.1: Light propagation through a scattering medium.

transformation

$$A = \sqrt{R^2 + I^2}, \tag{1.22a}$$

$$\theta = \arctan(\frac{I}{R}), \tag{1.22b}$$

and

$$R = A\cos\theta, \tag{1.23a}$$

$$I = A\sin\theta. \tag{1.23b}$$

The joint distribution of A and θ then follows

$$\begin{cases} p_A(A) = \frac{A}{2\sigma^2} e^{-\frac{A}{2\sigma^2}}, & A \geq 0, \\ p_\theta(\theta) = \frac{1}{2\pi}, & 0 \leq \theta \leq 2\pi. \end{cases} \tag{1.24}$$

If A and θ do not fall in the range in the above equation, the probability density is zero.

1.8 Transmission matrix

Since Maxwell's equations are linear equations with respect to electric and magnetic fields, if the boundary conditions are also linear (ϵ and μ in Eq. 1.1 are not dependent on **E** and **B**), the interaction between light and scattering media will be a linear process. Therefore, a scattering medium is a linear system that transforms the input light field to the output light field. For a given deterministic linear system (scattering medium in this case), we can model it by using a matrix. Here, the matrix is termed transmission matrix T, which builds the mapping between the input light field (E_{in}) and output light field (E_{out}).

In Fig. 1.2, suppose the incident light field E_a located at plane a can be decomposed into n modes (the modes can be in spatial domain, spatial frequency domain, etc), and the output light field E_b located at plane b can be decomposed into m modes. The transmission matrix T_{ab} is then an $m \times n$ matrix, and it relates E_a and E_b as follows [11, 12, 13]:

$$E_b = T_{ab} E_a, \tag{1.25}$$

$$\begin{bmatrix} E_{b,1} \\ E_{b,2} \\ \dots \\ E_{b,m} \end{bmatrix} = \begin{bmatrix} t_{11} & t_{12} & \dots & t_{1n} \\ \dots & & & \dots \\ t_{m1} & t_{m2} & \dots & t_{mn} \end{bmatrix} \begin{bmatrix} E_{a,1} \\ E_{a,2} \\ \dots \\ E_{a,n} \end{bmatrix}. \tag{1.26}$$

Equation 1.26 is the detailed expression of Eq. 1.25.

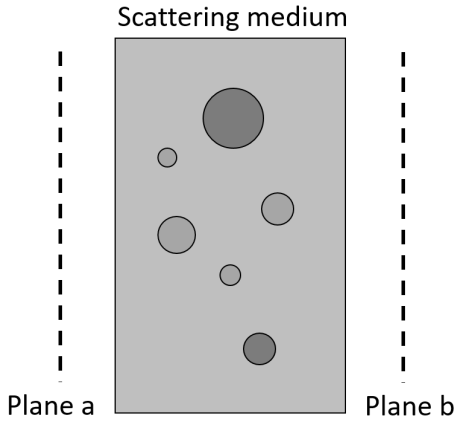

Figure 1.2: The schematic of Plane a and Plane b at the two sides of the scattering medium.

It is of similar importance to know the transmission matrix T_{ba} if the incident light field is at plane b and the output light field is at plane a. The principle of optical reciprocity ensures that $T_{ba} = T_{ab}^T$, where $(\cdot)^T$ denotes the matrix transpose.

If the scattering medium is lossless, both transmission matrices T_{ab} and T_{ba} are unitary, i.e.,

$$T_{ab}^\dagger T_{ab} = I_n, \tag{1.27a}$$

$$T_{ba}^\dagger T_{ba} = I_m. \tag{1.27b}$$

Here, I_n denotes an $n \times n$ identity matrix, and $(\cdot)^\dagger$ denotes the Hermitian transpose.

If we use the reciprocity property $T_{ba} = T_{ab}^T$ together with unitary condition in Eq. 1.27, we will have

$$T_{ba}^* T_{ab} = I_n, \tag{1.28}$$

where $(\cdot)^*$ denotes the conjugate operator. Equation 1.28 is actually the principle of time reversal in electromagnetic waves. A more intuitive explanation can be seen as follows. Assume that an incident field E_a on plane a is illuminating the scattering medium, then E_a^* is the phase conjugated field of E_a. Multiplying E_a on both sides of Eq. 1.28, and taking phase conjugate of both sides, we have

$$\begin{aligned} & (T_{ba}^* T_{ab} E_a)^* = (I_n E_a)^*, \\ \Leftrightarrow \quad & T_{ba} T_{ab}^* E_a^* = E_a^*, \\ \Leftrightarrow \quad & T_{ba} E_b^* = E_a^*. \end{aligned} \tag{1.29}$$

The last line in Eq. 1.29 shows that a phase conjugated field E_b will result in the phase conjugated field E_a after the light field is reversely propagating through the scattering medium.

The above derivation assumes that we have full access to both of the incident field E_a and the output field E_b. Practically, we can only have access to part of the modes of the incident field E_a and the output field E_b. The part of modes that is not accessible can be treated as loss. In this case, the unitary assumption of transmission matrices does not hold, and the time reversal relation in Eq. 1.28 should not be valid either. However, when light propagates through scattering media and some modes are lost, interestingly, the time reversal still approximately holds, i.e.,

$$T_{ba}^* T_{ab} \approx \alpha I_n, \tag{1.30}$$

where α is a normalization constant. This relation can be derived only based on the optical reciprocity and the statistical distribution of the matrix entries, without the unitary assumption.

The derivation of Eq. 1.30 can be seen as follows. Equation 1.21 indicates that the real and imaginary parts of the output field of the light that is scattered by scattering media follows Gaussian distribution, therefore the entries in each column of transmission matrices (Eq. 1.26) follow complex Gaussian distribution [10]. Hence, all the entries in transmission matrices follow complex Gaussian distribution. If we define the matrix O as $O = T_{ba}^* T_{ab}$, the i, j-th entry of O is equal to

$$o_{ij} = \sum_{k=1}^{m} t_{ki}^* t_{kj}. \tag{1.31}$$

Since t_{ki} and t_{kj} follow complex Gaussian distribution, only when $i = j$, o_{ij} has a positive expected value; if $i \neq j$, the expected value of o_{ij} is 0. Therefore, the diagonal entries of O have positive expected values, and the off diagonal entries have expected values of 0. This implies that $O = T^*_{ba} T_{ab} \approx \alpha I_n$.

1.9 Optical wavefront shaping

Optical wavefront shaping is an approach to control the light propagation through or inside scattering media. Based on the transmission matrix according to the scattering medium, corresponding wavefront can be calculated for creating specific patterns through or inside the scattering medium. Optical wavefront shaping can be realized by spatial light modulators (SLM). SLM can impose spatially varying modulation on the incident wave, where the modulation can act on amplitude, phase, and polarization. Typical SLM devices include liquid crystal cell arrays, digital micromirror devices (DMD), and deformable mirrors. In this section, we will focus more on liquid crystal cell arrays for phase modulation and DMD for amplitude modulation.

Typical architectures of liquid crystal cell arrays used in optical wavefront shaping adopt smectic liquid crystals [14]. In such arrangement, the orientation of liquid crystal molecules can be driven by external electric fields. If the liquid crystal molecules are uniaxial crystals or biaxial crystals, this property can be used to control the phase retardance of the transmitted light. More specifically, assume that the liquid crystal molecules are uniaxial and the incident light has the polarization aligning with the long axis of the molecules. If the external electric is applied to rotate the orientation of the molecules, and the final state of the molecules have short axis aligning with the polarization of the light, then the optical path length of the transmitted light is changed by $(n_l - n_s)d$, where n_l is the refractive index of the long axis, n_s is the refractive index of the short axis and d is the thickness of the crystal cell. The liquid crystal cells can be designed to let the molecules have continuous rotating angles, therefore the phase retardance can be designed to range from 0 to 2π. A 2D array of such cells can be aggregated to form a phase-modulated spatial light modulator.

DMD is fully integrated and monolithically fabricated on a mature SRAM CMOS address circuitry [15]. It consists of a 2D array of micromirrors, where each micromirror is attached to the torsional hinge aligned along the diagonal of the mirror. After applying electrostatic forces, each micromirror has two static tilted

angles (typically +10° and -10°). If the DMD is aligned accordingly in the optical system, the two static tilted angles of each micromirror can correspond to ON and OFF states. Therefore, DMD can be used as an amplitude modulation SLM. Since it is an MEMS device and each micromirror has small inertia, the refresh speed of DMD can achieve 23 kHz [16], which is significantly faster than conventional liquid crystal SLM.

1.10 Light diffusion in scattering media

The characterization of transmission matrix for scattering media requires access to both the input plane and output plane. This access is not always allowed in practice. For instance, when doing in vivo biomedical experiments (the scattering medium is biomedical tissue), we typically cannot access the plane inside the biomedical tissue. Estimating the light intensity distribution inside scattering media is of essence in such applications. Therefore, it is important to know how light diffuses into scattering media.

The diffusion equation, which is derived from the radiative transfer function, can be used to describe light diffusion in scattering media [7]:

$$\frac{\partial \Phi(\mathbf{r},t)}{c\partial t} + \mu_a \Phi(\mathbf{r},t) - D\nabla^2 \Phi(\mathbf{r},t) = S(\mathbf{r},t), \tag{1.32}$$

where $\Phi(\mathbf{r},t)$ denotes the fluence rate (intensity) at location $\mathbf{r}$ and time t, μ_a denotes the absorption coefficient of the medium, $S(\mathbf{r},t)$ denotes the isotropic source of photons at location $\mathbf{r}$ and time t, and D denotes the diffusion coefficient with $D = 1/(3\mu_a + 3\mu_s^{'})$. Here, $\mu_s^{'}$ is the reduced scattering coefficient mentioned in section 1.6, with $\mu_s^{'} = \mu_s/(1-g)$, where g is the scattering aniostropy factor.

For an infinitely short point source $S(\mathbf{r},t) = \delta(\mathbf{r},t)$, the impulse response of Eq. 1.32 is

$$\Phi(\mathbf{r},t) = \frac{c}{(4\pi Dct)^{3/2}} \exp(-\frac{r^2}{4Dct} - \mu_a ct),\ t > 0. \tag{1.33}$$

If the source is time-independent, the term $\frac{\partial \Phi(\mathbf{r},t)}{c\partial t}$ in Eq. 1.32 is zero. Equation 1.32 then degenerates to the time-independent form:

$$\Phi(\mathbf{r}) - \frac{1}{\mu_{\text{eff}}^2}\nabla^2 \Phi(\mathbf{r}) = S(\mathbf{r}), \tag{1.34}$$

where $\mu_{\text{eff}} = \sqrt{\mu_a/D} = \sqrt{3\mu_a(\mu_a + \mu_s^{'})}$ denotes the effective attenuation coefficient.

For a time-independent source $S(\mathbf{r}) = \delta(\mathbf{r})$, the impulse response of 1.34 is

$$\Phi(\mathbf{r}) = \frac{1}{4\pi Dr} \exp(-\mu_{\text{eff}}\, r). \tag{1.35}$$

Since both time-dependent and time-independent diffusion equations 1.32 and 1.34 are linear with respect to Φ, and the medium is shift-invariant, the Green function approach can be used to calculate the response of more complicated sources. For the time-dependent Eq. 1.32, the Green function has the form of

$$\Phi(\mathbf{r}, t; \mathbf{r}^{'}, t^{'}) = \frac{c}{[4\pi Dc(t-t^{'})]^{3/2}} \exp[-\frac{|\mathbf{r}-\mathbf{r}^{'}|^2}{4Dc(t-t^{'})} - \mu_a c(t-t^{'})],\ t > t^{'}. \quad (1.36)$$

Therefore, for any arbitrary source in space and time $S(\mathbf{r}_{'}, t^{'})$, the fluence distribution has the following expression:

$$\Phi(\mathbf{r}, t) = \int_0^t \int_0^\infty \Phi(\mathbf{r}, t; \mathbf{r}^{'}, t^{'}) S(\mathbf{r}_{'}, t^{'}) d\mathbf{r}^{'} dt^{'}. \quad (1.37)$$

For the time-independent Eq. 1.34, the Green function has the form of

$$\Phi(\mathbf{r}; \mathbf{r}^{'}) = \frac{1}{4\pi D|\mathbf{r}-\mathbf{r}^{'}|} \exp(-\mu_{\text{eff}}\,|\mathbf{r}-\mathbf{r}^{'}|). \quad (1.38)$$

For any arbitrary source in space $S(\mathbf{r}^{'})$, the fluence distribution has the following expression:

$$\Phi(\mathbf{r}) = \int_0^\infty \Phi(\mathbf{r}; \mathbf{r}^{'}) S(\mathbf{r}^{'}) d\mathbf{r}^{'}. \quad (1.39)$$

Based on the diffusion equation, diffuse optical tomography (DOT) has been implemented in optical imaging for biomedical tissue [17, 18]. A typical schematic of DOT is shown in Fig. 1.3. A source-detector pair is placed on the surface of the tissue. The light from the source first diffuses into the tissue and then is scattering back to the detector. Based on the light signal collected by the detector, forward models or inverse models are built to recover the tissue properties (absorption and scattering coefficients). Then, an array of such source-detector pairs are used to build a spatial map of tissue properties at different locations. The spatial resolution of such architecture is determined by the volume of the "banana shape" along which photons travel from the source to the detector. Mathematically, the point spread function (PSF) of such structure is the multiplication of the illumination PSF and the detection PSF. The detailed expression of the illumination PSF (detection PSF only has a lateral shift) can be found in Ref. [19]. Figure 1.3 gives an example of architecture with the source-detector separation of $2cm$, $\mu_a = 0.025cm^{-1}$, $\mu_s^{'} = 10cm^{-1}$, and tissue refractive index $n = 1.33$. As a rule of thumb, the spatial resolution of DOT is about 20% of the light penetration depth δ ($\delta = 1/\mu_a$) [7]. The mean photon-visited depth is about $\sqrt{\rho\delta}/2$, where ρ is the source-detector separation [20]. Experimentally, the penetration depth of photons can reach centimeters

[7], but the spatial resolution is rather modest. Despite the relatively modest spatial resolution, the inherent non-invasive, radiation free, and portable properties make it useful in biomedical areas such as brain imaging [21] and tumor imaging [22].

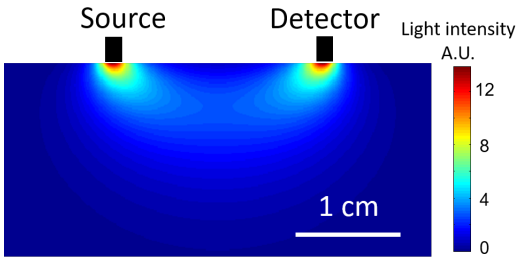

Figure 1.3: A typical configuration of a DOT setup.

1.11 Decorrelation

The preceding discussions assume that the scattering medium is static. In practice, many scattering media are dynamic, such as blood flow in tissue, particles in fluids with Brownian motions, etc. In such cases, if the illumination light on the scattering sample is coherent, the output light field will be a dynamic speckle field. The change of the output speckle field can be described as a decorrelation process, and this process can be quantified by complex field correlation function $G_1(t)$ [23]:

$$G_1(t) = \langle E(0)E(t)^* \rangle , \tag{1.40}$$

where $\langle \cdot \rangle$ denotes the expected value. Since common photo detectors measure the light intensity ($\propto |E|^2$) instead of the light field, the intensity correlation function $G_2(t)$ is

$$G_2(t) = \langle I(0)I(t) \rangle . \tag{1.41}$$

The Siegert relation can be used to relate $G_1(t)$ and $G_2(t)$, if the dynamic output light field at each point follows complex Gaussian distribution. The Siegert relation has the form [23, 24] of

$$G_2(t) = \langle I \rangle + \beta |G_1(t)|^2, \tag{1.42}$$

where β is a parameter which depends on the number of speckles detected and the coherence length and stability of the laser. In the ideal case, $\beta = 1$.

The normalized correlation functions are more common in experimental conditions, since they remove the information of the absolute light intensity and only leave the relative change. The normalized field correlation function $g_1(t)$ and intensity

correlation function $g_2(t)$ are defined as

$$g_1(t) = \frac{\langle E(0)E(t)^* \rangle}{\langle |E(0)|^2 \rangle} \tag{1.43}$$

and

$$g_2(t) = \frac{\langle I(0)I(t) \rangle}{\langle I(0) \rangle^2}. \tag{1.44}$$

Similarly, the Siegert relation of the normalized correlation functions reads as

$$g_2(t) = 1 + \beta |g_1(t)|^2. \tag{1.45}$$

For ideal cases, $g_1(0) = 1$ and $g_1(\infty) = 0$, while $g_2(0) = 2$ and $g_2(\infty) = 1$. The time scale of the decorrelation can be quantified by decorrelation time, which is defined as the time instant where the correlation function $g_1(t)$ drops to a specific value.

Decorrelation plays a subtle role in light control and imaging with scattering media. Sometimes it hinders applications, while sometimes it is helpful for applications. In light field control, we use transmission matrix to describe the scattering medium, and we typically first characterize the transmission matrix and then use the information of the matrix to realize light field control. In this case, decorrelation raises the requirement of running speed of transmission matrix characterization and light field control, since within the decorrelation time the characterized transmission matrix should still be valid for light control. In optical imaging and sensing through scattering media, the decorrelation time itself is an indicator of the dynamic scattering media. For instance, in dynamic light scattering, people use the decorrelation time to infer the information of blood flow [25] and air turbulence [26].

Outline of this thesis

This thesis discusses light control and light detection through scattering media. In Chapter 2, we investigate the transmission matrix inversion approach to realize coherent light control through scattering media. In Chapter 3, we use a pre-designed scattering medium - scattering metasurface - to realize large angular range and high resolution beam steering. In Chapter 4, we investigate the method of optical-channel-based intensity streaming (OCIS), which can be used for incoherent light control through scattering media. In Chapter 5, we present a method termed interferometric speckle visibility spectroscopy (ISVS) to quantify the decorrelation time of dynamic scattered light, and we implement the ISVS method to measure the human cerebral blood flow. In Chapter 6, we perform unified analysis of two methods that are

traditionally used to quantify the decorrelation time of dynamic scattered light, and demonstrate their equivalence in terms of the measurement accuracy.

References

[1] Max Born, Emil Wolf, and et al. *Principles of Optics : Electromagnetic Theory of Propagation, Interference and Diffraction of Light*. Cambridge University Press, 7th expanded edition, 1999.

[2] Rodney Loudon. *The Quantum Theory of Light, 3rd ed. (Oxford Science Publications)*. Oxford University Press, USA, 3rd edition, 2000.

[3] D. F. Walls and G. J. Milburn. *Quantum Optics*. Springer, 1994.

[4] P. H van Cittert. Die wahrscheinliche schwingungsverteilung in einer von einer lichtquelle direkt oder mittels einer linse beleuchteten ebene. *Physica*, 1(1-6):201–210, January 1934.

[5] F. Zernike. The concept of degree of coherence and its application to optical problems. *Physica*, 5(8):785–795, August 1938.

[6] Joseph W. Goodman. *Statistical Optics*. Wiley-Interscience, 1st edition, 1985.

[7] Lihong V. Wang and Hsin-I Wu. *Biomedical Optics: Principles and Imaging*. Wiley, John & Sons, Incorporated, 2007.

[8] Craig F. Bohren and Donald R. Huffman. *Absorption and Scattering of Light by Small Particles*. Wiley Science Paperback Series. Wiley-VCH, 1998.

[9] Vasilis Ntziachristos. Going deeper than microscopy: the optical imaging frontier in biology. *Nature Methods*, 7(8):603–614, July 2010.

[10] Joseph W. Goodman. *Speckle Phenomena in Optics*. Viva Books Private Limited, 2008.

[11] I. M. Vellekoop. *Controlling the propagation of light in disordered scattering media*. PhD thesis, University of Twente, 2008.

[12] I. M. Vellekoop and A. P. Mosk. Focusing coherent light through opaque strongly scattering media. *Optics Letters*, 32(16):2309, August 2007.

[13] S. M. Popoff, G. Lerosey, R. Carminati, M. Fink, A. C. Boccara, and S. Gigan. Measuring the transmission matrix in optics: an approach to the study and control of light propagation in disordered media. *Physical Review Letters*, 104(10), March 2010.

[14] L. Vicari. *Optical Applications of Liquid Crystals*. Series in Optics and Optoelectronics. Taylor & Francis, 1st edition, 2003.

[15] P. Rai-Choudhury. *MEMS and MOEMS Technology and Applications*, volume 85. SPIE Press, 2000.

[16] Dana Dudley, Walter M. Duncan, and John Slaughter. Emerging digital micromirror device (DMD) applications. In Hakan Urey, editor, *MOEMS Display and Imaging Systems*. SPIE, January 2003.

[17] D. A. Boas, D. H. Brooks, E. L. Miller, C. A. DiMarzio, M. Kilmer, R. J. Gaudette, and Quan Zhang. Imaging the body with diffuse optical tomography. *IEEE Signal Processing Magazine*, 18(6):57–75, 2001.

[18] Joseph P. Culver, Andrew M. Siegel, Jonathan J. Stott, and David A. Boas. Volumetric diffuse optical tomography of brain activity. *Optics Letters*, 28(21):2061, November 2003.

[19] T. Durduran, R. Choe, W. B. Baker, and A. G. Yodh. Diffuse optics for tissue monitoring and tomography. *Reports on Progress in Physics*, 73(7):076701, June 2010.

[20] Michael S. Patterson, Stefan Andersson-Engels, Brian C. Wilson, and Ernest K. Osei. Absorption spectroscopy in tissue-simulating materials: a theoretical and experimental study of photon paths. *Applied Optics*, 34(1):22, January 1995.

[21] David A. Boas, Anders M. Dale, and Maria Angela Franceschini. Diffuse optical imaging of brain activation: approaches to optimizing image sensitivity, resolution, and accuracy. *NeuroImage*, 23:S275–S288, January 2004.

[22] Bruce J. Tromberg, Brian W. Pogue, Keith D. Paulsen, Arjun G. Yodh, David A. Boas, and Albert E. Cerussi. Assessing the future of diffuse optical imaging technologies for breast cancer management. *Medical Physics*, 35(6Part1):2443–2451, May 2008.

[23] David A. Boas. *Diffuse photon probes of structural and dynamical properties of turbid media: Theory and biomedical applications*. PhD thesis, University of Pennsylvania, 1996.

[24] A. J. F. Siegert. On the fluctuations in signals returned by many independently moving scatterers, Radiation Laboratory, Massachusetts Institute of Technology, 1943.

[25] Turgut Durduran and Arjun G. Yodh. Diffuse correlation spectroscopy for non-invasive, micro-vascular cerebral blood flow measurement. *NeuroImage*, 85:51–63, January 2014.

[26] Gerard M. Ancellet and Robert T. Menzies. Atmospheric correlation-time measurements and effects on coherent doppler lidar. *Journal of the Optical Society of America A*, 4(2):367, February 1987.

Chapter 2

FOCUSING LIGHT THROUGH SCATTERING MEDIA BY TRANSMISSION MATRIX INVERSION

Focusing light through scattering media has broad applications in optical imaging, manipulation, and therapy. The contrast of the focus can be quantified by peak-to-background intensity ratio (PBR). Here, we theoretically and numerically show that by using a transmission matrix inversion method to achieve focusing, within a limited field of view and under a low noise condition in transmission matrix measurements, the PBR of the focus can be higher than that achieved by conventional methods such as optical phase conjugation or feedback-based wavefront shaping. Experimentally, using a phase-modulation spatial light modulator, we increase the PBR by 66% over that achieved by conventional methods based on phase conjugation. In addition, we demonstrate that, within a limited field of view and under a low noise condition in transmission matrix measurements, our matrix inversion method enables light focusing to multiple foci with greater fidelity than those of conventional methods.

2.1 Introduction

Focusing light through scattering media has broad applications in areas such as biomedical imaging [1, 2, 3, 4], cell cytometry [5], optogenetics [6, 7], and photodynamic therapy [8]. However, because of the refractive index inhomogeneity, light is scattered when propagating through scattering media. To focus light through such turbid media, researchers have developed a number of wavefront shaping techniques, including feedback-based methods [9, 10], optical phase conjugation [11, 12, 13, 14], and transmission matrix methods [15, 16, 17, 18]. Feedback-based methods employ a spatial light modulator (SLM) to continuously shape the wavefront of the incident light while monitoring the feedback signal from a guidestar which is proportional to the light intensity at a target location. In this way, an optimum wavefront can be obtained to maximize the light intensity at the target location to form an optical focus. Optical phase conjugation methods achieve light focusing by phase conjugating the scattering light field emitted from a guidestar [19] located at the target location. Traditionally, transmission matrix methods first measure the scattered light fields corresponding to different incident light fields (i.e. measure the transmission matrix), and then realize focusing by sending an appropriate incident

field which is proportional to the linear combination of the columns of the transpose conjugation of the measured transmission matrix.

To focus light through scattering media, wavefront shaping methods typically use an SLM to increase the light intensity at the target location. This strategy is fundamentally tied to the concept of phase conjugation, i.e., using the finite elements of the SLM to align the phase of the incident wavefront to increase the intensity at the target location. Typically, the number of optical modes of the scattered light field is larger than the number of controllable elements on the SLM. Therefore, one can only partially conjugate the correct wavefront solution, which leads to a non-zero background surrounding the focus. The contrast of the focus can be quantified by a peak-background ratio (PBR), which is the ratio between the intensity of the focus and the average intensity of the background surrounding the focus. We note that our definition of PBR is different from the conventional wavefront shaping definition of PBR, which is the ratio between the focus intensity and the average intensity before wavefront shaping [9]. We chose to use our definition, since in most applications such as point-scanning microscopy and photolithography, the contrast of a focus in a single light pattern is an important parameter. In theory, the PBR of the focus is proportional to the number of degrees of freedom (pixels or super-pixels) of the SLM [9]. This conclusion is intuitive because we can only increase the intensity at the target location by a limited amount, given that we have only a limited number of degrees of freedom. However, in a noise-free or very low noise situation, if we take the strategy to increase the intensity at the target location while darkening the background near the target location, we can achieve a focus with a higher PBR than that achieved by conventional methods in a given field of view (FOV). We will refer to this method as transmission matrix inversion, because mathematically it takes the pseudoinverse of the transmission matrix to realize it. Popoff *et al.* have demonstrated that using the inverse of the transmission matrix one can recover an image through scattering media with greater fidelity than that using the phase conjugation method [20]. The method we demonstrate here shares the same theoretical foundation with the transmission matrix inversion method they reported in [20]. In this work, we compare the transmission matrix inversion method and the phase conjugation method based on the optical focus (foci) directly measured (without reconstruction) after transmission through the scattering medium and find that the transmission matrix inversion method is able to focus light with higher contrast and fidelity under a noise-free or low noise condition. This high-contrast light focus (foci) formed directly after transmission through scattering

media has a number of important applications, including point-scanning microscopy and photolithography.

2.2 Principle and simulation

Mathematically, we use a transmission matrix T to relate the optical fields before (E_{in}) and after (E_{out}) transmitting through a scattering medium:

$$\mathbf{E_{out}} = \begin{bmatrix} E_{out,1} \\ E_{out,2} \\ \dots \\ E_{out,m} \end{bmatrix} = \begin{bmatrix} t_{11} & t_{12} & \dots & t_{1n} \\ \dots & & & \dots \\ t_{m1} & t_{m2} & \dots & t_{mn} \end{bmatrix} \begin{bmatrix} E_{in,1} \\ E_{in,2} \\ \dots \\ E_{in,n} \end{bmatrix} = \mathbf{T}\mathbf{E_{out}}, m < n. \tag{2.1}$$

Here, the scattering medium is described by a transmission matrix $\mathbf{T}$, whose elements t_{ij} follow a complex Gaussian distribution [21, 22, 23] with a zero mean and a variance σ^2, i.e., $t_{ij} \sim CN(0, \sigma^2)$. The incident field $\mathbf{E_{in}}$ is described by an $n \times 1$ vector and the output field $\mathbf{E_{out}}$ is described by an $m \times 1$ vector. Here, m means that there are m modes in our interested FOV, but does not mean that the total number of output optical modes is m after light propagates through the scattering medium. We assume $m < n$, which is the condition for theoretically realizing a zero background, as will be discussed in the following subsection Focusing light to one target location.

Focusing light to one target location

To focus light through scattering media by conventional methods such as phase conjugation, we obtain the appropriate incident light field by $\mathbf{E_{in}^{conj}} = \mathbf{T}^* \times \mathbf{E_{out}}$ [15]. Here, $\mathbf{T}^*$ denotes the conjugate transpose of $\mathbf{T}$. If we want to focus light to one target location, without losing generality, we can set the desired output field $\mathbf{E_{out}} = \begin{bmatrix} 1 & 0 & \dots & 0 \end{bmatrix}^t$, where $[\cdot]^t$ denotes matrix transpose. Thus, $\mathbf{E_{in}^{conj}}$ is the first column of $\mathbf{T}^*$, i.e., $\mathbf{E_{in}^{conj}} = \mathbf{T}^* \times \begin{bmatrix} 1 & 0 & \dots & 0 \end{bmatrix}^t$, and the output field achieved by the phase conjugation method can be calculated by

$$\mathbf{E_{out}^{conj}} = \mathbf{T} \times \mathbf{T}^* \times \begin{bmatrix} 1 \\ 0 \\ \dots \\ 0 \end{bmatrix}. \tag{2.2}$$

Because of the statistical property of the elements of $\mathbf{T}$, $\mathbf{T} \times \mathbf{T}^* \approx \alpha \mathbf{I}$, where $\mathbf{I}$

$$\mathbf{I_{out}^{conj}} = |\mathbf{E_{out}^{conj}}|^2 = \begin{bmatrix} |E_{out,1}|^2 \\ |E_{out,2}|^2 \\ \cdots \\ |E_{out,m}|^2 \end{bmatrix} = \begin{bmatrix} I_{out,1}^{conj} \\ I_{out,2}^{conj} \\ \cdots \\ I_{out,m}^{conj} \end{bmatrix} \approx \alpha \begin{bmatrix} 1 \\ n^{-1} \\ \cdots \\ n^{-1} \end{bmatrix}. \tag{2.3}$$

Since the elements t_{ij} of $\mathbf{T}$ follow the complex Gaussian distribution, the probability theory shows that the expected value of $I_{out,1}^{conj}$ (peak intensity) is n times higher than that of $I_{out,k}^{conj}$ ($k \neq 1$, background intensity) [9]. Therefore, the PBR is limited by the number of independent incident optical modes n, which depends on the pixel number of the SLM. In this case, we use all the degrees of freedom to enhance only one specific output mode while doing nothing about the background (the rest of the modes). Moreover, the theory only predicts the intensity enhancement statistically based on the distribution of the elements of $\mathbf{T}$; the exact enhancement should be measured experimentally, or calculated based on the known transmission matrix $\mathbf{T}$. However, if we take the matrix inversion, the enhancement is no longer limited by the pixel number on the SLM. Here, we choose the first column of the pseudoinverse of $\mathbf{T}$ as the input field $\mathbf{E_{in}^{inv}}$, i.e., $\mathbf{E_{in}^{inv}} = \mathbf{T^+} \times \begin{bmatrix} 1 & 0 & \ldots & 0 \end{bmatrix}^t$, where $\mathbf{T^+} = \mathbf{T^*}(\mathbf{TT^*})^{-1}$ denotes the Moore–Penrose pseudoinverse [24] of $\mathbf{T}$ and it has the property of $\mathbf{T} \times \mathbf{T^+} = \mathbf{I}$. Then, the output light field can be calculated by

$$\mathbf{E_{out}^{inv}} = \mathbf{T} \times \mathbf{E_{in}^{inv}} = \mathbf{T} \times \mathbf{T^+} \times \begin{bmatrix} 1 \\ 0 \\ \cdots \\ 0 \end{bmatrix} = \begin{bmatrix} 1 \\ 0 \\ \cdots \\ 0 \end{bmatrix}. \tag{2.4}$$

Here, the Moore-Penrose pseudoinverse requires the condition of $m < n$ as mentioned in Eq. 2.1. The result in Eq. 2.4 shows that theoretically the background can be suppressed down to zero; thus the PBR can be increased to infinity. We should note that the phase conjugation is a special case of the Moore-Penrose pseudoinverse. When there is only one output mode (i.e., the transmission matrix is 1 by n), $\mathbf{T^*}$ is the same as $\mathbf{T^+}$ except by a normalization factor. When there are more than one output modes, the transmission matrix inversion method not only increases the intensity of the focus, but also allocates some degrees of freedom to suppress the background intensity.

Figure 2.1 illustrates the difference between the foci achieved by the transmission matrix inversion method and the phase conjugation method for light focusing. In a

given FOV (denoted by the red boxes in Fig. 2.1 (a)), the transmission matrix inversion method has a higher PBR than that of the phase conjugation method, because the background can theoretically be suppressed to zero. For locations outside the FOV, the background intensity for both methods are similiar. Energy conservation is still satisfied because we only re-distribute the energy so as to improve the contrast inside the FOV, but not break the unitarity of the total transmission matrix.

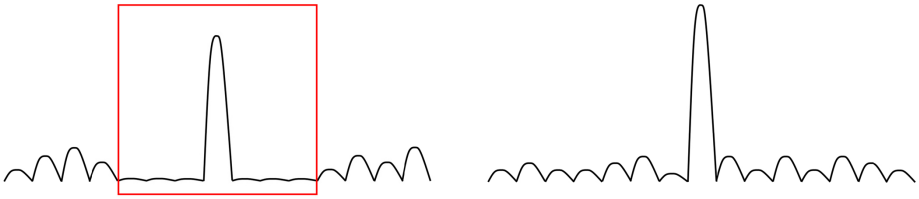

(a) (b)

Figure 2.1: Illustration of focusing light to a target location by (a) the transmission matrix inversion method, and (b) the phase conjugation method. The red box in (a) denotes the selected field of view.

Simulation results are shown in Fig. 2.2. We generated a transmission matrix with a dimension of 49×100, and used both the phase conjugation and the transmission matrix inversion methods to focus light to a single mode inside a FOV of 49 optical modes. The PBR of the focus achieved by the phase conjugation method (Fig. 2.2(a)) is 51. In comparision, the PRB of the focus achieved by the transmission matrix inversion method reaches infinity, since the background within the FOV is suppressed to zero (Fig. 2.2(b)). From Fig. 2.2, it can be seen that the tradeoff of our matrix inversion method is that the peak intensity is lower than that of the phase conjugation method, because some degrees of freedom are assigned to suppress the background.

In practice, the noise in the measurement of transmission matrix reduces the PBR, so the PBR cannot reach infinity. Based on the derivations in the Appendix, we theoretically prove that the PBR of the transmission matrix inversion method is determined by the ratio of the difference between the number of degrees of freedom to control light (n) and the number of modes in the FOV (m) to the normalized noise level (quantified by variance σ_n^2, normalized by σ^2) in transmission matrix measurement:

$$PBR = \frac{n-m}{\sigma_n^2}. \tag{2.5}$$

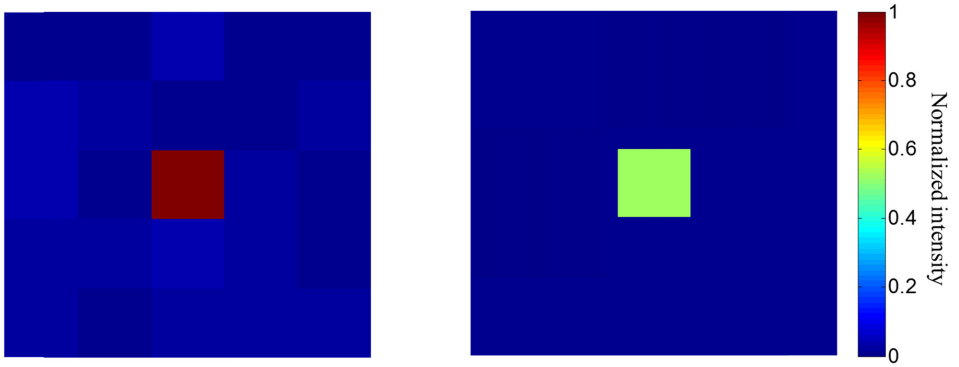

Figure 2.2: Two-dimentional simulations of focusing light through a scattering medium to a target location by (a) phase conjugation, and (b) transmission matrix inversion.

If we fix n and rewrite Eq. 2.5, then $PBR = \frac{1-\beta}{\sigma_n^2} n$, where $\beta = \frac{m}{n}$. If $\frac{1-\beta}{\sigma_n^2} > 1$, PBR can be higher than n, which is the theoretical limit of the PBR in phase conjugation. Elaborations on Eq. 2.5 will be discussed in section 2.4.

Focusing light to multiple target locations

Here, we demonstrate that our matrix inversion method enables light focusing to multiple foci with higher fidelity than those of conventional methods based on phase conjugation [15]. We use an example of focusing light to two target locations to explain the principle (Fig. 2.3). Since the phase conjugation method simply adds the fields of two focus light fields together (Fig. 2.3(a)), the peak of one focus interferes with the background associated with the other focus. Therefore, the peak intensity of the two foci is no longer equal due to the interference, even if they are equal when achieved individually by phase conjugation.

When the PBR of the focus is low, the amplitude of the peak is close to the amplitude of the background, so this low fidelity problem becomes even more severe for the phase conjugation method. In contrast, if we suppress the background associated with one focus at the position of the peak of the other focus, the peak intensities of the two foci would be equal (Fig. 2.3(b)). The matrix inversion method enables us to achieve this scheme. We first select the positions of the foci with equal focal light intensity, then at each focus position, the background associated with the other focus is automatically set to zero.

Figure 2.4 shows the simulation results of focusing light to two locations through

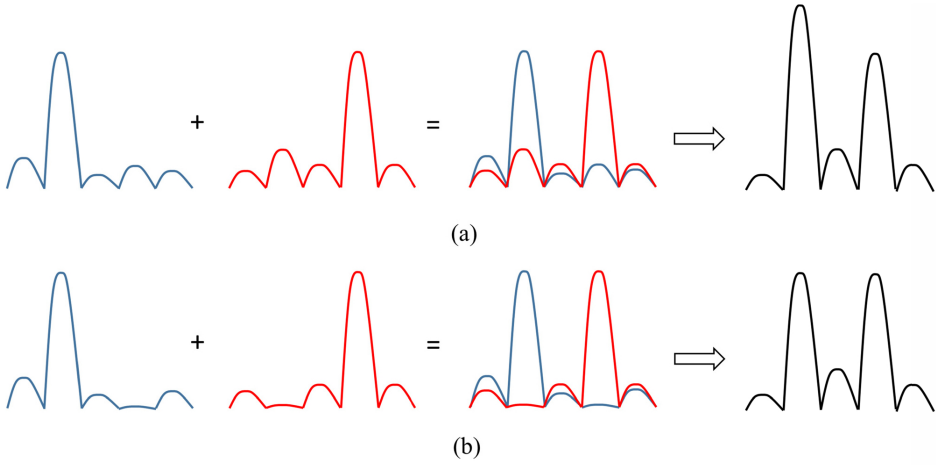

Figure 2.3: Illustration of focusing light to two target locations by (a) phase conjugation, and (b) transmission matrix inversion.

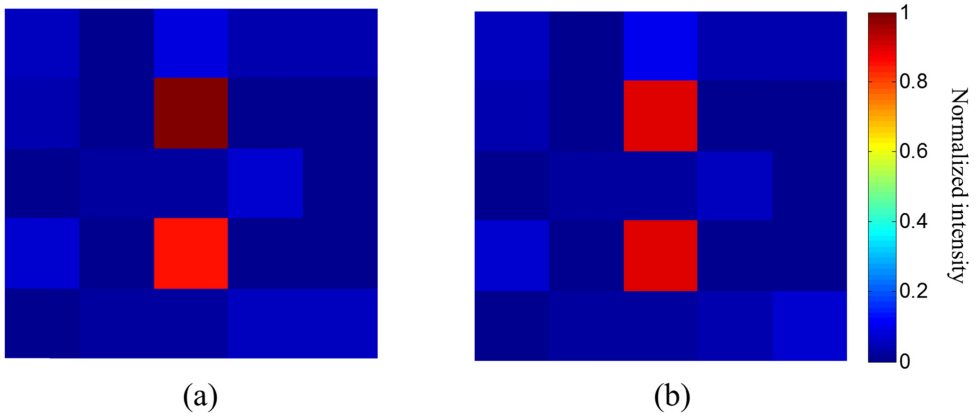

Figure 2.4: Two-dimensional simulations of focusing light to two positions by (a) phase conjugation, and (b) transmission matrix inversion.

a scattering medium. The simulation parameters are the same as those used for focusing light to a single location. The intensities of the two foci achieved by phase conjugation are not equal (1 versus 0.86, see Fig. 2.4(a)), while the intensities of the two foci achieved by matrix inversion are equal (both are 0.9, see Fig. 2.4(b)). This result shows that the matrix inversion method achieves higher fidelity when focusing light to multiple locations. It should be noted that unlike controlling tens of optical modes in the single focus case shown in Fig. 2.2, here, we control only two optical modes at the two target foci locations. Therefore, the intensity of the foci achieved by matrix inversion is not sacrificed as much as that in the single focus

case (Fig. 2.2).

2.3 Experiment

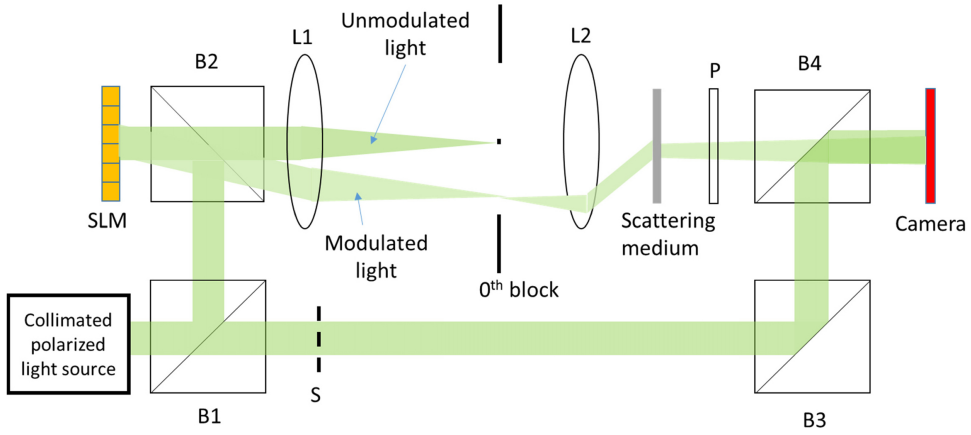

Figure 2.5: Schematic of the experimental setup. B, beam splitter; L, lens; P, polarizer; S, shutter; SLM, spatial light modulator.

We experimentally demonstrate the aforementioned advantages of matrix inversion over phase conjugation to focus light through scattering media. We first measured the transmission matrix of the scattering medium by on-axis four-step phase shifting holography [25]. A diode pumped laser (532 nm, 150 mW, CrystaLaser Inc., USA) was used as a light source. The polarization direction of the emitted light was rotated by a polarizer to make it align with the SLM operation direction. A beam splitter B1 split the light into two paths. The beam that passed through B1 was used as reference beam for holography, and the beam reflected by B1 illuminated a phase-only-modulation SLM (PLUTO, HOLOEYE), which was relayed by lenses L1 and L2 onto a scattering medium made of ground glass (DG10-120, Thorlabs). A polarizer P blocked the light whose polarization was changed by the scattering medium. The scattered light then interfered with the reference beam on the camera sensor (GX1920, Allied Vision). By stepping the phases displayed on the SLM, we retrieved the scattered light field on the camera sensor. Since a portion of the light illuminating the SLM was not modulated, we used a 0th order block (a black disk with a diameter of 100 μm printed on a transparency) to eliminate this part of the light. A phase gradient pattern was added on the SLM to prevent the modulated light from being blocked by the 0th order block. We chose 128 Hadamard bases as the incident fields, and for each Hadamard pattern we recorded the output field on the camera, which represented one column of the transmission matrix. After recording

the transmission matrix, we blocked the reference beam by shutter S and used the transmission matrix inversion method to realize the desired focusing patterns.

Focusing light to one target location with a higher PBR than phase conjugation
A workflow of focusing light to a target location with matrix inversion is shown in Fig. 2.6(a). To effectively suppress the background, we first used the conventional method – phase conjugation - to realize one focus spot with a PBR of 21 (Fig. 2.6(b),(d)). Then, we selected some bright background channels and performed matrix pseudoinversion. By doing this, we selectively darkened the bright background speckle grains to improve the PBR to 35 (Fig. 2.6(c),(e)), achieving a 66% improvement of PBR. The transmission matrix inversion method did not reduce the peak intensity much, but it suppressed the background around the focus. In our experiment, since we used a phase-modulation SLM, we simply took the phase of the calculated incident optical field while keeping the amplitude spatially uniform. We will discuss more about the impact of phase-only modulation in section 2.4.

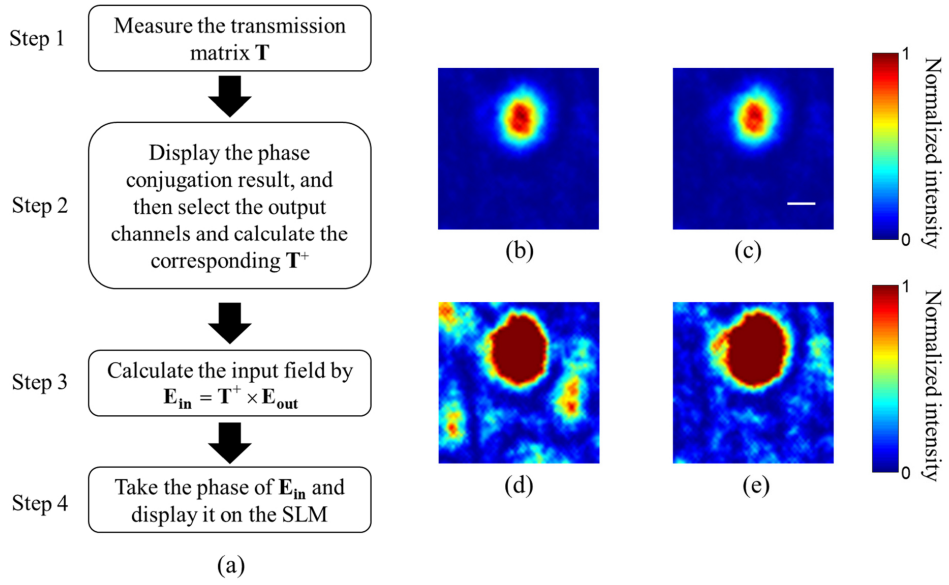

Figure 2.6: Workflow and focus results of matrix inversion. (a) Workflow of realizing a high PBR focusing by matrix inversion. Optical focus achieved by (b) phase conjugation and (c) matrix inversion. Over-exposed images of the focus achieved by (d) phase conjugation and (e) matrix inversion to see the background speckle grains. Scale bar, 50 μm. β=0.1 in our experiment.

Focusing light to multiple target locations with higher fidelity than phase conjugation

We demonstrate that matrix inversion enables a higher fidelity over phase conjugation when focusing light to multiple target locations in Fig. 2.7. Since the phase conjugation method simply adds different focus fields together (Section 2.2), the intensity of two foci is not equal, as shown in Fig. 2.7(a) – (c). As the theory only considers the expected value of the output pattern, phase conjugation can only statistically guarantee that the intensity of the multiple foci are equal, so the focus intensity may not be equal when we only perform the experiment once. In contrast, the intensity of the multiple foci achieved by matrix inversion is more even (Fig. 2.7(d) – (f)), because here the solution is exactly for realizing two focus spots with equal intensity. Therefore the deviation between the expected value and the one-time-realization in the phase conjugation method does not exist here. The patterns in Fig. 2.7 are captured based on three different transmission matrices since we move the scattering medium and the camera to show generality. The line profile comparisons between the foci achieved by the phase conjugation and the matrix inversion methods are shown in Fig. 2.7(g) – (i).

2.4 Discussion

Accurately measuring the transmission matrix is very important for transmission matrix inversion based optical focusing. Because of the measurement noises caused by air turbulence, photon shot noise, mechanical drift of the optical system, etc., the measured transmission matrix always deviates from the true transmission matrix. This deviation limits the PBR improvement of the transmission matrix inversion method. As shown in Eq. 2.5, if we fix n, we have $PBR = \frac{n-m}{\sigma_n^2} = \frac{1-\beta}{\sigma_n^2}n$, where $\beta = \frac{m}{n}$. Simulation results match well with the theoretical results based on Eq. 2.5 (see Fig. 2.8). It is understandable that the PBR drops as β increases (Fig. 2.8 (a)), since in this case we use limited degrees of freedom to control more output optical modes. Obviously, larger measurement errors in transmission matrix measurement lead to lower PBRs, as shown in Fig. 2.8(b). For a given field of view (given β), when the noise level is lower than $1 - \beta$, the PBR can be higher than n. In this case, the PBR achieved by matrix inversion is higher than that achieved by phase conjugation.

In our experiments described in section 2.3, we applied phase-only modulation to realize the transmission matrix inversion method. Phase-only modulation can be treated as noisy amplitude-and-phase modulation since the amplitude of the mod-

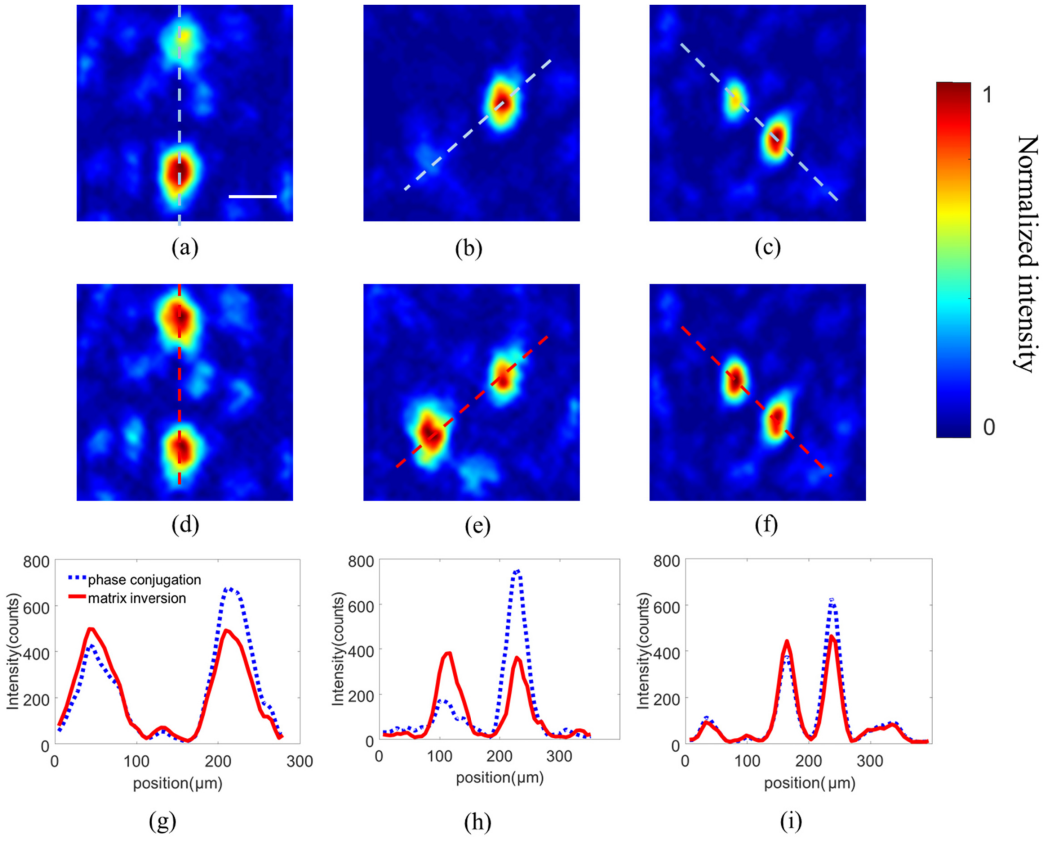

Figure 2.7: Focusing light to two target locations achieved by phase conjugation ((a) – (c)) and by achieved by matrix inversion ((d) – (f)). (g) – (i) Line profiles of the foci shown in (a) – (f) achieved by phase conjugation and matrix inversion. Scale bar, 50 μm.

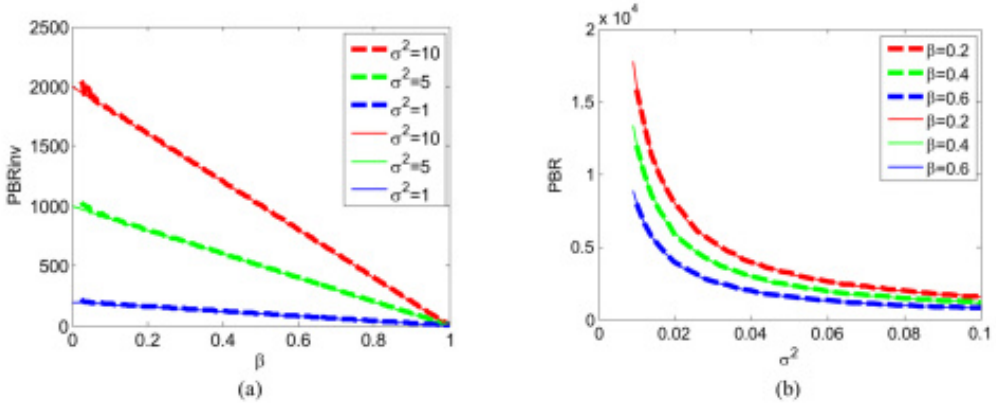

Figure 2.8: PBR versus (a) β and (b) σ^2 as n is fixed as 200. Solid lines: theoretical calculation. Dashed lines: numerical simulations.

ulated light deviates from the field calculated from the matrix inversion. However, phase-only modulation based matrix inversion method still outperforms phase-only modulation based phase conjugation when β is less than ~ 0.4 given the noise level in our experiment. Our experimental results match well with the numerical simulation results (see Fig. 2.9), where we set the normalized measurement noise as 1. Under this condition, we found that the difference between the PBRs of phase-only modulation and amplitude & phase modulation is about 60%.

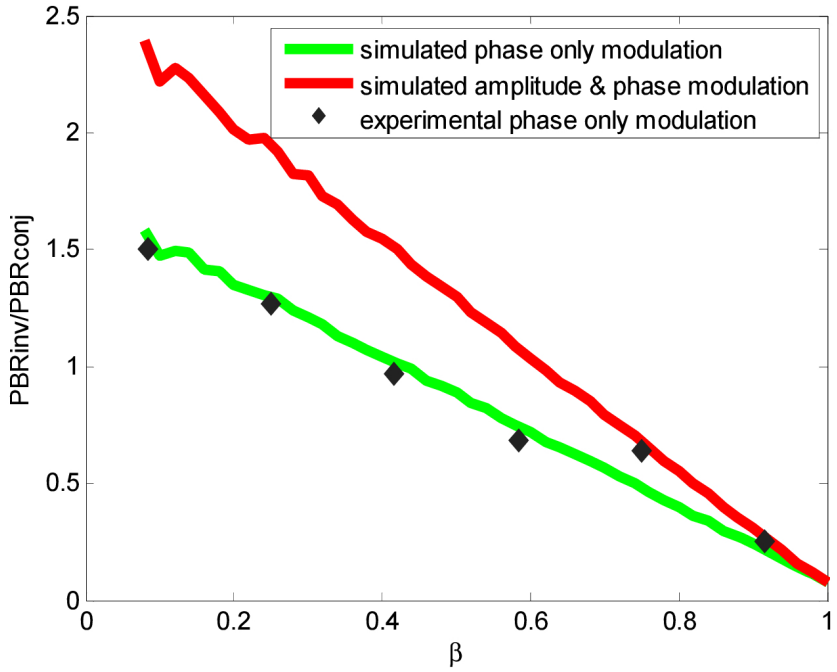

Figure 2.9: Experimental and simulated ratios between the PBRs achieved by matrix inversion and phase conjugation, considering noise and phase-only modulation (black dots and green curve, respectively). Red curve shows the simulation result considering amplitude & phase modulation. In the simulation, $n = 128$ and $\sigma_n = 1$.

In addition to focusing, in a broader view, the transmission matrix inversion method can project a light pattern through scattering media. For example, the matrix inversion method can be used to darken a speckle field in a FOV without creating any focal spots like that demonstrated in section 2.3, while phase conjugation cannot achieve this. In section 2.3, if the target focus position is outside the FOV, what we see inside the FOV is that those bright speckle grains are darkened. Based on this principle, we can find the wavefront solution to darken speckles in a FOV using the following protocol. After measuring the transmission matrix corresponding to the FOV, we only need to add an arbitrary row $\mathbf{r}$ into the measured transmission

matrix $\mathbf{T}$ to make a new transmission matrix $\mathbf{T_{new}} = \begin{bmatrix} \mathbf{r} \\ \mathbf{T} \end{bmatrix}$ and calculate its pseudoinverse $\mathbf{T^{+}_{new}} = \begin{bmatrix} \mathbf{c_1} & \mathbf{c_2} & \dots & \mathbf{c_{m+1}} \end{bmatrix}$, where $\mathbf{c_i}$ is the $i_t h$ column of $\mathbf{T^{+}_{new}}$. Since $\mathbf{T_{new}} \times \mathbf{T^{+}_{new}} = \mathbf{I}$, we get $\mathbf{T_{new}} \times \mathbf{c_1} = \begin{bmatrix} 1 & 0 & \dots & 0 \end{bmatrix}^t$, which means that the first column $\mathbf{c_1}$ of $\mathbf{T^{+}_{new}}$ is orthogonal to all the rows of $\mathbf{T}$. Therefore, $\mathbf{c_1}$ is the wavefront solution to darken the speckle grains in the FOV. The experimental results are shown in Fig. 2.10, where we darkened the speckle grains in red circles in Fig. 2.10(d) – (f) while keeping the speckle grains outside the FOV highly correlated with the original fields (Fig. 2.10(a) – (c)). To show the generality of the method, we moved the camera and the diffuser at three different positions. Unlike the case with the matrix inversion method, the speckle grains in the red circles cannot be fully darkened by using the phase conjugation method, because if we replace the $\mathbf{T^{+}_{new}}$ above by $\mathbf{T^{*}_{new}} = \begin{bmatrix} \mathbf{r}^* & \mathbf{T}_* \end{bmatrix}$, there is no guarantee that the first column $\mathbf{r}^*$ of $\mathbf{T^{*}_{new}}$ is orthogonal to all the rows of $\mathbf{T}$.

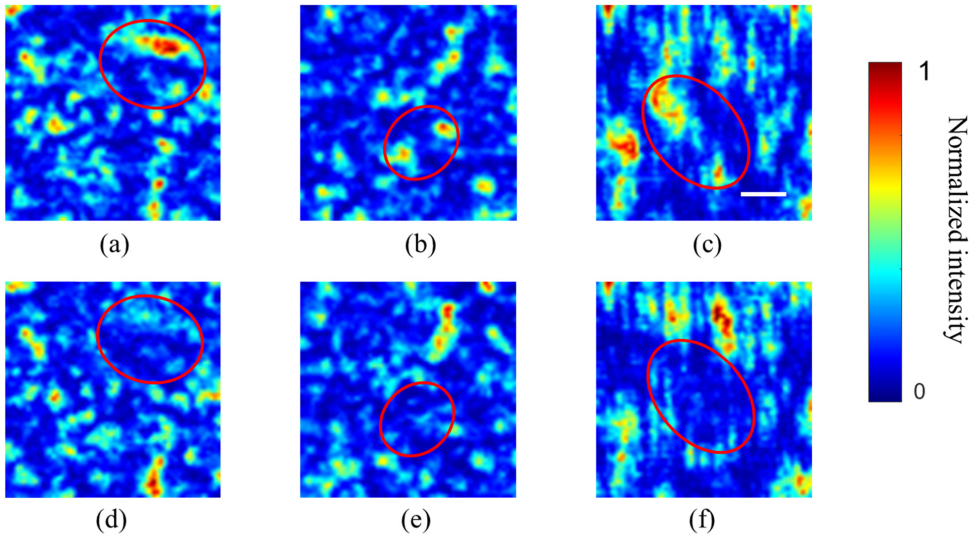

Figure 2.10: Results of speckle darkening. The original speckle patterns before darkening are shown in (a) – (c). After using the matrix inversion method, we can selectively darken the speckle grains enclosed in the red circles ((d) – (f)). Scale bar, 50 μm.

2.5 Summary

In summary, we develop a transmission matrix inversion method for focusing light and projecting patterns through scattering media. We first theoretically and numeri-

cally prove the feasibility of this method, and then experimentally demonstrate that it can perform better than conventional methods under low noise conditions. By using this method, we obtain a higher PBR than that achieved by conventional methods in a given field of view. Moreover, our method improves the fidelity of focusing light to multiple locations through scattering media. This method can also be used for speckle darkening. We derive the analytical expression of the PBR achieved by our method, and predict that the performance can be improved if there are methods to measure the transmission matrix more accurately or devices with known transmission matrices. Since high-contrast (high-PBR) and high-fidelity focusing is critical to many applications such as photolithography and confocal/two-photon microscopy, we believe our method will have an impact in these areas.

2.6 Appendix – Derivation of PBR

In the Appendix, all the letters in bold mean matrices, and the corresponding lowercase italic letters mean the elements in the matrices. Without losing generality, let us assume the desired output field as $\begin{bmatrix}1 & 0 & \dots & 0\end{bmatrix}^t$, then

$$\mathbf{E_{out}^{inv}} = \mathbf{T_0} \times \mathbf{E_{in}^{inv}} = \mathbf{T_0} \times (\mathbf{T_0} + \mathbf{e})^+ \times \begin{bmatrix}1\\0\\\dots\\0\end{bmatrix}, \tag{2.6}$$

where $\mathbf{e}$ is the noise in transmission matrix measurement. Thus $\mathbf{T_0} \times (\mathbf{T_0} + \mathbf{e})^+$ is no longer equal to $\mathbf{I}$. Here, $t_{ij} \sim CN(0,1)$, and we assume $e_{ij} \sim CN(0, \sigma_n^2)$. $\mathbf{T_0} \times (\mathbf{T_0} + \mathbf{e})^+$ can be rewritten as

$$\mathbf{T_0} \times (\mathbf{T_0} + \mathbf{e})^+ = \mathbf{I} - \mathbf{e}(\mathbf{T_0} + \mathbf{e})^+. \tag{2.7}$$

While the first term, $\mathbf{I}$, in Eq. 2.7 multiplied by the desired output vector results in the peak intensity of the output, the second term leads to the background of the output field.

We then conduct singular value decomposition (SVD) [26] for $\mathbf{T_0} + \mathbf{e}$, that is $\mathbf{T_0} + \mathbf{e} = \mathbf{UVD}^*$. By substituting it into Eq. 2.7, we have

$$\mathbf{I} - \mathbf{e}(\mathbf{T_0} + \mathbf{e})^+ = \mathbf{I} - \mathbf{e}(\mathbf{UDV}^*)^+ = \mathbf{I} - \mathbf{eVD^{-1}U}^* = \mathbf{I} - \tilde{\mathbf{e}}\mathbf{D^{-1}U}^*. \tag{2.8}$$

Since V is a unitary matrix, $\tilde{e} = eV$ is still a complex random Gaussian matrix with the same distribution as e [27]. The background of $\mathbf{E_{out}^{inv}}$ is equal to the mean value

of the square of the norm ($\bar{l}_2$) of the element b_{ij} in $b_{ij} = \tilde{e}D^{-1}U^*$. Because unitary matrix $\mathbf{U}^*$ does not change the ($\bar{l}_2$) of $b_{ij}^{'}$, we only need to calculate the ($\bar{l}_2$) of $b_{ij}^{'}$ in $\mathbf{b}^{'} = \tilde{\mathbf{e}}\mathbf{D}^{-1} = \tilde{\mathbf{e}}\mathbf{\Gamma}$. Thus the ($\bar{l}_2$) of $b_{ij}^{'}$ is

$$< |b_{ij}^{'}|^2 >= \frac{1}{m^2}| \sum_{j=1}^{m} \sum_{i=1}^{m} \tilde{e_{ij}} \gamma_{ii}|^2 =< |\tilde{e_{ij}}|^2 \gamma_{ii}^2 > . \tag{2.9}$$

Here, $< |b_{ij}^{'}|^2 >$ means the ensemble average of $|b_{ij}^{'}|^2$. If we assume that $\mathbf{e}$ and ($\mathbf{T0} + \mathbf{e}$) are independent (this approximation holds if $\sigma_n << 1$. Numerical results show that this approximation still works well when $\sigma_n \sim 1$), then $\tilde{\mathbf{e}}$ and $\tilde{\mathbf{\Gamma}}$ are also independent. In this case, Eq. 2.9 becomes

$$< |b_{ij}^{'}|^2 >=< |\tilde{e_{ij}}|^2 \gamma_{ii}^2 >=< |\tilde{e_{ij}}|^2 >< \gamma_{ii}^2 >= 2\sigma_n^2 < \gamma_{ii}^2 > . \tag{2.10}$$

Random matrix theories show that the probability density function (PDF) of singular value d of a m by n standard complex Gaussian matrix is [27]

$$p_d(x) = \frac{\sqrt{-(\frac{x^2}{2n} - (1+\sqrt{\beta})^2)(\frac{x^2}{2n} - (1-\sqrt{\beta})^2)}}{\pi\beta x}, \beta = \frac{m}{n} < 1. \tag{2.11}$$

Since $\gamma_{ii}^2 = d_{ii}^{-2}$, we have the PDF of γ_{ii}^2

$$p_{\gamma^2}(y) = \frac{\sqrt{-(\frac{1}{2ny} - (1+\sqrt{\beta})^2)(\frac{1}{2ny} - (1-\sqrt{\beta})^2)}}{2\pi\beta y}, \beta = \frac{m}{n} < 1. \tag{2.12}$$

Therefore, we have $< \gamma_{ii}^2 >= \int_{\frac{2n}{(1+\sqrt{\beta})^2}}^{\frac{2n}{(1-\sqrt{\beta})^2}} y p_{\gamma^2}(y) dy = \frac{1}{2n(1-\beta)}$. Substituting it into Eq. 2.10, we get

$$< |b_{ij}^{'}|^2 >= \frac{\sigma_n^2}{2n(1-\beta)}. \tag{2.13}$$

Ensemble average of peak intensity is $< |p_i|^2 >=< |1 - b_{ii}|^2 >= 1 + < |b_{ii}|^2 >= 1 + \frac{\sigma_n^2}{2n(1-\beta)}$. Finally, we have

$$PBR = \frac{< |p_i|^2 >}{< |b_{ij}^{'}|^2 >} = \frac{n-m}{\sigma_n^2} + 1 \approx \frac{n-m}{\sigma_n^2}. \tag{2.14}$$

References

[1] Na Ji, Daniel E. Milkie, and Eric Betzig. Adaptive optics via pupil segmentation for high-resolution imaging in biological tissues. *Nature Methods*, 7(2):141–147, December 2009.

[2] Xiao Xu, Honglin Liu, and Lihong V. Wang. Time-reversed ultrasonically encoded optical focusing into scattering media. *Nature Photonics*, 5(3):154–157, January 2011.

[3] Ying Min Wang, Benjamin Judkewitz, Charles A. DiMarzio, and Changhuei Yang. Deep-tissue focal fluorescence imaging with digitally time-reversed ultrasound-encoded light. *Nature Communications*, 3(1), January 2012.

[4] Ke Si, Reto Fiolka, and Meng Cui. Fluorescence imaging beyond the ballistic regime by ultrasound-pulse-guided digital phase conjugation. *Nature Photonics*, 6(10):657–661, August 2012.

[5] Edward Haojiang Zhou, Haowen Ruan, Changhuei Yang, and Benjamin Judkewitz. Focusing on moving targets through scattering samples. *Optica*, 1(4):227, October 2014.

[6] Haowen Ruan, Joshua Brake, J. Elliott Robinson, Mooseok Jang, Cheng Xiao, Chunyi Zhou, Viviana Gradinaru, and Changhuei Yang. Optogenetic control of neural activity with time-reversed ultrasound encoded light. In *Optics in the Life Sciences Congress*. OSA, 2017.

[7] Jonghee Yoon, Minji Lee, KyeoReh Lee, Nury Kim, Jin Man Kim, Jongchan Park, Hyeonseung Yu, Chulhee Choi, Won Do Heo, and YongKeun Park. Optogenetic control of cell signaling pathway through scattering skull using wavefront shaping. *Scientific Reports*, 5(1), August 2015.

[8] Zheng Huang. A review of progress in clinical photodynamic therapy. *Technology in Cancer Research & Treatment*, 4(3):283–293, June 2005.

[9] I. M. Vellekoop and A. P. Mosk. Focusing coherent light through opaque strongly scattering media. *Optics Letters*, 32(16):2309, August 2007.

[10] I. M. Vellekoop and A. P. Mosk. Universal optimal transmission of light through disordered materials. *Physical Review Letters*, 101(12), September 2008.

[11] Zahid Yaqoob, Demetri Psaltis, Michael S. Feld, and Changhuei Yang. Optical phase conjugation for turbidity suppression in biological samples. *Nature Photonics*, 2(2):110–115, January 2008.

[12] Meng Cui and Changhuei Yang. Implementation of a digital optical phase conjugation system and its application to study the robustness of turbidity suppression by phase conjugation. *Optics Express*, 18(4):3444, February 2010.

[13] Chia-Lung Hsieh, Ye Pu, Rachel Grange, Grégoire Laporte, and Demetri Psaltis. Imaging through turbid layers by scanning the phase conjugated second harmonic radiation from a nanoparticle. *Optics Express*, 18(20):20723, September 2010.

[14] Yuecheng Shen, Yan Liu, Cheng Ma, and Lihong V. Wang. Focusing light through biological tissue and tissue-mimicking phantoms up to 9.6 cm in thickness with digital optical phase conjugation. *Journal of Biomedical Optics*, 21(8):085001, August 2016.

[15] S. M. Popoff, G. Lerosey, R. Carminati, M. Fink, A. C. Boccara, and S. Gigan. Measuring the transmission matrix in optics: an approach to the study and control of light propagation in disordered media. *Physical Review Letters*, 104(10), March 2010.

[16] Angélique Drémeau, Antoine Liutkus, David Martina, Ori Katz, Christophe Schülke, Florent Krzakala, Sylvain Gigan, and Laurent Daudet. Reference-less measurement of the transmission matrix of a highly scattering material using a DMD and phase retrieval techniques. *Optics Express*, 23(9):11898, April 2015.

[17] Jonghee Yoon, KyeoReh Lee, Jongchan Park, and YongKeun Park. Measuring optical transmission matrices by wavefront shaping. *Optics Express*, 23(8):10158, April 2015.

[18] Moonseok Kim, Wonjun Choi, Youngwoon Choi, Changhyeong Yoon, and Wonshik Choi. Transmission matrix of a scattering medium and its applications in biophotonics. *Optics Express*, 23(10):12648, May 2015.

[19] Roarke Horstmeyer, Haowen Ruan, and Changhuei Yang. Guidestar-assisted wavefront-shaping methods for focusing light into biological tissue. *Nature Photonics*, 9(9):563–571, August 2015.

[20] Sébastien Popoff, Geoffroy Lerosey, Mathias Fink, Albert Claude Boccara, and Sylvain Gigan. Image transmission through an opaque material. *Nature Communications*, 1(1), September 2010.

[21] Joseph W Goodman. *Statistical optics*, volume 1. New York, Wiley-Interscience, 1985.

[22] N. Garcia and A. Z. Genack. Crossover to strong intensity correlation for microwave radiation in random media. *Physical Review Letters*, 63(16):1678–1681, October 1989.

[23] John Brian Pendry, A. MacKinnon, and P. J. Roberts. Universality classes and fluctuations in disordered systems. *Proceedings of the Royal Society of London. Series A: Mathematical and Physical Sciences*, 437(1899):67–83, April 1992.

[24] Kyle J. Myers Harrison H. Barrett. *Foundations of Image Science*. Wiley-Interscience, 1st edition, 2003.

[25] Tong Zhang and Ichirou Yamaguchi. Three-dimensional microscopy with phase-shifting digital holography. *Optics Letters*, 23(15):1221, August 1998.

[26] Gene H. Golub and Charles F. van Loan. *Matrix Computations*. JHU Press, fourth edition, 2013.

[27] Antonia Maria Tulino and Sergio Verdú. Random matrix theory and wireless communications. *Foundations and Trends in Communications and Information Theory*, 1(1), 2004.

Chapter 3

WIDE ANGULAR RANGE AND HIGH RESOLUTION BEAM STEERING BY METASURFACE-COUPLED PHASED ARRAY

Optical beam steering has broad applications in LIDAR, optical communications, optical interconnects and spatially resolved optical sensors. For high speed applications, phased-array-based beam steering methods are favored over mechanical methods as they are unconstrained by inertia and can inherently operate at a higher speed. However, phased array systems exhibit a tradeoff between angular range and beam divergence, making it difficult to achieve both a large steering angle and a narrow beam divergence. Here, we present a beam steering method based on wavefront shaping through a disorder-engineered metasurface that circumvents this range-resolution tradeoff. We experimentally demonstrate that, through this technique, one can continuously steer an optical beam within a range of 160° (80° from normal incidence) with an angular resolution of about 0.01° at the cost of beam throughput.

3.1 Introduction

Optical beam steering has applications in LIDAR, optical communications and optical interconnects [1, 2, 3]. Broadly speaking, beam steering is performed either mechanically or via a phased array. Mechanical solutions, such as decentered lenses [4], Risley prisms [5], and galvanometer-scanning mirrors [6], use reflective or deflective optics and moving optical elements to steer the light. Phased-array-based solutions typically involve the use of coherent light sources and phase modulators [7, 8, 9, 10, 11]. By modulating the phase of each element in the array, the emitted coherent light can be made to constructively interfere in the far field at a specified angle, thereby generating a beam in the desired direction.

The performance of beam steering systems can be characterized by the steering angular range (θ), angular resolution ($\delta\theta$), number of resolvable beam directions ($N_{dir} = \theta/\delta\theta$), beam throughput, and speed. For all of these benchmarks except speed, mechanical systems are on par or outperform phased arrays [12]. This is especially true for the maximum number of resolvable beam directions. The best reported number of resolvable beam directions (1D) for a mechanical method can reach to $\sim 2.5 \times 10^5$ [12], while the best reported number for a phased array method

is 500 [11] – a difference of 3 orders of magnitude. On the other hand, phased arrays hold the advantage in speed over mechanical methods. Specifically, inertia limits the steering speed of mechanical solutions – a problem that phased array methods do not have to contend with. As such, applications that require high speed beam steering almost invariably use phased arrays.

Since phased arrays significantly underperform in the number of resolvable beam directions, improvements to phased arrays that can improve on this count are very important and relevant for practical applications.

In most phased arrays, the number of resolvable beam directions, N_{dir}, is fundamentally tied to the number of controllable elements in the array, $N_control$. This relationship can be easily understood as follows. The steering range $\theta \propto 1/a$ and the angular resolution $\delta\theta \propto 1/A$, where a is the size of each element of the array and A is the total array size. Here, $\delta\theta$ is defined as the full width at half maximum (FWHM) of the steered beam. Thus, $N_{dir} = \theta/\delta\theta \propto A/a = N_{control}$. Put in another way, this implies a tradeoff between the steering range and angular resolution that can only be improved by increasing the number of control elements.

Existing on-chip phased-array methods can only provide tens to thousands of independent degrees of control [7, 8, 9, 10, 11] and thus have a limited number of resolvable steering directions. To our knowledge, the state-of-the-art phased array described in ref [11] has the highest reported number of resolvable steering directions (about 500 in 1D).

In this work, we report a new phased-array implementation method that circumvents this restriction to provide a large increase in the number of resolvable steering directions without requiring a large scale up in the number of controllable elements. In our scheme, we trade off the beam throughput (fraction of output energy in the desired direction) to accomplish this. In certain applications such as non-energy critical optical interconnects and communications, this tradeoff is acceptable as our method can still provide an excellent signal to background ratio in the beam direction.

3.2 Principle

Our phased-array method relies on a disorder-engineered metasurface as its key optical component. This metasurface is a random phase mask that consists of a 2D array of subwavelength-sized scatterers (SiN_x square nanoposts with a height of 630 nm) on a fused silica substrate arranged in a square lattice with a pitch size of 350

nm, similar to the metasurface used in our previous work [13]. The metasurface has high transmission (>95%) and each nanopost confers a phase shift to the light that passes through it. The phase delay of the transmitted light is controlled by tuning the width of each nanopost, which varies from 60 nm to 275 nm. This range of width covers a relative phase delay of 0 to 2 π. The random phase pattern on the metasurface is designed to scatter light isotropically within a range of 0 to π at the design wavelength (532 nm). In other words, the pre-designed disorder-engineered metasurface is a phase mask with a known random phase pattern that can convert low spatial frequency wave vectors into high spatial frequency wave vectors in a predetermined manner. When combined with a spatial light modulator (SLM), the system can output light over a much larger range of angles than what is possible with a spatial light modulator alone.

Figure 3.1 compares the working principles of a single SLM beam steering system and a metasurface-coupled SLM beam steering system. A simple SLM beam steering system uses a SLM to directly perform beam steering [14]. However, as SLM pixels tend to be large in comparison to the optical wavelength, the achievable steering angle tends to be small (see Fig. 3.1(a)). The disorder-engineered metasurface is capable of scattering light uniformly within a range of -90° to 90° (Fig. 3.1(b)) due to the subwavelength size and random distribution of the nanoposts. By displaying the correct phase map on the SLM, constructive interference occurs and light intensity is enhanced at the specified angle.

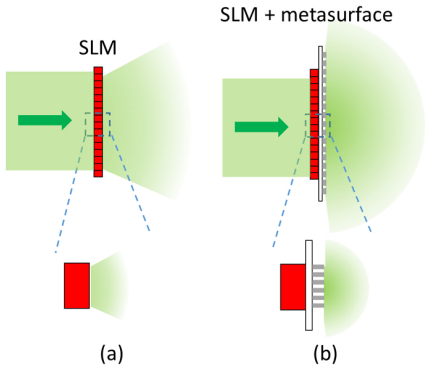

Figure 3.1: Comparison of steering range of a single SLM structure and a metasurface-coupled SLM structure. (a) Without the metasurface, the SLM can only provide a small diffraction envelop that is determined by the pixel size, and thus can only steer light within a limited angular range. (b) With the metasurface-coupled SLM structure, since each scatterer is subwavelength, the steereable range can span from –90° to 90°.

The required phase pattern to actuate beam steering in the desired direction can be calculated by using the principles of optical phase conjugation (OPC) [15], as shown in Fig. 3.2. In OPC, the input-output response of a scattering system can be characterized by a transmission matrix $\mathbf{T_{AB}}$ (from plane A to B), with $\mathbf{E_B} = \mathbf{T_{AB}}\mathbf{E_A}$. The random scattering nature implies that the elements of $\mathbf{T_{AB}}$ follow an identical independent complex Gaussian distribution [16]. Due to optical reciprocity, $\mathbf{T_{BA}} = \mathbf{T_{AB}}'$ (where $(\cdot)'$ is the transpose operator). To realize a desired optical field $\mathbf{E_{desired}}$ (Fig. 3.2 (b)), which corresponds to a beam steered at a specified angle, the optical field solution on the SLM, $\mathbf{E_{cal}}$, is calculated by $\mathbf{E_{cal}} = (\mathbf{T_{AB}}\mathbf{E^*_{desired}})^* = \mathbf{T^*_{AB}}\mathbf{E_{desired}}$ ($(\cdot)^*$ is the conjugation operator), which first calculates the scattering speckle field of the beam from the desired direction (Fig. 3.2 (a,i) and then phase conjugates it (Fig. 3.2 (a,iii)). The output field is then $\mathbf{E_{out}} = \mathbf{T_{BA}}\mathbf{T^*_{AB}}\mathbf{E_{desired}} = (\mathbf{T^+_{AB}}\mathbf{T_{AB}})^*\mathbf{E_{desired}} \approx \mathbf{E_{desired}}$). Since T is a complex Gaussian random matrix, $\mathbf{T^+T} \approx \mathbf{I}$ [17]. In our case, $\mathbf{T_{AB}}$ is a diagonal matrix, with each element corresponding to the phase delay of each nanopost. To match the pixel size of the SLM, $\mathbf{E_{cal}}$ is low-pass filtered prior to being displayed on the SLM (Fig. 3.2 (a,ii)).

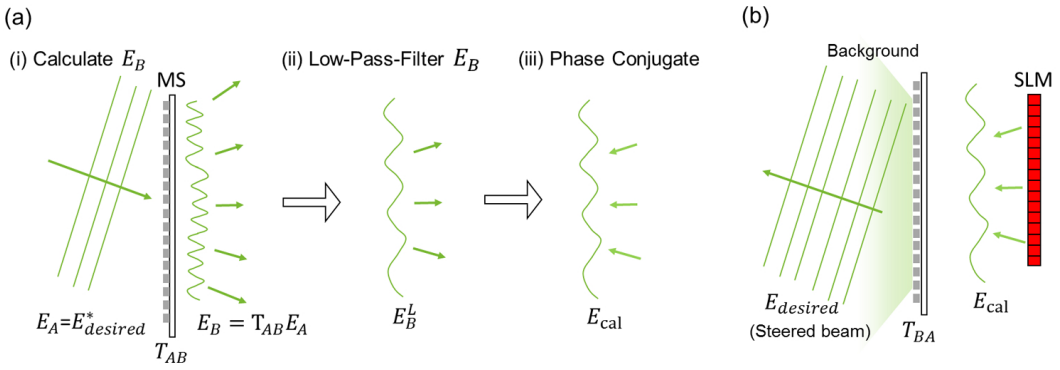

Figure 3.2: The process required to steer the beam is to (a) calculate the required phase pattern on the SLM and (b) display the phase pattern on the SLM and reflecting light off the SLM. The steps to calculate the phase pattern are as follows. (i) Assume there is an incident field E_A with the desired steering angle incident on the metasurface (MS). Calculate the transmitted scattered field E_B. (ii) In order to match the SLM pixel size to the scattered field speckle size, E_B is low-pass filtered to be E^L_B. (iii) E^L_B is phase conjugated to get the phase pattern required on the SLM, E_{cal}. (b) The beam can then be steered by displaying the phase of E_{cal} on the SLM and reflecting light off the SLM and into the metasurface. SLM, spatial light modulator; MS, metasurface.

As a side note, we would like to point out that this procedure is related to our

earlier work on using a disorder-engineered metasurface to render a record number of addressable diffraction-limited spots [13]. In fact, it is possible to use the same pair of SLM and disorder-engineered metasurface to perform both focused-spot rendering and beam steering. This flexibility is a key advantage of metasurface-coupled SLM wavefront shaping.

3.3 Experiment

The optical setup for the disorder-engineered metasurface-coupled phased-array system for beam steering is shown in Fig. 3.3. We first accurately map the SLM onto the metasurface (Fig. 3.3(a)) and then use the aligned system to perform beam steering (Fig. 3.3(b)). The laser beam (532nm, 150mW, CrystaLaser Inc. USA) is first split into two arms by a polarizing beam splitter (PBS). Light on arm R2 is scattered by the metasurface and interferes with light from arm R1 at BS1. The interference pattern is incident on the SLM (PLUTO, HOLOEYE) and camera (GX1920, Allied Vision), which are at conjugate planes with the metasurface. The SLM is demagnified 5x to match it to the size of the metasurface. An electro-optic modulator (EOM) adds a phase shift to the light on arm R2 in order to extract the phase of the light scattered by the metasurface, which is done using phase-shifting holography.

Once the metasurface is aligned, the phase pattern required to steer the beam to a specific angle is determined and displayed on the SLM. Light from arm R2 is blocked and light from arm R1 is modulated by the SLM in order to realize beam steering. (Fig. 3.3(b)). The zeroth-order block removes the component of light from the SLM that remains unmodulated. L4 and camera 2 are moved to image the steered beam. The procedure to digitally align the metasurface to the rest of the system is as follows. First, the phase of the light scattered from the metasurface is calculated. This measured phase map is compared to the designed phase map using cross-correlation to determine the lateral position of the metasurface. Next, the axial position of the metasurface is determined by digitally propagating the measured field and comparing it to the designed phase map. Once the position of the metasurface is precisely determined, the optical aberrations of the system are characterized by segmenting the designed map and the measured field into a 2D array of 27 by 48 and taking their difference. Finally, using the parameters determined in digital alignment, the calculated pattern is displayed on the SLM to steer light.

Figure 3.4(a) shows the steering system scheme and the far field beam shapes at

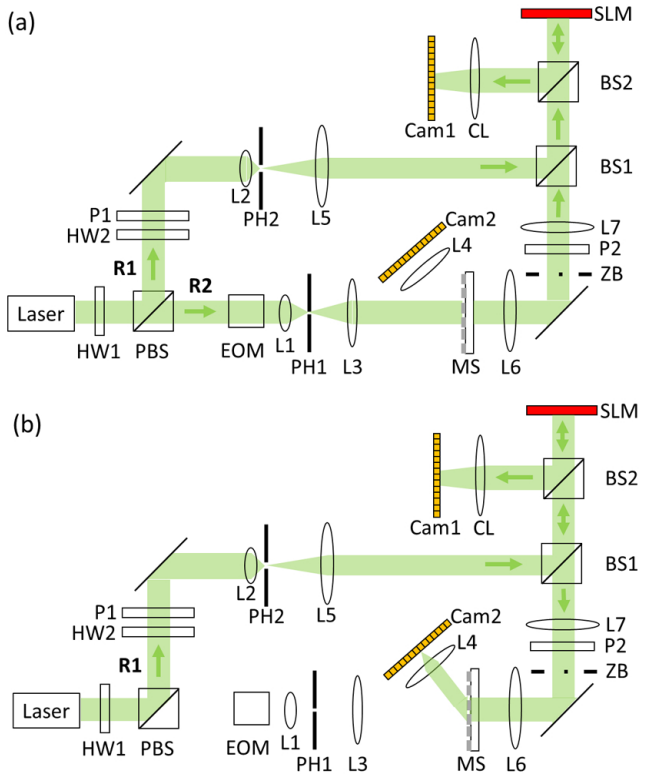

Figure 3.3: Schematic of optical system, showing light path to (a) align the metasurface and (b) realize beam steering (b). BS, beam splitter; Cam, camera; CL, camera lens; EOM, electro-optic modulator; HW, half-wave plate; L, lens; M, mirror; MS, metasurface; P, polarizer; PH, pinhole; PBS, polarized beam splitter; ZB, zeroth-order block.

the steering angles of 0°, 40° and 80°, acquired by moving the imaging system (L4 and Camera 2). The elliptical shape of the beam is due to the rectangular aperture shape on the metasurface. The 1D line profile at 0° is also plotted, showing a high signal to background ratio (14 dB). In Fig. 3.4(b), we show 1D shapes of the far field beams at other steering angles ranging from 0° to 80°. From the figure, we can see that our measured angular resolution matches the theoretical calculation very well. As the steering angle increases, the beam divergence is enlarged due to the projection effect of the emitting aperture. That is, when viewing at an angle, the system aperture size is scaled by a cosine factor. Experimentally, the steerable range was 160° (from normal incidence to 80°, due to measurement limit), and the angular resolution for steering angles near 0° was 0.01° and 0.018° in two axes, respectively. The illumination area on the metasurface is $3.1 \times 1.7 mm^2$, which has the theoretical angular resolution on both axes same as the experimental results. The average beam divergence within the steering range was 0.017° and 0.03° in two

axes. From the results above, the system should be able to steer the beam to 5×10^7 resolvable directions in 2D (about 10^4 in 1D), which is three orders of magnitudes greater than previously reported phased-array performance [11]. In comparison, the SLM has 1080×1920 pixels, yielding 2×10^6 nominal degrees of control and possible resolvable steering direction.

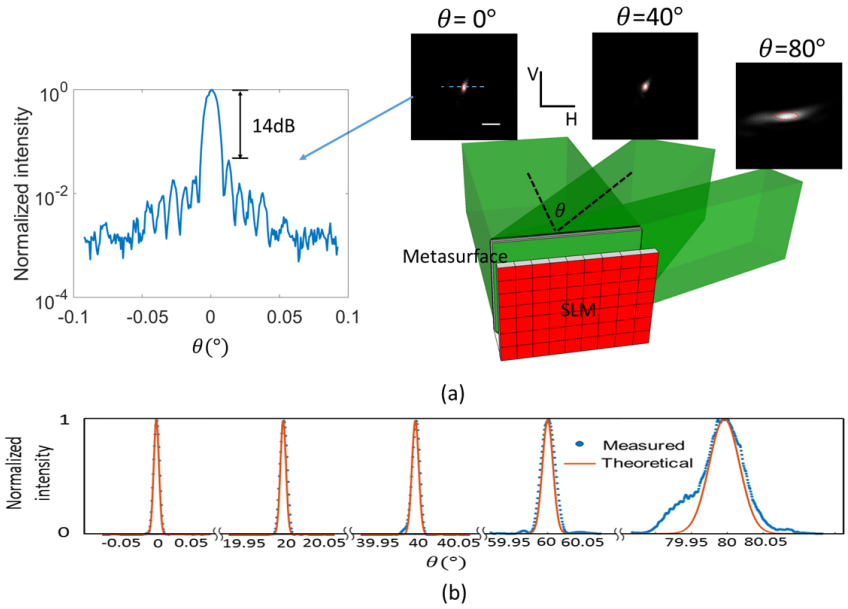

Figure 3.4: Experimental results of beam steering. (a) The illustration of the steering scheme (the 4-f imaging system for imaging the SLM to the metasurface is not shown here). The far field beam shapes at the steering angles of 0°, 40°, and 80° are shown. The red circles enclose the theoretical FWHM of the beams. The intensity line profile at normal direction is shown. (b) The 1D far field beam shapes at other steering angles. The red lines denote the theoretical shapes of the beams. The blue dots denote the measured data. Scale bar: 0.05°. V, vertical axis; H, horizontal axis.

Figure 3.5 shows the beam energy as a function of steering angle. The drop in energy at larger angles is expected due to the cosine dependency of the visible system aperture when viewed at an angle. We can see that the performance of the metasurface-coupled system (in blue) is significantly better than the SLM-only system (in red). In fact, the metasurface-coupled system is capable of steering beams substantially beyond the 5° range limitation of the SLM (red). For comparison, we have also plotted the profile associated with a Lambertian source (in yellow), which represents the theoretical upper bound.

Table 3.1 compares the best steering performance achieved by a selection of phased-array methods reported in the literature. To our knowledge, our method provides the

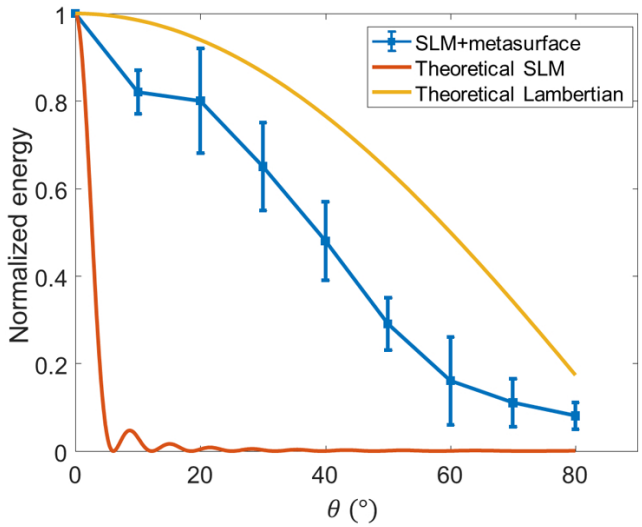

Figure 3.5: The normalized beam energy versus steering angle for our metasurface-coupled SLM system (in blue) in comparison to an SLM-only beam steering system (in red). The performance of a lambertian source (in yellow) is included to show the theoretical upper bound. All of the curves are normalized based on the energy at θ=0°.

Table 3.1: Comparison of the steering performance of different phased-array methods

	Range	Resolution	N_{dir} (1D)	Throughput
Hutchison	80°	0.14°	500	Not mentioned
Haellstig	4°	<0.005°	800[1]	68%
Metasurface-coupled phased array	160°	0.017°	9.4×10^3	1.0×10^{-6}

[1] Calculated from range and resolution.

best reported performance in terms of steering range and the number of resolvable directions amongst phased arrays. This is consistent with our expectation that the metasurface is capable of spreading the light over a large angular range while still 'preserving' the original aperture size of the SLM to provide a sharp angular resolution. However, the throughput of our system, defined as the ratio of the power in the directed beam direction versus the total output power, is very low.

The throughput is expressed as $throughput = K \times \frac{\pi}{4} \frac{N_{control}}{N_{mode}}$, where $N_{control}$ is the degrees of control on the SLM, N_{mode} is the number of optical modes in the system aperture, $\pi/4$ is due to the phase-only modulation of the SLM [18], and K is an

empirical factor that accounts for experimental imperfections. For an ideal system, K should equal 1. Here, the optical mode set is defined as the set of basis vectors that are needed to characterize the output electric field. N_{mode} is calculated as $N_{mode} = 2\pi A/\lambda^2$, where A is the aperture area and λ is the wavelength of light [19]. In our experiment, K is $\sim 3.8\times10^{-3}$ due to the metasurface fabrication imperfection and residual optical system misalignment.

This tradeoff of throughput for increased number of resolvable directions is a direct consequence of the fact that we have used the metasurface to access a much larger beam steering range without increasing the number of SLM control elements. For applications where power inefficiency is not an issue, our method is an effective solution to substantially increasing the number of resolvable steering beam directions. We would like to draw attention to the fact that the peak-to-background contrast of the steered beam can be substantial even though the throughput is low; the measured contrast ratio was 23 (14 dB) in the experiment described by Fig. 3.4(a).

3.4 Discussion

In effect, the conventional SLM phased array and our metasurface-coupled phased array differs in performance emphasis. To see this, consider a given system aperture size A and number of control elements $N_{control}$. For a conventional SLM phased array, as $N_{control}$ increases, the throughput of the SLM remains fixed but the number of resolvable steering directions increases. The situation is reversed for the metasurface-coupled phased array. As $N_{control}$ increases, the number of resolvable steering directions stays fixed while the throughput increases. In the limiting case where $N_{control} = N_{mode}$, both types of phased arrays are expected to have the same theoretical throughput and number of steering directions.

We believe that the concept of equipping an active phased array with a passive disorder-engineered metasurface can be employed by current chip-based phased array methods that suffer from the tradeoff between steerable range and angular resolution. The cost of a passive metasurface with subwavelength scatterers and a large aperture is much lower than that of a highly integrated chip. Moreover, since the transmission property of the metasurface is known, instead of optical phase conjugation, other algorithms, such as transmission matrix inversion [17], can be used for customized applications. For instance, the algorithm in ref [17] allows the beam steering system to provide lower background intensity within a given steering range than the phase conjugation algorithm. Currently, the metasurface is designed

at 532 nm and we can expect the system performance to deteriorate if the operating wavelength is changed. One potential strategy is to design the metasurface so that the nanoposts confer a broader range of phase delays from 0 to $M \times 2\pi$ where M is a large integer. This way, a wavelength shift will have a smaller impact on the overall phase delay distribution profile. This is an area that deserves further study and optimization.

3.5 Summary

In summary, we have demonstrated a disorder-engineered metasurface coupled phased-array-based beam steering system with a large steering range and narrow beam divergence, which provides us with more resolvable directions at the cost of throughput. The enhancement of steering range is attributable to the subwavelength scatterers, and the high angular resolution is attributable to the large aperture of the metasurface. Since the phase map of the metasurface is known a priori, the phase solution on the SLM for any specified steering angle within the steering range can be found computationally after alignment. This idea of disorder-engineered metasurface-coupled phased-array method offers an effective solution to the range-resolution tradeoff in traditional phased-array methods, and can potentially be applied in LIDAR, free space optical communications, and optical interconnects.

References

[1] Brent Schwarz. Mapping the world in 3d. *Nature Photonics*, 4(7):429–430, July 2010.

[2] Feng Feng, I. H. White, and T. D. Wilkinson. Free space communications with beam steering a two-electrode tapered laser diode using liquid-crystal SLM. *Journal of Lightwave Technology*, 31(12):2001–2007, June 2013.

[3] C. J. Henderson, D. G. Leyva, and T. D. Wilkinson. Free space adaptive optical interconnect at 1.25 gb/s, with beam steering using a ferroelectric liquid-crystal SLM. *Journal of Lightwave Technology*, 24(5):1989–1997, May 2006.

[4] Bradley D. Duncan. Wide-angle decentered lens beam steering for infrared countermeasures applications. *Optical Engineering*, 43(10):2312, October 2004.

[5] Philip J. Bos. Wide-angle achromatic prism beam steering for infrared countermeasure applications. *Optical Engineering*, 42(4):1038, April 2003.

[6] M. Jofre, G. Anzolin, F. Steinlechner, N. Oliverio, J. P. Torres, V. Pruneri, and M. W. Mitchell. Fast beam steering with full polarization control using

a galvanometric optical scanner and polarization controller. *Optics Express*, 20(11):12247, May 2012.

[7] Ami Yaacobi, Jie Sun, Michele Moresco, Gerald Leake, Douglas Coolbaugh, and Michael R. Watts. Integrated phased array for wide-angle beam steering. *Optics Letters*, 39(15):4575, July 2014.

[8] Jie Sun, Ehsan Shah Hosseini, Ami Yaacobi, David B. Cole, Gerald Leake, Douglas Coolbaugh, and Michael R. Watts. Two-dimensional apodized silicon photonic phased arrays. *Optics Letters*, 39(2):367, January 2014.

[9] Firooz Aflatouni, Behrooz Abiri, Angad Rekhi, and Ali Hajimiri. Nanophotonic projection system. *Optics Express*, 23(16):21012, August 2015.

[10] Hooman Abediasl and Hossein Hashemi. Monolithic optical phased-array transceiver in a standard SOI CMOS process. *Optics Express*, 23(5):6509, March 2015.

[11] David N. Hutchison, Jie Sun, Jonathan K. Doylend, Ranjeet Kumar, John Heck, Woosung Kim, Christopher T. Phare, Avi Feshali, and Haisheng Rong. High-resolution aliasing-free optical beam steering. *Optica*, 3(8):887, August 2016.

[12] Hans Dieter Tholl. Novel laser beam steering techniques. In David H. Titterton, editor, *Technologies for Optical Countermeasures III*. SPIE, September 2006.

[13] Mooseok Jang, Yu Horie, Atsushi Shibukawa, Joshua Brake, Yan Liu, Seyedeh Mahsa Kamali, Amir Arbabi, Haowen Ruan, Andrei Faraon, and Changhuei Yang. Wavefront shaping with disorder-engineered metasurfaces. *Nature Photonics*, 12(2):84–90, January 2018.

[14] Emil Haellstig, Johan Stigwall, Mikael Lindgren, and Lars Sjoqvist. Laser beam steering and tracking using a liquid crystal spatial light modulator. In William E. Thompson and Paul H. Merritt, editors, *Laser Systems Technology*. SPIE, September 2003.

[15] Zahid Yaqoob, Demetri Psaltis, Michael S. Feld, and Changhuei Yang. Optical phase conjugation for turbidity suppression in biological samples. *Nature Photonics*, 2(2):110–115, January 2008.

[16] Joseph W. Goodman. Speckle phenomena in optics: theory and applications. *Journal of Statistical Physics*, 130(2), September 2007.

[17] Jian Xu, Haowen Ruan, Yan Liu, Haojiang Zhou, and Changhuei Yang. Focusing light through scattering media by transmission matrix inversion. *Optics Express*, 25(22):27234, October 2017.

[18] I. M. Vellekoop and A. P. Mosk. Focusing coherent light through opaque strongly scattering media. *Optics Letters*, 32(16):2309, August 2007.

[19] Allard P. Mosk, Ad Lagendijk, Geoffroy Lerosey, and Mathias Fink. Controlling waves in space and time for imaging and focusing in complex media. *Nature Photonics*, 6(5):283–292, May 2012.

Chapter 4

CONTROLLING LIGHT THROUGH COMPLEX SCATTERING MEDIA WITH OPTICAL-CHANNEL-BASED INTENSITY STREAMING

For the past decade, optical wavefront shaping has been the standard technique to control light through scattering media. Implicit in this dominance is the assumption that knowledge of the optical phase is a necessity for optical control through scattering media. In this work, we challenge this assumption by reporting on an intensity-only approach for light control through a disordered scattering medium – optical-channel-based intensity streaming (OCIS). Instead of actively tuning the interference between the optical paths via wavefront shaping, OCIS can control light and transmit information through scattering media with linear intensity operation. We describe this method with an intensity transmission matrix framework. We experimentally characterize focus patterns created through scattering media and demonstrate that, unlike wavefront shaping, OCIS can generate distinct energy null points. Finally, we demonstrate the use of OCIS to implement a scattering medium mediated secure optical communications application.

4.1 Introduction

Seeing through fog, looking around corners, and peering deep into biological tissue have traditionally been considered to be impossible tasks in optics. The main challenge is attributable to disordered optical scattering which scrambles the optical field of light from different optical paths. In the last decade, optical wavefront shaping has made great progress to control light through complex disordered scattering media for imaging and focusing [1, 2, 3, 4, 5, 6]. This class of techniques first measures the optical phase or complex field of light from different scattering paths and then actively manipulates the output field by shaping an input wavefront. This active control of optical wavefronts has become a powerful and standard technique to manipulate light through disordered scattering media.

While different versions of optical wavefront shaping techniques have been developed, they almost always require phase measurement and spatial light modulation1–6. During the phase measurement process, interferometry of various forms is used to extract the phase information of the scattered light, either directly using holo-

graphic methods or indirectly using phase retrieval techniques. Then, knowledge of the phase information is used to display a pattern on a spatial light modulator which controls the propagation of light through many optical channels in parallel so that a desired optical pattern is obtained through the scattering medium by interference between all of the modulated optical paths. It is important to note that regardless of whether amplitude or phase modulation is used, traditional wavefront shaping techniques always exploit the phase relationship between different optical channels to form the desired output pattern since the output pattern is formed by interference.

This principle means that optical wavefront shaping requires knowledge of the phase relationship between the input and output planes of the scattering medium. Mathematically, the optical fields on the input plane and the output plane are related by a complex matrix called the transmission matrix [5, 7]. Since a typical transmission matrix can contain millions of entries or more, measuring both the real and imaginary parts of all the entries is a challenging task since optical detectors measure only intensity information, requiring the use of interferometric techniques such as phase-shifting or off-axis holography. Because of this challenge, a large research effort has been devoted to improving the speed and stability of complex transmission matrix characterization [8, 9].

Given the complexities associated with measuring the phase relationship between different channels for wavefront shaping, it is worth asking whether the ends justify the means. Wavefront shaping can effectively transform a scattering medium into an optical lens by actively measuring and realigning the phase of the light from individual paths, but is the knowledge of the optical phase a prerequisite for manipulating light through scattering media? While the answer from conventional wisdom is yes, here we report new findings that challenge this assumption. We report a new optical approach that allows us to manipulate light through complex media without knowledge of the complex transmission matrix or the use of wavefront shaping. This method characterizes the optical intensity channels of the scattering medium by simply measuring the intensity of the optical speckle pattern transmitted through the scattering medium. Once we obtain the map of the optical intensity channels, we can control the light intensity and transmit information through the scattering medium using a linear combination of the modulated light through these optical channels. We call this method optical-channel-based intensity streaming (OCIS). Since phase information is not required, OCIS simplifies the complex field measurement to a direct intensity measurement. This new concept expands our understanding of light

control through scattering media and introduces new strategies to overcome and use optical scattering. In practice, since no interferometer, phase reconstruction, or spatial light modulation is required, the approach is remarkably simple to implement and can operate at high speeds. The reference-free feature of OCIS is useful in practical applications such as remote communication through scattering media.

In this work, we first explain the concept of optical intensity channels and the approach for performing incoherent and linear operations with them. This concept is further generalized with an intensity transmission matrix framework based on the transmission matrix theory from wavefront shaping. We then experimentally demonstrate the ability of this method to form a focus pattern with feedback-based OCIS. We derive the relationship between the number of controllable modes and the contrast-to-noise ratio (CNR) of the focus pattern and experimentally demonstrate the operational speed. Interestingly, OCIS is also able to form an energy null spot, a function that is difficult to achieve with wavefront shaping approaches due to the presence of naturally occurring dark speckles [10, 11]. We then move on to report on the optical intensity transpose, an OCIS-derived technique that uses optical speckle intensity information transmitted from a point source through a scattering medium to identify the optical channels of the scattering medium and to send light back to the location of the point source through these optical channels. Finally, using the linear operations provided by the intensity channels, we demonstrate a practical application of OCIS – scattering medium mediated secure optical information transmission. OCIS can provide a means to directly transmit information through scattering media in a secure way without requiring a prior secure channel.

4.2 Principle

To help understand the principles of OCIS for optical control through scattering media, let us imagine a scenario where a coherent light beam from a point source at position P1 is incident on and transmits light through a scattering medium (Fig. 4.1a). A laser speckle pattern will develop behind the scattering medium as a result of the mutual interference of multiple scattering paths [12]. The speckle intensity is randomly distributed, and let us assume that a bright speckle is developed at position P2 and a dark speckle is developed at position P3 (Fig. 4.1a). Whether a speckle is bright or dark depends on the degree of alignment (i.e., the degree of constructive or destructive interference) between the phasors representing the field contribution from different optical paths through the medium. The bright speckles result from situations where the phasors are more strongly aligned than on average

(i.e., relatively constructive interference), forming a longer-than-average resultant phasor, and the dark speckles from the situations where the phasors are more weakly aligned than on average (i.e., relatively destructive interference), forming a shorter-than-average resultant phasor.

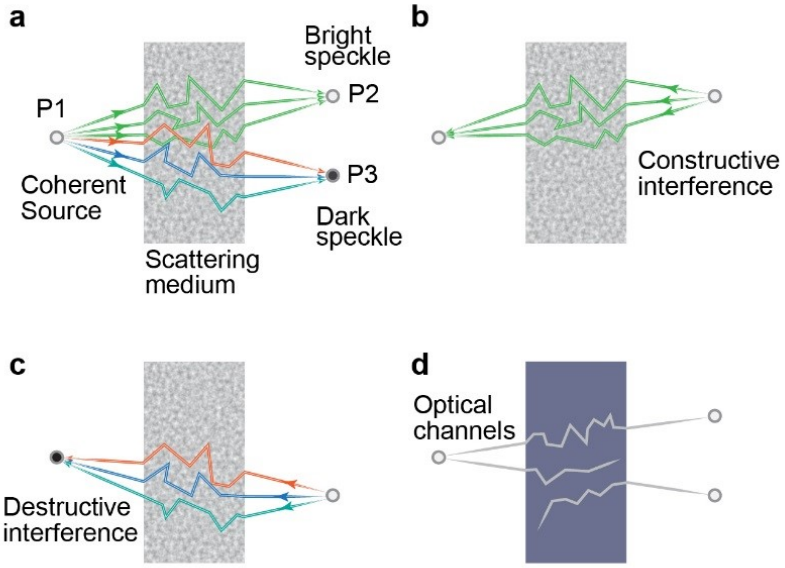

Figure 4.1: Optical intensity channels. (a) A coherent source or guidestar at position P1 on the target plane leads to a bright speckle at position P2 and a dark speckle at position P3. In the case of a bright speckle, the majority of the optical paths share a similar phase (denoted by the same color) and thus relatively constructively interfere. In contrast, the optical paths leading to the dark speckle are out of phase (denoted by different colors). (b) and (c) Based on the time-reversal symmetry of optical propagation, a bright speckle at position P2 will also lead to a bright speckle at position P1 (b). However, a bright speckle at position P3 will not result in a bright speckle at position P1 due to destructive interference (c). (d) This phenomenon is interpreted in a picture of optical channels. An optical channel is established between position P1 and P2 for optical energy transmission while there is no optical channel between position P1 and P3.

In the example presented in Fig. 4.1a, the relatively constructive interference occurring between light from the majority of optical paths that connect positions P1 and P2 forms a bright speckle at P2, whereas the relatively destructive interference of light occurring between the different paths that connect P1 and P3 forms a dark speckle. The time-reversal symmetry of optical propagation also means that if we place the light source at position P2, the light will follow the same trajectories to reach position P1 (Fig. 4.1b). Since the phase relation between these optical paths is

maintained, relatively constructive interference occurs at position P1. Similarly, if we move the light source to position P3, destructive interference occurs at position P1 because the phase relationship between the optical paths remains the same regardless of the propagation direction of the light (Fig. 4.1c). We can abstract the above analysis to a picture of optical channels (Fig. 4.1d). An open optical channel is established between the position P1 and P2 while the optical channel that connects position P1 and P3 is closed. We can then generalize this relationship to the entire target plane where the intensity of a speckle maps to the throughput of the associated channels. The concept of optical intensity channels forms the foundation of OCIS, which allows us to manipulate light through scattering media by learning and modulating the intensity of light through the optical channels.

It should be noted that the concept of optical intensity channels here differs from the channels described in optical wavefront shaping theory [13] since here knowledge of optical intensity alone is required, instead of information about the complex field. Mathematically, we can describe OCIS with an intensity transmission matrix. This mathematical theory mirrors the complex optical field transmission matrix theory that is extensively used in wavefront shaping methods [5, 7].

To understand OCIS in the framework of an intensity transmission matrix, we start by examining the complex optical field transmission matrix mathematical framework [5, 7]. In this case, the optical fields on the input plane and the target plane can be discretized into complex row vectors $\mathbf{u}$ and $\mathbf{v}$, respectively, and connected by a transmission matrix $\mathbf{T}$ through the equation $\mathbf{v} = \mathbf{uT}$. The optical field on the target plane is a linear transform of the field on the input plane. However, the intensity on the target plane, which is of interest in most applications, is not linear with respect to the intensity of the shaped optical field.

OCIS aims to simplify this nonlinear relationship by directly connecting the input intensity to the output intensity in a linear form through an intensity transmission matrix $\mathbf{S}$ of the form

$$\mathbf{b} = \mathbf{aS}, \tag{4.1}$$

where $\mathbf{a}$ and $\mathbf{b}$ are row vectors denoting the intensity of the optical patterns on the input plane and output plane, respectively. Each element of $\mathbf{a}$ and $\mathbf{b}$ represents the intensity value of an optical mode. This equation is valid if the input modes are spatially incoherent with each other so that the intensity of each output mode is a linear combination of the intensity values of these input modes. In this case, the $(i, j)th$ element of $\mathbf{S}$ is equal to the magnitude square of the $(i, j)th$ element of $\mathbf{T}$, and

thus all elements of **S** are real and non-negative. While complex transmission matrix theory interprets light propagation through scattering media on a fundamental level, the intensity transmission here serves as an intuitive and efficient tool to analyze linear and incoherent operations.

There are two primary ways by which we can satisfy the condition that the spatial modes on the input plane are spatially incoherent and do not mutually interfere with each other. The most direct way is to use a spatially incoherent light source on the input side. Alternatively, we can sequentially illuminate each input spatial mode. In this case, time separation can also guarantee that cross-modal interference does not occur. In our experiment, we demonstrated the use of these two approaches to linearly and incoherently operate on the intensity channels. In the following sections, we will demonstrate a series of experimental implementations of OCIS to overcome optical scattering and transmit information through disordered scattering media.

Feedback based OCIS

Here we apply the principle of OCIS with a feedback mechanism to form a focus pattern through a scattering medium, an important evaluation of the ability of this technique to overcome optical scattering. The requirement for a feedback mechanism here shares similarity with feedback-based wavefront shaping [14]. The implementation of feedback-based OCIS can be divided into two steps: measurement and display. During the measurement process, OCIS aims to find the optical channels between the input plane and the target spot. In this case, one can use a CW laser source to illuminate the scattering medium with different optical modes, e.g. scanning spatially over time as shown in Fig. 4.2a1. By simply measuring the optical intensity feedback as the laser beam scans, one can learn the optical channel mapping between the scanning position on the input plane and the target spot. During display, we simply inject light only into the optical channels that connect the input plane and the target spot as shown in Fig. 4.2a2. Although part of the light also couples to other channels that are connected to other positions on the target plane, the total light intensity on these positions is on average lower than that on the target spot.

We now use the intensity transmission framework to analyze feedback-based OCIS. During the measurement step, we sequentially send in the basis input vectors, which form a matrix **A** (Fig. 4.2b1, left matrix). In our case, we input single modes (i.e.,

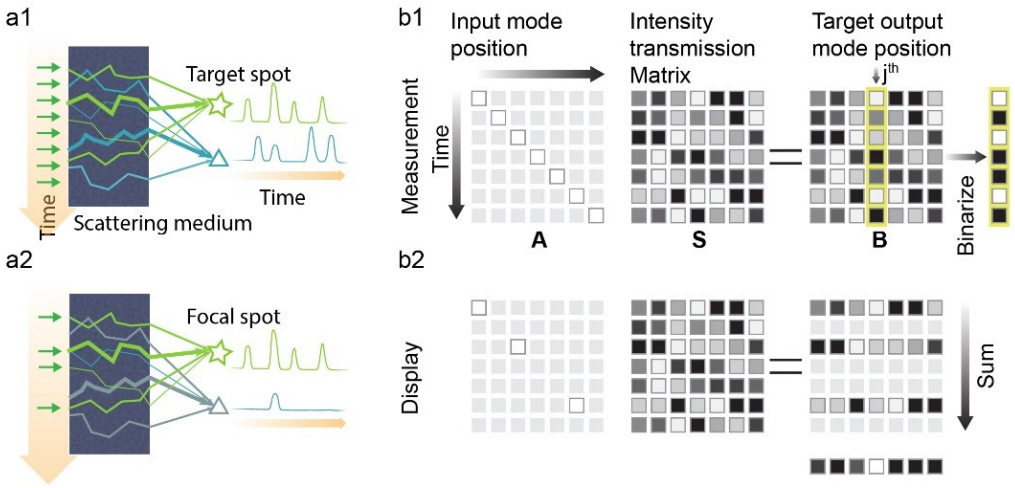

Figure 4.2: Principle of feedback-based OCIS. (a1) A coherent light source scans across the input plane of the scattering medium over time, resulting in time-varying intensity signals at the target spot on the target plane. At another spot (denoted by a triangle), the signals are uncorrelated with those at the target spot due to the random scattering of the light through the sample. These time-varying signals allow us to map the optical channels between the input plane and the target plane. (a2) By injecting light into the channels that connect to the target spot, a focus pattern is formed at the target spot while other spots on the target plane receive less light on average. (b) Matrix representation of the feedback-based OCIS. (b1) The incident optical mode sweeps through space over time, and can be represented by an identity matrix **A**. Its interaction with the scattering medium is represented by multiplying the intensity transmission matrix **S**, resulting in time-varying speckle patterns on the output. The measurement of the time-varying speckles at the target position is equivalent to taking one column of the intensity matrix **B**. (b2) During display, the binarized output selects a number of rows of **S** as output. The integration of the selected output rows over time results in an optical focus pattern at the target position.

$\mathbf{A}_i = \delta[i]$), where $\mathbf{A}_i$ denotes the i-th row vector of **A**, and $\delta[i]$ is a delta row vector with a nonzero value at the i-th element (e.g., $\mathbf{A}_1 = [1, 0, 1, ...][i]$). As a result, by collecting the transmitted intensity patterns over time, we obtain an output matrix **B** (Fig. 4.2b1, right matrix) that maps to the intensity transmission matrix **S**. The time-encoded intensity measured at the j-th location on the target plane indicates the throughput of the optical channels that connect the corresponding input mode to this location.

To enhance the temporal average intensity at the j-th location on the target plane, we select a subset of the row vectors of **A** where each row vector $\mathbf{A}_i$ connects to a

high-throughput channels to the j-th column of $\mathbf{B}$. We denote the set of row vector indices obtained using the feedback-based OCIS as CFB. We then sequentially send light to these channels and integrate the output intensity patterns (Fig. 4.2b2) to avoid mutual interference between different channels. Mathematically, the target pattern formed by feedback-based OCIS is given by

$$\mathbf{b_{FB}} = \sum_{i \in C_{FB}} \mathbf{B}_i = \sum_{i \in C_{FB}} (\mathbf{A}_i \mathbf{S}). \tag{4.2}$$

Mathematically, Eq. 4.2 can be further rewritten as

$$\mathbf{b_{FB}} \sum_{i \in C_{FB}} (\mathbf{A}_i)\mathbf{S} = \mathbf{a_{FB}}\mathbf{S}. \tag{4.3}$$

where $\mathbf{a_{FB}}$ is the summation of the input mode intensities in time. This equation is in agreement with Eq. 4.1, which justifies the use of temporal separation approach to realize the requirement of spatial incoherence.

With this mathematical framework in place, we can quantitatively evaluate the performance of OCIS based on speckle statistics. The contrast-to-noise ratio (CNR), which is defined as the ratio between the background-subtracted, time-averaged, spatial-peak intensity and the standard deviation of the background, is a reasonable metric because it evaluates both the peak intensity of the temporal average pattern and the fluctuation of its background. Assuming the instantaneous speckle patterns, i.e, the rows of the intensity transmission matrix, are fully developed [12], and the total number of uncorrelated speckle patterns that the OCIS system can measure and control is N (i.e. the number of rows in $\mathbf{S}$), the expected CNR of the optical spot pattern is given by

$$CNR = \sqrt{N} \exp(-\frac{I_t}{2\mu}) \frac{I_t}{\mu}, \tag{4.4}$$

where I_t is the intensity threshold and μ is the mean intensity of the speckle (i.e., the mean of the intensity transmission matrix $\mathbf{S}$). A step-by-step derivation of Eq. 4.4 is provided in Section 4.5. As the total number of measured frames N increases, the background becomes more uniform, the CNR increases, and the resulting optical spot becomes more pronounced. Therefore, this metric indicates the ability of OCIS to overcome optical scattering and to recover optical information through scattering media.

Another metric that is widely used in optical wavefront shaping is peak-to-background ratio (PBR) or intensity enhancement factor, which is defined as the ratio between

the peak intensity and the mean of the background. The PBR of OCIS is given by

$$PBR = 1 + \frac{I_t}{\mu}. \tag{4.5}$$

A detailed derivation of Eq. 4.5 is included in Section 4.5. As shown in Eq. 4.4 and 4.5, we can choose the intensity threshold I_t to optimize either CNR or PBR (See Section 4.5).

In wavefront shaping for optical focusing through scattering media, the PBR and CNR of the focus are equal except for a constant offset of 1 (PBR = CNR+1), for fully developed background speckle patterns. This fixed relationship stems from the fact that the background follows well-defined speckle statistics, where the mean and standard deviation of the background are the same value. In comparison, the PBR and CNR are quite different quantities in OCIS because the background mean is decoupled from its variance. A more detailed discussion of CNR and PBR can be found in Fig. 4.6. Different with wavefront shaping, both CNR and PBR are required here in OCIS to comprehensively characterize the quality of the focus pattern. CNR indicates the peak value and background variance, which determines the visibility of the focus pattern, while PBR indicates the energy enhancement on the targeted optical spot. For OCIS, CNR provides a better gauge of the signal-to-noise ratio than PBR in strong light scenarios (See Section 4.5 for more details). Since most of our experiments were performed at high light intensity levels, we chose to optimize CNR instead of PBR for optimal performance. We do note that in low light scenarios, PBR becomes the more relevant gauge of the signal-to-noise ratio for OCIS.

We next report our experimental findings on the controlling capability and speed of feedback-based OCIS. A simplified signal diagram is shown in Fig. 4.3a and the detailed experimental setup is described in the Methods section and shown in Fig. 4.7a. During measurement, a CW mode laser source illuminates the scattering medium (a ground glass diffuser, see Methods). We use a single photodetector with an active area comparable to the size of a single speckle grain to measure the temporal speckle intensity of the target point at the target plane during one galvo mirror sweep of time duration t (Fig. 4.3a1). We can then apply an intensity threshold to the time trace and identify a subset of optical channels that contribute bright speckles at the target location. During the display step (Fig. 4.3a2), we use this information to selectively turn on the laser illumination only at time points when this subset of speckle patterns is reproduced during a repeated galvo mirror scan. Since all the

selected speckle patterns show a brighter-than-threshold speckle at the target point, the temporal average optical intensity at the target point can then be expected to be higher on average than that of the background. Although the instantaneous intensity may fluctuate within the time period of t, i.e. the galvo mirror single trip scan duration, the temporally averaged optical spot can, nevertheless, effectively fulfill the role of a wavefront-shaping-based focused spot in many applications such as imaging or target localization, as long as t is shorter than 1) the decorrelation time of the scattering medium and 2) the application's signal integration time frame.

Because only intensity information is measured and modulated, the implementation of feedback-based OCIS can be extremely simple and fast. We used a comparator circuit to identify the high intensity speckles measured by the photodiode and streamed the digital signal (Fig. 4.8 and 4.9) to a field programmable gate array (FPGA) that was synchronized with the galvo mirror. During the display process, a last-in-first-out (LIFO) module in the FPGA was used to time-reverse and output the signal as the galvo mirror swept back. In this case, the output signal from the FPGA modulated the laser. In our experiment, a galvo mirror of 4 kHz was used, meaning that an optical spot was created within 250 μs. This all-hardware-based OCIS system is able to measure and control 8×10^3 modes per millisecond.

A camera with exposure time covering a galvo mirror one-way sweep (125 μs) was triggered to capture the patterns on the target plane. Fig. 3b shows the patterns captured by the camera at various speckle decorrelation times. To demonstrate the performance of this technique in the presence of fast speckle decorrelation, we tuned the speckle decorrelation time by moving the scattering medium at controllable speeds. As shown in Fig. 4.3b, the visibility of the optical spot becomes lower as the speckle decorrelation time decreases. To quantify the CNR as a function of speckle decorrelation time, we calculated the CNR of the patterns and plotted them over the decorrelation time as shown in Fig. 4.3c. The CNR drops to 50% of the maximum at a decorrelation time of 200 μs, matching well with the period of the galvo mirror, 250 μs.

The ability of OCIS to form a focus pattern can be generalized to arbitrary intensity control through scattering media by modulating the light intensity through the optical channels. One notable scenario is the generation of a null energy spot at a target point. In principle, the generation of a null energy spot through wavefront shaping is possible [10, 11]. Practically, a wavefront-shaping-based null energy spot has very limited practical utility – a natural speckle field is populated with numerous null

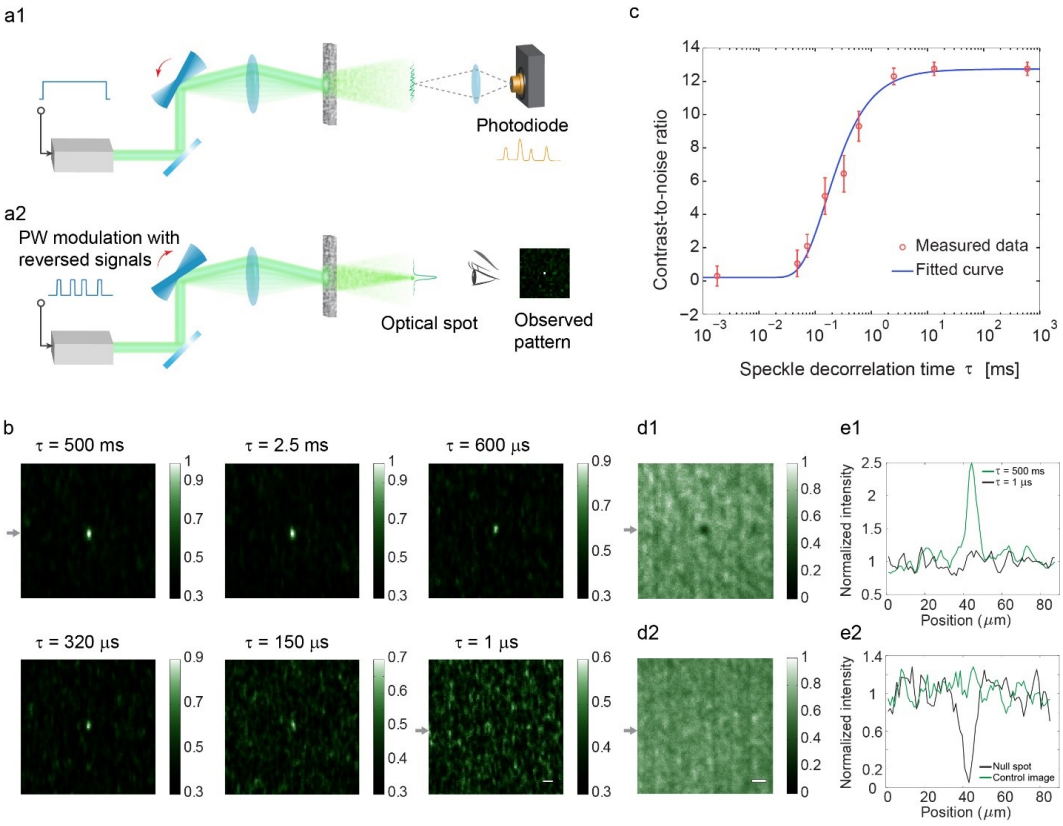

Figure 4.3: Results of the feedback-based OCIS. (a) Simplified system setup. (a1) Measurement. A galvo mirror was used to steer light into different channels of the scattering sample. As the galvo mirror scanned forward, the photodetector measured the temporal signal that fluctuated as light coupled into different channels. (a2) The measured signal was binarized and used to modulate the intensity of the laser in a time-reversed order as the galvo mirror scanned backward. In this case, we can measure the optical channels and inject light into the high-throughput channels during a galvo mirror round trip. (b) At different sample decorrelation times, optical spots were created in free space and captured by a camera with an exposure time of 125 μs. The CNRs for τ from 500 ms to 1μs are 12.6, 12.3, 9.3, 6.5, 5.1, and 0.3. Scale bar: 20 μm. (c) CNR as a function of the sample decorrelation time. (d) Feedback-based OCIS for null energy display. (d1) By injecting light into the low-throughput optical channels instead of high-throughput ones, we can obtain a null energy spot on the target plane. (d2) Control image. By sending light into randomly selected channels, no null energy spot was observed. Scale bar: 20 μm. (e1) Line plots of the arrow-indicated lines in (b, τ = 500 ms and 1 μs), normalized by the mean value of the background. (e2) Line plots of the arrow-indicated lines in (d), normalized by the mean value of the background.

spots due to deconstructive interference and an engineered null energy spot would not have a significant distinction from those spots. OCIS has an intrinsic capability to form a null energy spot of high visibility because it incoherently sums up speckle patterns and provides an averaged flat background.

Implementation-wise, the generation of a null energy point with OCIS simply requires that we negate the high-throughput optical channels between the incident plane and the target spot and send light to the low-throughput channels. We demonstrate this effect in the following experiment. Similar to the feedback-based OCIS for forming an optical spot through a scattering medium, we measured the binarized temporal speckle intensity through a scattering medium (see Methods) during the measurement step. Unlike the display process to form an optical spot where we chose the bright speckles, here we inverted the measured logic signals to choose the dark speckles, which subsequently modulated the laser source as the synchronized galvo mirror scanned backward. As such, a null energy spot was observed on the time-integrated pattern with a PBR of 5.0×10^{-2} and a CNR of -5.1 (Fig. 4.3d1, Fig. 4.3e2). To capture a control image, we randomly selected a subset of speckle patterns during display, and no null energy spot was observed (Fig. 4.3d2, Fig. 4.3e2). A quantitative derivation of the CNR and PBR of null energy spot patterns is included in Section 4.5.

The process of speckle pattern selection and summation here shares similarity with the operational process of ghost imaging [15]. However, there are fundamental distinctions between these two methods. First, ghost imaging measures speckles in free space and is not related to the optical channel theory while OCIS is a method to overcome or utilize disordered scattering. Second, ghost imaging reconstructs images computationally while OCIS is able to physically form images (See Section 4.5).

Optical intensity transposition

The ability to measure light transmitted from a point through a scattering medium and to find an optical solution that can send light back through the scattering medium to the original point (e.g. Fig. 4.4a) is highly sought for practical applications. In combination with guidestar techniques [3], this ability can potentially allow controlled concentrating of light energy within and information transmission through a scattering medium. To date, optical phase conjugation is the dominant wavefront shaping approach to perform such a function [16, 17]. As such, the phase conjugation

operation has long been assumed to be vital for retroreflecting light through or inside scattering media.

Surprisingly, OCIS provides an alternative and simple approach to accomplish the same objective – we name this approach optical intensity transposition. Moreover, OCIS accomplishes this objective without requiring phase measurements or the use of phase conjugation. To better understand the approach, we refer back to the intensity transmission matrix theory. From this theory, we can see that the index set C_{BF} or the target column vector of the intensity transmission matrix records the throughput of the optical channels between the input plane and target spot. Interestingly, the feedback-based OCIS method is not the only way to obtain this information about the optical channels. One can also utilize a point source on the target plane, which can be formulated as a delta column vector $\hat{\delta}[j]$ (Fig. 4.4c1, right column; the symbol$\hat{}$denotes column vector), to probe the target column of the intensity transmission matrix, that is $\hat{\mathbf{S}}_j = \mathbf{S}\hat{\delta}[j]$, in which $\hat{\mathbf{S}}_j$ is the j-th column of the intensity transmission matrix $\mathbf{S}$. In this case, we can directly obtain the target column $\hat{\mathbf{S}}_j$ on the input plane (Fig. 4.4c1) as the response of the delta function on the target plane. By measuring and thresholding this column vector, we are able to obtain the index set COIT with the optical intensity transpose method, which is the same as the CFB. Once we have the information about the optical channels, we can follow the same procedure as feedback-based OCIS to control light intensity through scattering media, e.g. forming an optical spot on the target plane (Fig. 4.4c2), which is mathematically described in Eq. 4.2. Interestingly, we can also playback all the modes simultaneously provided that they are spatially incoherent. Similar to Eq. 4.3, the summation of the selected intensity patterns on the input plane, $\mathbf{a_{OIT}} = \sum_{i \in C_{OIT}} \mathbf{A}_i$, is the transpose of the binarized column vector $\hat{\mathbf{S}}_j$, justifying the name of optical intensity transposition. As a comparison, optical phase conjugation plays back the conjugate transpose of the measured column of the complex transmission matrix.

We demonstrate this concept by the following experiment. Similar to optical phase conjugation, optical intensity transposition also starts with a coherent light source or a guidestar point [3] on the target plane behind the scattering medium (Fig. 4.4b1). The resulting optical pattern on the detector plane after scattered by the scattering sample carries important information about the scattering characteristics of the medium. Instead of recording the complex field or its phase map, here we only record the intensity information. In this case, we scan a galvo mirror placed at the Fourier plane of the detector plane to convert a spatial intensity pattern into a

temporal intensity signal and record the signal using a photodetector (Fig. 4.4b1). See Methods and Fig. 4.7b for more details on the setup. In the playback step, instead of using a spatial light modulator to display a conjugated optical wavefront, here we simply turn on the light source when the backward-scanning galvo mirror rotates to the positions where bright speckles were measured on the detector plane during recording. This process can be easily achieved by modulating the light source with the time-reversed signal as the galvo mirror scans backward (Fig. 4.4b2). By integrating the playback pattern over the backward scanning period on a camera, we observe an optical spot on the camera (Fig. 4.4d1). In other words, we "refocus" light through the scattering medium to the origin by simply reflecting the light back without the need to consider and manipulate the phase information. As a control experiment, we mismatched the timing between the phase of the galvo mirror and the modulation signal, and captured a control pattern as shown in Fig. 4.4d2.

It is worth noting that wavefront shaping with amplitude-only modulation such as with digital micromirror devices (DMD) can also include similar operations - intensity measurement, thresholding, and modulation [18]. However, these two methods are different on a fundamental level. Binary amplitude modulation still exploits interference between the modulating pixels and therefore, is still a phase-based approach. As phase and interference are involved, a reference beam, parallel spatial modulation, and finely-tuned alignment are all necessary with DMD-based phase conjugation. The underlying principle of OCIS is based on the linear operation on the intensity instead of the complex field in wavefront shaping including DMD-based phase conjugation.

Secure optical information transmission through scattering media

Disordered optical scattering scrambles the propagation directions of photons. In optical imaging, this effect broadens the point spread function and prevent optical information to be localized or resolved precisely through scattering media. In free-space optical communication, the spreading of the photons due to optical scattering prevents the information to be confined privately or delivered specifically. In this case, the optical scatterers act as tiny "beam splitters" that duplicate and broadcast the optical information to the public.

Conventionally, a separate key is used to secure information transmission. In this case, a private channel is first established to allow the communication participants to share the key. The key is then used to encrypt the information to be transmitted

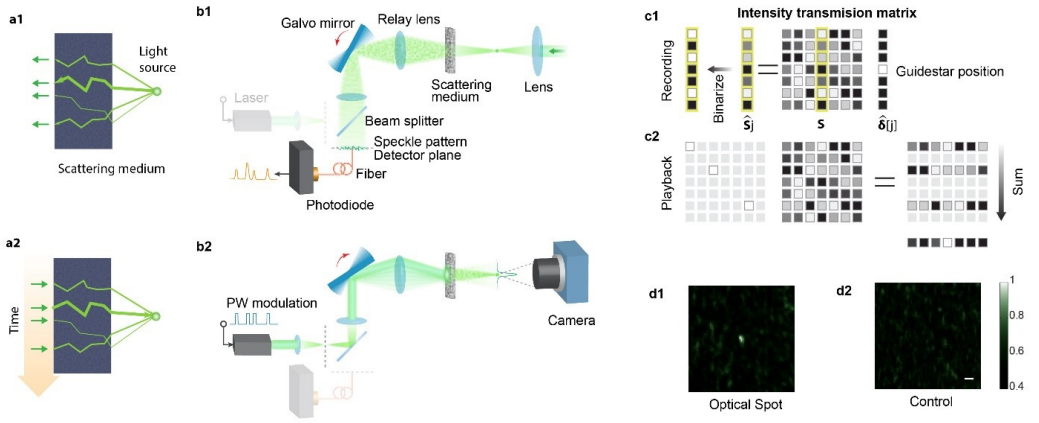

Figure 4.4: Optical intensity transposition. (a) The principle of optical intensity transposition. (a1) Light emitted from a coherent light source at the target plane traverses the optical channels to the input plane. By measuring the light intensity of the transmitted light as a function of space, we can obtain a spatial map of the optical channels. (b2) By sending light back through the high-throughput channels and linearly combining the transmitted light, we can obtain a focus pattern at the source location. (b) Experimental setup. Similar to optical phase conjugation, the retroreflecting process can be separated into two steps. (a1) Recording. A point source transmits light through the scattering medium and a photodiode measures a one-dimensional speckle pattern during one galvo mirror sweep. (a2) Playback. The measured signal is time-reversed and then modulates the laser on the input side as the galvo mirror scans backward. An optical spot is created at the position of the initial point source. (c) Matrix representation of optical intensity transposition. During recording (c1), a guidestar selects a column of the intensity transmission matrix as a time-varying intensity output, which is then binarized. During playback (c2), the binarized signal is used to select the corresponding rows of the intensity matrix, whose sum leads to a bright optical spot at the guidestar position. (d) Experimental results. An optical spot pattern was imaged on a camera with optical intensity transposition (d1), while no bright spot was observed in the control experiment where we disabled the synchronization between the playback sequence and the galvo mirror (d2). Scale bar: 20 μm.

in a public channel. Only the receivers with the key can decode the encrypted information. Of particular interest to mention here are the previous works on using optical approaches to generate random keys [19, 20, 21, 22].

Recently, optical wavefront-shaping-based approaches have been demonstrated to address the non-specific transmission of optical information due to optical scattering. Instead of using a separate digital key for encryption, this method takes advantage of the random scattering itself to “encrypt” the optical information [23]. In this case,

the scrambled optical information due to optical scattering can only be recovered by the measured complex transmission matrix of the scattering.

Here, we demonstrate one potential use of OCIS in optical communication through scattering media. There are two main advantages of using OCIS for private communication with the presence of optical scattering. First, a separate random key generator and a private channel are not required although they are compatible with OCIS for an additional layer of security. Second, prior measurement of the complex transmission matrix is not required either, which is important for remote communications where complex field measurement is challenging.

To understand the principle of OCIS-based information transmission through scattering media, we consider a scenario where person A (Alice) and person B (Bob) try to communicate to each other in a non-line-of-sight environment such as through fog, through turbid water, or around the corners. The scattering medium can also take the form of a multimode fiber. Similar to the optical intensity transposition described in the previous section, Alice will first illuminate the scattering medium with a point source to establish the channels. Bob will then measure the transmitted speckle pattern on a camera. Each bright speckle spot on the camera will represent a bright channel through the scattering medium back to Alice's initial point source. In other words, if Bob places a point source at that bright speckle location, Alice will receive a bright speckle. The opposite is true for the dark speckle spots on Bob's camera. Placing a point source at one of these dark points will cause Alice to receive a dark speckle. The relationship allows Bob to send a '1' bit (or '0' bit) by injecting photons to bright channels (or dark channels) as shown in Fig. 4.5a2. As long as Bob only uses each channel once, the security of the communication channel would be preserved. An eavesdropper Chuck detecting light elsewhere will not be able to glean useful information as he will receive a speckle pattern that is uncorrelated with Alice and Bob's (See Section 4.5 for more details).

Figure 4.5b shows the schematic of OCIS-based free-space secure communications between communication parties Alice and Bob. Each of them used a ground glass diffuser as the scattering medium. During the channel establishment phase, a camera on Bob's side was used to record the speckle intensity pattern as a channel map (b1). Then a DMD, which was pixel-to-pixel matched with the camera, was used to select bright or dark channels depending on the logic values of the message to be transmitted (b2). To enhance SNR, we combined multiple channels simultaneously to transmit one-bit data. At the same time, the photodetector on Alice's side will

receive a binary intensity sequence that matches the original data. It should be noted that to avoid optical field interference between these channels, the light field on the DMD is spatially incoherent (see Methods and Fig. 4.7c for more details). The experimental results are shown in (Fig. 4.5c-f). The original data from Bob is a two-dimensional image (Fig. 4.5c), which was transmitted row by row to Alice. Each bit is either logic 1 or logic 0, which corresponds to a focus pattern or a null pattern described in Section Feedback based OCIS. The CNR is ~3.7 for the focus pattern and -1.5 for the null pattern. Upon reception by the photodetector on Alice's side, the data stream was reconstructed to an image (Fig. 4.5d), whose binarized version (Fig. 4.5e) matches the original data. In contrast, a photodetector that measured one speckle grain of the intercepted light, which mimics an eavesdropper Chuck, received a random sequence (Fig. 4.5f) that is uncorrelated with the original data.

To further enhance security, Alice can additionally shuffle the scattering medium (e.g. by rotating the diffuser) before her emitter and receiver to refresh the optical channel map intermittently. Effectively, secret and ever-changing channels are created between the sender and the targeted receiver, and information only streams within the channels. In addition, OCIS provides a physical layer of encryption that is highly compatible and complementary to the conventional digital key encryption. In the case where the digital key is hacked, OCIS serves as another line of defense, and vice versa. More details about the analysis on possible attacks and applicability of OCIS-based secure communications can be found in Section 4.5.

4.3 Discussion

OCIS opens up a new door to control light through scattering media. From the perspective of optical channels, wavefront shaping proactively measures and aligns the phase of light passing through each optical channel and therefore requires a significant amount of effort and time to process the phase information. In contrast, OCIS only needs to identify and modulate the intensity of light passing through the optical channels. The concept of OCIS extends our understanding of controlling light through scattering media. In addition, it comes with a number of important features.

First, the OCIS implementation is, in general, simple and fast because it requires only intensity information, which can be directly measured with typical optoelectronic devices. Its general simplicity versus the higher complexity of wavefront shaping

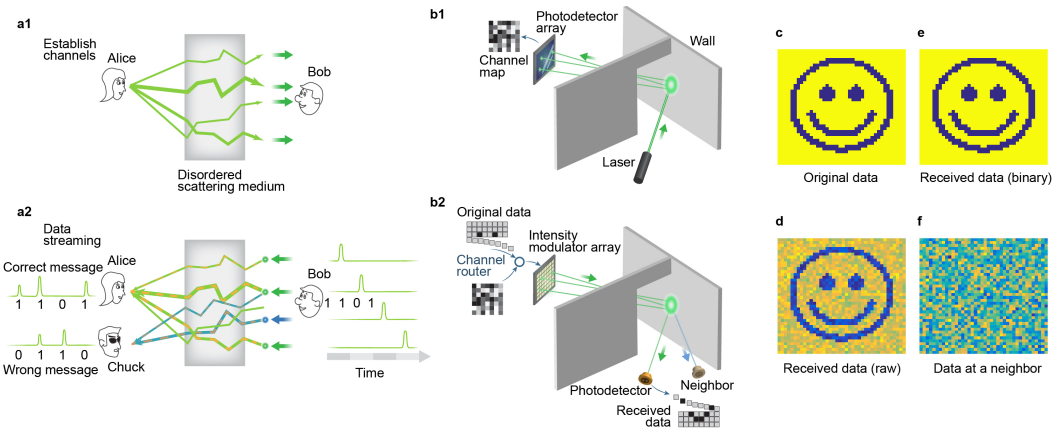

Figure 4.5: Secure communication with OCIS. (a) Conceptual illustration. OCIS enables secure free-space optical communications between communication parties Alice and Bob. (a1) Alice establishes optical channels between Alice and Bob by sending a laser pulse through the scattering medium. Bob measures the resultant speckle intensity pattern on the remote end to reveal the optical channels between Alice and Bob. (a2) To send a binary message to Alice, Bob streams spatially incoherent optical pulses through different channels of the scattering medium, e.g., logical ones to randomly selected open channels and logical zeros to randomly selected closed channels. As a result, Alice receives a matched message while a third person Chuck receives a random message because the channels between Bob and Chuck are uncorrelated with those between Alice and Bob. (b) Experimental demonstration of the OCIS-based free space secure communication. (b1) A laser beam transmits through a local diffuser and a remote diffuser. A photodetector array at the remote end measures the resultant speckle pattern as the map of the optical channels. (b2) An intensity modulator array is used to route the optical pulses to different channels based on the message and the measured channel map. Two photodetectors on the local side record the returned optical pulses. One of the photodetectors is conjugated to the laser while the other one is placed elsewhere. (c-f) Experimental results. (c) Original binary data. (d) Raw data received by the conjugated photodetector. (e) Binarized data of (d). (f) Raw data received by the neighboring photodetector.

implementations provides it with a speed advantage for a certain range of operation. We anticipate that the system speed can be significantly boosted by using much faster intensity modulation schemes such as amplitude modulation of diode lasers and using faster scanners such as swept source lasers. We further note that speed improvements are generally coupled with diminished photon budgets. An analysis of OCIS performance in the regime where shot noise becomes considerable is provided in Section 4.5. One significant disadvantage of OCIS versus standard wavefront shaping is that the PBR and CNR enhancements are weaker functions of

the number of controllable modes than those of wavefront shaping. OCIS's PBR is preset by choosing a threshold, and, as such, access to more control optical modes (N) only allows us to pick a higher threshold, optimizing PBR this way would yield ln(N) peak improvements. In comparison, PBR scales as N for wavefront shaping. This indicates that wavefront shaping should generally outperform OCIS in light starved scenarios (e.g. single photon regime) or when the goal is to achieve intensity enhancement. When photon budget is not a limiting factor and the goal is to recover information from random scattering, CNR which measures the peak to the noise fluctuations (rather than the background DC value) is actually a better gauge of the nominal SNR performance. By this measure, the CNR of OCIS scales as sqrt(N) while wavefront shaping scales as N.

Second, OCIS is intrinsically capable of displaying negative patterns. The generation of negative patterns through scattering media is, in principle, possible with wavefront shaping but highly impractical as the negative pattern created would be difficult to distinguish from naturally occurring null points in the speckled background. In contrast, because OCIS directly operates on an intensity basis instead of controlling interference, the background formed by OCIS exhibits a much less pronounced spatial variation. Similar to the formation of a bright spot, the controllable dark spot here also carries information through scattering media. In the secure communications application, the use of null spots to carry information is especially useful because it improves the overall signal-to-noise characteristics of the method.

Third, since OCIS directly operates on intensity, it is useful in some applications where phase measurement is difficult to achieve. In many practical cases such as free space optical communications through fog, cloud, turbid water, walls, or biological tissue, it is difficult to implement a reference beam. The demonstrated secure information streaming through scattering media is an application enabled by the reference-beam-free feature of OCIS.

Last but not least, OCIS can be implemented with spectral channels. In this case, different optical wavelengths provide different optical channels because the scattering properties are wavelength dependent. Instead of scanning through different spatial modes of the sample, one can also scan through the spectral modes to measure the throughput of the optical channels as a function of wavelength. Unlike wavefront shaping which requires multiple modes to be displayed in parallel simultaneously, spectral OCIS enables the use of a single mode fiber as the optical interface and therefore enables miniature optical devices.

4.4 Summary

With its ability to confine optical information locally and specifically, OCIS can be used for imaging through scattering media as we demonstrated in Section 4.5 and Fig. 4.11. With the same principle, OCIS can also be used in secure information transmission where it helps prevent optical information from spreading globally in optical information transmission through scattering media. While we demonstrated a free-space communication scenario, the OCIS can potentially be used with multimode fibers to secure information during transmission. OCIS provides a physical encryption that does not require the use of a digital key yet it is also compatible with the conventional digital key encryption and thus provides an additional layer of security. This flexibility enables OCIS in a wide range of optical information transmission applications.

In conclusion, we would like to close by noting that this work is an initial exploration of intensity-only-based modulation strategies for controlling light transmission through scattering media. As wavefront shaping operates on optical fields but most of the end applications concern only intensity, wavefront shaping intrinsically has to deal with the nonlinear, field-to-intensity conversion problem. OCIS simplifies this problem to a linear operation by directly operating on intensity, and thus may offer superior solutions in some applications.

4.5 Appendix

Supplementary figures

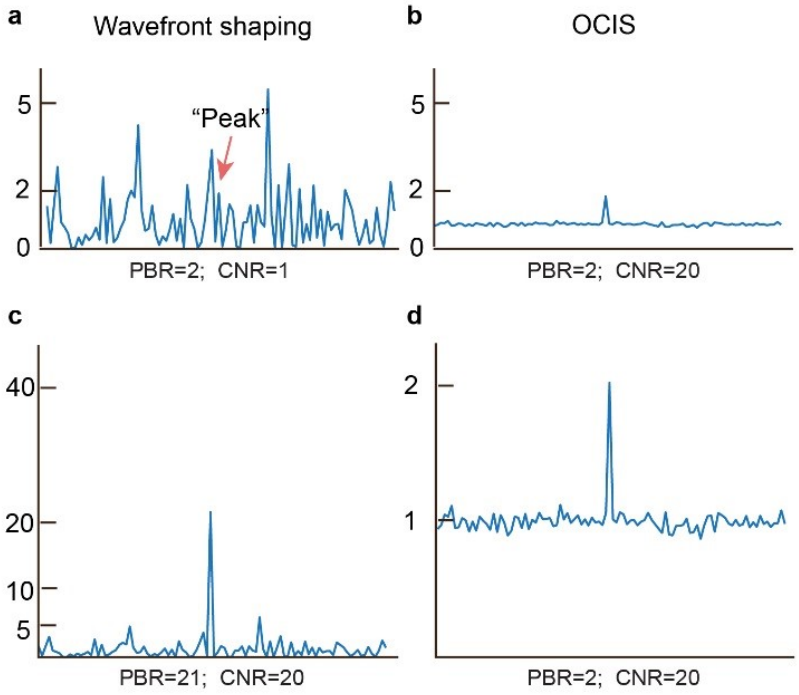

Figure 4.6: Simulation results for comparison of the metrics, peak to background ratio (PBR) and contrast of noise ratio (CNR), which evaluate the quality of a focus pattern. (a) In optical wavefront shaping, at low PBR, e.g. PBR=2, the peak is immersed into the background of fully developed speckles, where the standard deviation of the speckle intensity is the same as its mean. In this case, CNR=PBR-1=1. (b) For the same PBR, the time-averaged pattern created by OCIS shows a prominent peak as the variation of the background is much lower, resulting in a higher CNR, e.g. CNR=20 (~1000 controllable modes). (c) To obtain the same CNR as the pattern formed by OCIS, the PBR of the focus formed by the wavefront shaping techniques needs to increase to 21. (d) The pattern in (b) is rescaled to help visually compare to the pattern in (c). As shown in (c) and (d), as long as the CNR is the same, the visibility of the peak is very similar although they have a very different PBR. Therefore, CNR is a more useful metrics for OCIS.

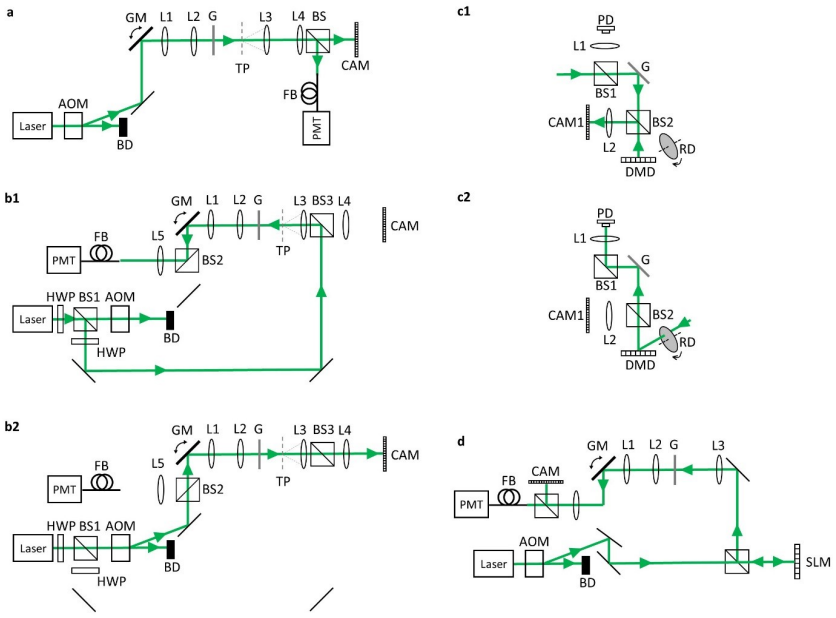

Figure 4.7: Experimental Setups. (a) Feedback based OCIS setup. (b) Optical intensity transpose setup, (b1) recording; (b2) playback. (c) Setup for direct imaging through scattering media. Abbreviations: AOM, acousto-optic modulator; BD, beam dump; BS, beam splitter; CAM, camera; DMD, digital micro-mirror device; FB, fiber; G, ground glass diffuser; GM, galvanometer mirror; HWP, half wave plate; L, lens; PD, photodetector; PMT, photomultiplier tube; RD, rotating diffuser; TP, target plane.

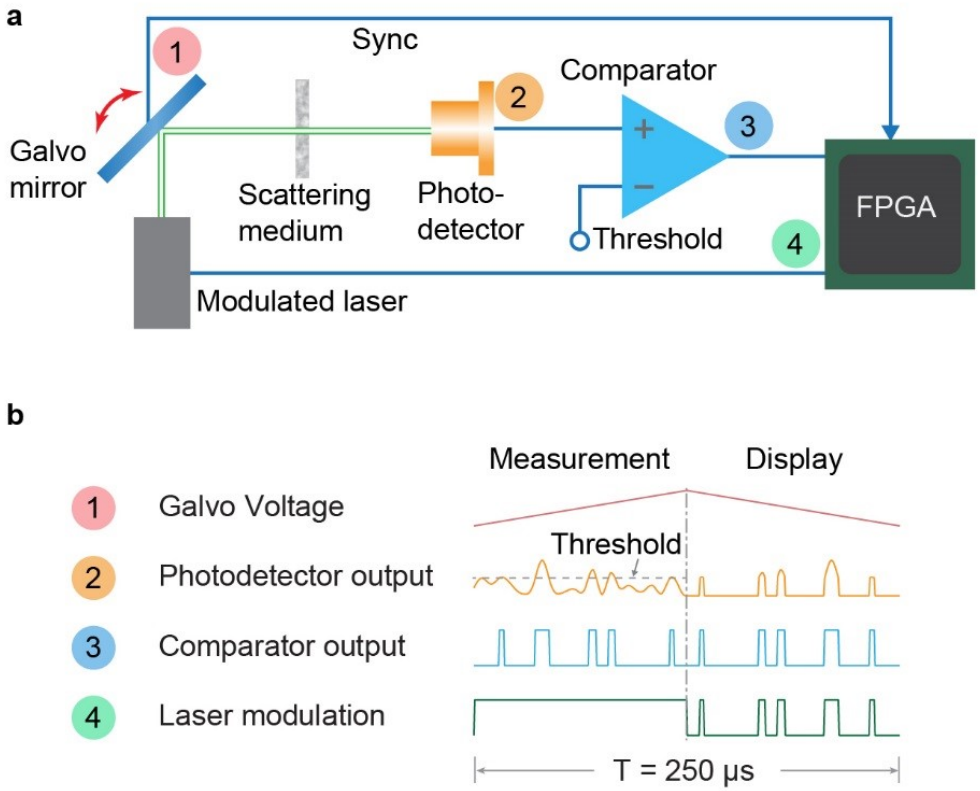

Figure 4.8: Experimental Setups. (a) Feedback based OCIS setup. (b) Optical intensity transpose setup, (b1) recording; (b2) playback. (c) Setup for direct imaging through scattering media. Abbreviations: AOM, acousto-optic modulator; BD, beam dump; BS, beam splitter; CAM, camera; DMD, digital micro-mirror device; FB, fiber; G, ground glass diffuser; GM, galvanometer mirror; HWP, half wave plate; L, lens; PD, photodetector; PMT, photomultiplier tube; RD, rotating diffuser; TP, target plane.

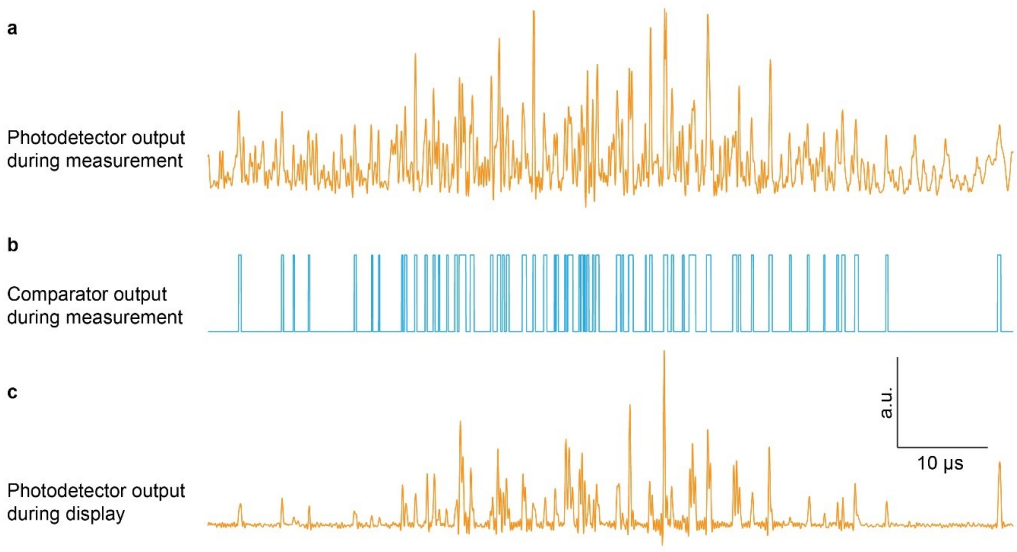

Figure 4.9: Experimental signal traces from the feedback-based OCIS. (a) A raw signal output from the photodetector during measurement. (b) A binarized signal output from the comparator during measurement. (c) A photodetector output signal during display. To provide a clearer visual comparison, we time-reversed this output signal again to match the timing.

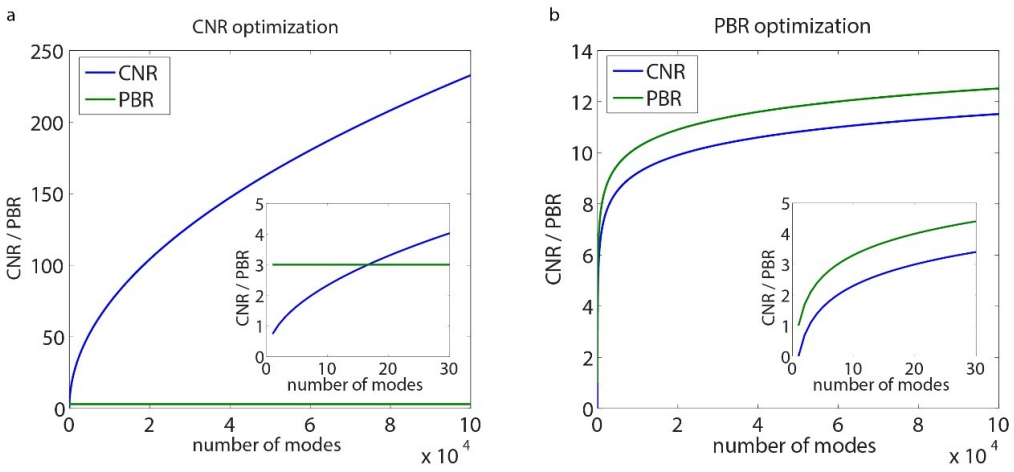

Figure 4.10: CNR and PBR as a function of number of controllable modes. (a) CNR optimization mode based on Eq. 4.12 and Eq. 4.13 S8. (b) PBR optimization mode based on Eq. 4.14 and Eq. 4.15

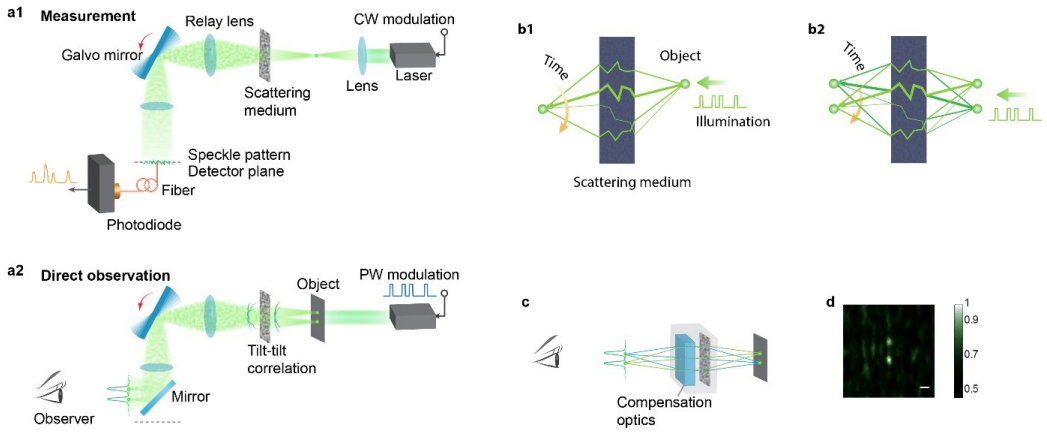

Figure 4.11: Direct imaging through a thin scattering medium with OCIS. (a) Experimental setup. This procedure can be separated into two steps. (a1) Measurement. This procedure is the same as the recording of the intensity reflection method described above. An optical spot was created on the target plane and a binarized speckle intensity is measured sequentially on the detector plane during a sweep of the galvo mirror. (a2) Direct observation. By using this signal to modulate the laser that illuminates a transmission object on the target plane, one can directly observe the object as the galvo mirror synchronizes with the modulated illumination. The method utilizes the angular memory effect of the thin scattering medium, where a tilted optical field incident to the thin scattering medium results in a tilted optical field on the other side. Therefore, the measured signal is also applicable to the neighboring points and enables direct observation of the object with only one measurement. (b) Optical diagram of the imaging process. (b1) Light from an object couples to different high-throughput channels over time and the transmitted light is directed to a spot to form a PSF of the imaging system. (b2) Based on the optical memory effect, a neighboring spot within the memory effect range also forms an image at the imaging plane. (c) Equivalently, OCIS and the scattering medium serves as an imaging system and one can see through the scattering medium directly. (d) An image of the object was formed through the scattering medium and captured by a camera on the detector plane. Scale bar: 10 μm.

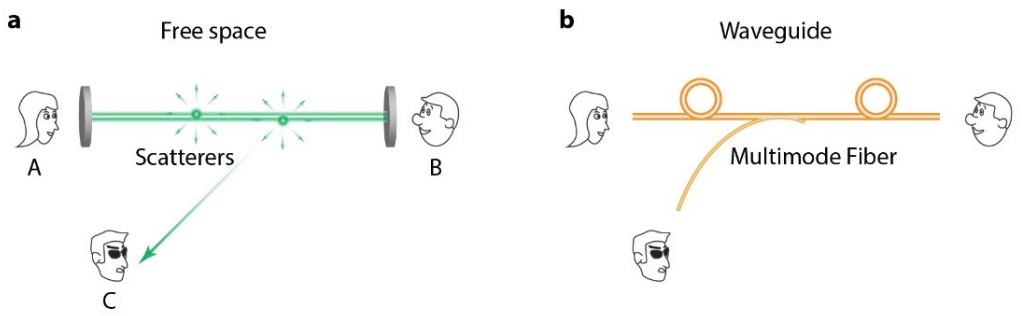

Figure 4.12: Optical information coupled out of the communication chain. (a) In free space, scatterers spread light to other directions. (b) In waveguide geometry, light can be coupled out of an optical fiber.

Supplementary notes

Experimental setups

The optical setup of feedback-based OCIS is shown in Fig. 4.7a. A collimated CW laser beam (532 nm wavelength, CrystaLaser Inc.) was intensity-modulated by an acousto-optic modulator (AOM, 100MHz, IntraAction Corp.) by taking the first order of the diffracted beam. The modulated beam was then scanned by a galvo mirror (CRS 4 KHz, Cambridge Technology), which was imaged onto the surface of a ground glass diffuser (DG10-120, Thorlabs) through a 4-f relay system (L1, L2). The light intensity on the surface of the diffuser was 20 mW. Another 4-f system (L3, L4) magnified the speckle to match the core diameter of the fiber. A photomultiplier tube (PMT, H7422, Hamamatsu) was used to measure the speckle intensity, and the output signal was sent to an analog comparator (LM361N, Texas Instruments). An FPGA board (Cyclone 2, Altera) that was synchronized with the galvo mirror received and processed the output signals from the comparator. The output signals from the FPGA controlled an electronic switch (ZASWA-2-50DR+, Mini-circuits) to modulate the amplitude of the carrier (100 MHz) to the AOM. A camera (GX1920, Allied Vision) was placed on the conjugate plane of the fiber to observe the optical patterns.

The optical setup of optical intensity transpose is shown in Fig. 4.7b. During the recording process (Fig. 4.7b1), lens L3 created an optical spot behind the ground glass diffuser and the optical spot was conjugated with the camera by a 4-f system (L3 and L4). The light from the optical spot was then scattered by the diffuser and the PMT recorded the intensity on the Fourier plane of the galvo mirror which was conjugate to the surface of the diffuser. During the playback process (Fig. 4.7b2), the collimated laser beam that was aligned to be conjugated to the fiber end was modulated by the AOM when the galvo mirror was scanning. In the same way as feedback-based OCIS, the FPGA received the binarized signals from the comparator and output the signals to control the AOM for OCIS.

The optical setup for realizing imaging through scattering media is shown in Fig. 4.7c. We used a ground glass diffuser, the same as the one used in feedback-based OCIS demonstration, as the backscattering surface. The camera measured a speckle pattern after light backscattered from the surface. During data streaming, we randomly selected ~300 sub-channels (corresponding to ~300 speckles) to form a channel. The light intensity modulation was realized with a DMD system (Discovery 4100, Texas Instruments). To assure linear intensity operation as described in the

intensity transmission matrix theory, the DMD modulates spatially incoherent light, which was scattered by a rotating diffuser in front of the coherent laser source.

Mathematical derivation of CNR and PBR

OCIS optical spot

Here we quantitatively evaluate the performance of OCIS techniques. Assuming the instantaneous speckle patterns are fully developed [24], the speckle intensity follows an exponential distribution with mean μ and standard deviation $\sigma = \mu$. The shot noise effect will be considered in the next section. The probability density function is given by

$$P(I) = \frac{1}{\mu} \exp\left(-\frac{I}{\mu}\right), \tag{4.6}$$

where μ is the mean intensity of the speckle pattern. Then, α, the portion of patterns in which the intensity value of the pixel of interest is higher than a threshold I_t is given by

$$\alpha = \int_{I_t}^{\infty} \frac{1}{\mu} \exp\left(-\frac{I}{\mu}\right) dI = \exp -\frac{I}{\mu}. \tag{4.7}$$

The mean intensity of the pixel of interest among these patterns is therefore given by

$$\bar{I}_p = \int_{I_t}^{\infty} I \times \frac{P(I)}{\alpha} dI. \tag{4.8}$$

Substituting Eq. 4.6 and 4.7 into Eq. 4.8 leads to

$$\bar{I}_p = \mu + I_t. \tag{4.9}$$

If our system captures N independent speckle patterns in total, the number of selected patterns is then approximately αN. Since the OCIS sums up all the selected patterns, the peak intensity of the resultant pattern on average is given by $\bar{I}_{sp} = \alpha N \bar{I}_p$, while the mean and standard deviation of the background of the resultant pattern is given by $I_{sb} = \alpha N \mu$ and $\sigma_{sb} = \sqrt{\alpha N}\sigma = \sqrt{\alpha N}\mu$. The contrast-to-noise ratio (CNR) is given by

$$CNR_P = \frac{\bar{I}_{sp} - \bar{I}_{sb}}{\sigma_{sb}} = \sqrt{\alpha N}\frac{I_t}{\mu} = \sqrt{N}\exp\left(-\frac{I_t}{2\mu}\right)\frac{I_t}{\mu}. \tag{4.10}$$

The PBR of OCIS is given by

$$PBR_P = \frac{\bar{I}_{sp}}{\bar{I}_{sb}} = \frac{\alpha N \bar{I}_p}{\alpha N \mu} = \frac{\mu + I_t}{\mu} = 1 + \frac{I_t}{\mu}. \tag{4.11}$$

From Eq. 4.10 and 4.11, we find that both CNR and PBR are functions of intensity threshold I_t that we choose. Therefore, by selecting a proper threshold, we can

optimize the CNR or PBR accordingly. Here we analyze the solutions for CNR and PBR optimization, respectively. The subscripts "A" and "B" in CNRs and PBRs below correspond to "a. CNR optimization" and "b. PBR optimization", respectively.

a. CNR optimization

Through optimization, we find that maximum CNR is achieved when the intensity threshold is set at double of the mean intensity, that is $I_t = 2\mu$. In this case, the CNR given by Eq. 4.10 becomes

$$CNR_{P\_A} = \frac{2}{e}\sqrt{N} \tag{4.12}$$

and the PBR given by Eq. 4.11 becomes

$$PBR_{P\_A} = 3. \tag{4.13}$$

In this case, PBR decouples from CNR and is a constant independent of the number of summed speckle patterns. In our experiment (Fig. 4.3b in the article, τ = 500 ms), we achieved a PBR of ~2.5.

b. PBR optimization

To maximize PBR, one would set I_t as high as possible as indicated by Eq. 4.11. However, the maximum I_t is bounded by the requirement that on average one speckle pattern is selected during display. This requirement can be describes as $\alpha N = 1$. Substituting α with Eq. 4.7, we find that the intensity threshold for PBR optimization is given by $I_t = \mu \ln N$. Substituting this equation into Eq. 4.11, we have the maximum PBR:

$$PBR_{P\_B} = 1 + \ln N. \tag{4.14}$$

Using this intensity threshold to calculate CNR based on Eq. 4.10, we have

$$CNR_{P\_B} = \ln N. \tag{4.15}$$

Equations 4.14 and 4.15 show that the PBR and CNR are coupled in this case. This relationship, $PBR = CNR + 1$, is the same as that in wavefront shaping because in both cases the intensity distribution of the background follows speckle intensity distribution where its mean intensity equals its standard deviation.

Figure 4.10 plots CNR and PBR as a function of number of measured optical modes. From this figure, we can find that in CNR optimization mode, CNR increases as

a function of number of optical modes while the PBR remains the same. The enhancement in CNR means that the optical spot is more evident, which is the key metric to evaluate the ability of an imaging technique. In contrast, PBR fails to indicate this ability in this mode as it remains constant over the number of optical modes. In the PBR optimization mode, PBR and CNR are coupled and thus both of them can be used to evaluate the performance of an imaging technique.

Null energy point

For an OCIS generated null energy point, the portion of speckle patterns being selected is given by

$$\alpha = \int_0^{I_t} \frac{1}{\mu} \exp -\frac{I}{\mu} dI = 1 - \exp(-\frac{I_t}{\mu}). \tag{4.16}$$

In this case, the expected intensity of the point of interest among the selected patterns is given by

$$\bar{I}_n = \frac{1}{\alpha} \int_0^{I_t} I \times P(I) dI. \tag{4.17}$$

By substituting the probability density function $P(I)$ with Eq. 4.6, we have

$$\bar{I}_n = I_t - \frac{I_t}{1 - \exp(-\frac{I_t}{\mu})} + \mu. \tag{4.18}$$

If the system measures N speckle patterns in total, the number of selected speckle patterns is αN, and therefore the expected intensity of the sum of these patterns at the null energy point is given by $I_{sn} = \alpha N \bar{I}_n$. Likewise, the expected intensity of the sum of these patterns at the background is given by $I_{sb} = \alpha N \mu$, and the standard deviation of the background is $\sigma_{sb} = \sqrt{\alpha N}\sigma = \sqrt{\alpha N}\mu$. Therefore, the CNR, which is defined as the ratio between the background-subtracted null intensity and the standard deviation of the background, is given by

$$CNR_N = \frac{\bar{I}_{sn} - \bar{I}_{sb}}{\sigma_{sb}} = -\sqrt{N}\frac{I_t}{\mu} \frac{\exp(-\frac{I_t}{\mu})}{1 - \exp(-\frac{I_t}{\mu})}. \tag{4.19}$$

The PBR, which is defined as the ratio between the negative peak or null point intensity and the mean of the background, is given by

$$PBR_N = \frac{\bar{I}_{sn}}{\bar{I}_{sb}} = -\sqrt{N}\frac{I_t}{\mu} \frac{\exp(-\frac{I_t}{\mu})}{1 - \exp(-\frac{I_t}{\mu})}. \tag{4.20}$$

Discussions on the security of OCIS-based communications

There are two typical scenarios where light can be received by a third party (Fig. 4.12). In free space, scatterers, such as dust, fog, turbid water, or opaque walls, scatter light outside the line-of-sight of the communication parties. In waveguide geometry, leaky modes allow the light to be coupled out of the waveguide. There is also an extreme case where an optical fiber waveguide is cut and a beam splitter is inserted in between. Although this behavior can be easily monitored, we also include it in our security analysis framework.

Without OCIS, light scattering and coupling into a third party will allow the third party to receive the same copy of the information as the primary communication parties. In this case, the security of the information only depends on the use of a digital key to encrypt the information. If the third party hacks the digital key, the information is revealed.

OCIS provides a physical layer of encryption, which can be used on top of digital encryption. Here we analyze the probability of decoding the OCIS encrypted information by coupling and detecting the light during propagation in the aforementioned scenarios. In principle, if the third party (Chuck) can measure the full optical field from the primary communication parties (Alice and Bob), he can decode the information by correlating the two optical fields based on the time-reversal symmetry of light propagation. In practice, measuring the optical field in the middle of the scattering media is extremely challenging in OCIS for several reasons. First, measuring the full field requires a full coverage in free space or cutting the optical fibers, which can be easily monitored as discussed above. Second, OCIS can use multiple spatially incoherent light sources, between which there is no static phase difference, to prevent phase measurement. Therefore, we would like to focus on a more practical case where intensity patterns are measured in the middle.

Here is the process of the intensity pattern measurement. First, Alice sends a single-mode laser pulse through the scattering media to establish a channel map with Bob. Chuck measures a speckle pattern in the middle of the scattering medium, and Bob measures a speckle pattern on the other end of the scattering medium. For simplicity, here we analyze the case where Bob only sends light through one channel for one bit of information transmission. This channel is randomly selected from the channels that meet the intensity requirement and the scattering medium is refreshed when all the channels have been used. Chuck measures the second speckle pattern in the middle when Bob sends one bit back to Alice. In this case, Chuck tries to decode

the information by calculating the sign of the correlation coefficient between the speckle patterns.

Mathematically, we can explicitly calculate the correlation coefficient C of the intensity patterns measured by Chuck and analyze its expected value and the standard deviation. The correlation coefficient C has the form of

$$C = \frac{\frac{1}{M_0}\sum_{r=1}^{M_0}(I_{C,A}(r) - \bar{I}_{C,A})(I_{C,B}(r) - \bar{I}_{C,B})}{\bar{I}_{C,A}\bar{I}_{C,B}}, \tag{4.21}$$

where $I_{C,A}(r)$ and $I_{C,B}(r)$ are the intensity patterns measured by Chuck when Alice and Bob send the light pulses, respectively; $\bar{I}_{C,A}$ and $\bar{I}_{C,B}$ are the mean intensities of these two patterns, respectively; M0 is the total number of spatial modes generated by the scattering medium and is much larger than one; r is the index of the speckle grains. After mathematical derivation based on the complex field relationship ensured by reciprocity, the expected value of correlation coefficient C has the following expression:

$$E(C) \approx \frac{I_t - \bar{I}}{M_0\bar{I}}, \tag{4.22}$$

where I_t is the intensity of the speckle grain that Bob selects as the channel to send one bit back to Alice; $\bar{I}$ is the mean intensity of the speckle grains at Bob's side. For simplicity, here we assume that Alice and Bob use the same amount of power for the laser pulses they send to each other. In this case, the speckle power that Alice observes is also I_t, the same as that of the speckle that Bob selects based on the intensity transmission matrix theory.

While the step by step derivation of the correlation coefficient in Eq. 4.22 is beyond the scope of the work, this equation has an intuitive interpretation. The numerator $I_t - \bar{I}$ indicates the power deviated from the mean power at the mode of interest that Alice observes or Bob selects. If Bob randomly picks a channel to send light back to Alice, the expected value of this deviation should be zero, and the expected correlation between Chuck's patterns is also zeros. Therefore, the expected value of the correlation coefficient describes the energy ratio between the part that is deviated from the mean at the mode of interest and the total energy.

For each bit during transmission, Chuck does the correlation between the two speckle patterns and obtains one correlation coefficient C. Therefore, it is also important to know the deviation of the one-time calculation from the expected value of the correlation coefficient C. The error or the standard deviation of the correlation

coefficient is given by [25]

$$std(C) \approx \sqrt{\frac{1}{M}}, \tag{4.23}$$

where M is the number of modes that Chuck measures out of the M_0 modes carried by the scattering medium. Here we assume that the measurement is well above shot noise limit. Therefore, the SNR of the information that Chuck obtained is given by

$$SNR_C = (\frac{E(C)}{std(C)})^2 = (\frac{I_t - \bar{I}}{\bar{I}})^2 \frac{M}{M_0^2}. \tag{4.24}$$

Here we provide an example calculation of the SNR that Chuck may receive. Let's assume that a scattering medium carries 10^6 modes (M_0) and Chuck measures all the modes in an extreme case ($M = M_0$); the mean of the threshold that Bob chooses is $2\bar{I}$. In this case, the SNR of the correlation coefficient C is $\sim 10^{-6}$, which is very difficult for Chuck to obtain meaning information. In practice, Chuck can only measure a small portion of the modes, resulting in an even lower SNR. The leakage of information can be further mitigated by the combination of digital encryption, such as leakage-resilient cryptography [26].

By providing a physical layer of encryption, OCIS based secure communication can be potentially applied to several scenarios including free-space and fiber-based communication. Importantly, this physical encryption is complementary to and able to work with key based encryption, which includes keys that are generated with optical approaches such as quantum key distribution [27]. Compared to quantum key distribution, OCIS does not have a strict requirement on the number of photons used in communications as long as Alice and Bob can measure sufficient photons. It should be noted that OCIS requires multimode fibers to provide the physical encryption, which is likely to be a limiting factor for immediate use in some existing networks that are based on single mode fibers. In the demonstration, we only show a one-way communication where Bob sends information to Alice. Extending to a two-way communication is straightforward - Alice will need access to multiple speckles like Bob. In our experiment, the data transfer rate is limited by the refreshing rate of the DMD. The data transfer rate can possibly be improved by using an acousto-optic deflector (AOD) to select the intensity channels in the future.

Supplementary Methods - Image transmission through scattering media with OCIS

With the knowledge of intensity mapping between the input plane and target plane, OCIS is able to correct for disordered scattering and allows for direct transmission

of intensity information through scattering media. Here, we demonstrate this ability by directly imaging an object through a scattering medium. From the recording process of optical intensity transpose (Fig. 4b1 or Fig. 4.11a1), we can obtain a map of optical channels between the input plane and target plane during a galvo mirror scan. We can then direct the light from the high-throughput channels to a point on the detector plane during the second galvo scan. In this case, we modulate and send light to the high throughput channels sequentially when the galvo mirror rotates to positions where the channels are connected to the point (Fig. 4.11a1). As such, we obtain a time-averaged optical spot on the detector plane as a PSF of the imaging system.

To form a wide field image through the scattering medium, here we utilize the tilt-tilt correlation or angular memory effect of a thin scattering medium [28, 29]. Within an angular memory effect range, tilting of an input wavefront to a scattering medium causes tilting of the scattered output wavefront, and these two optical wavefronts remain highly correlated. For a thin scattering medium, the correlation maintains within a reasonable tilting angle for wide field imaging. Therefore, the modulation signal that generates the PSF is also a valid solution to cast a neighboring spot on the target plane to a shifted optical spot on the detector plane through the scattering medium (Fig. 4.11a2 and 4.11b2). The method maps to the phase compensation approach that enables wide field imaging through thin scattering medium in optical wavefront shaping [29, 30]. In both cases, we can interpret the system as a piece of compensation optics that corrects for the scattering of the sample and allows us to see through the scattering medium directly (Fig. 4.11c). Intriguingly, no phase information or manipulation is required for OCIS to compensate for the optical scattering here.

To directly correct optical scattering and form an image in free space through a thin scattering medium experimentally, we first calibrated the scattering medium by measuring the response of a point source on the target plane through the scattering medium (Fig. 4.11a1). See Fig. 4.7d for more details on the setup. This step is the same as the recording process in optical intensity transpose. We then used a target consisting of two points near the calibration point with a separation of 20 μm (Fig. 4.11a2). To image the object, the laser source was modulated with the signal measured from the calibration step as the galvo mirror scans. We placed a camera with an exposure time covering the galvo scan duration to directly observe the image of the two spots on the detector plane. As shown in Fig. 4.11d, the image

information directly was transmitted through the scattering medium with OCIS.

The optical setup of realizing imaging through scattering media is shown in Fig. 4.7d. The initial focus for the intensity response measurement as well as the two-point object pattern for imaging was created by using an SLM. During measurement, the SLM displayed a focus on the target plane and the PMT measured the speckle intensity signal as the galvo mirror was scanning. During wide-field imaging, the SLM displayed two foci around the original focus as a target. To directly image this target, we repeated the galvo mirror scanning and modulated the intensity of the laser illumination using the AOM based on the recorded intensity response. The camera was used to directly observe the image of the two foci through the scattering medium.

References

[1] I. M. Vellekoop and A. P. Mosk. Focusing coherent light through opaque strongly scattering media. *Optics Letters*, 32(16):2309, August 2007.

[2] Allard P. Mosk, Ad Lagendijk, Geoffroy Lerosey, and Mathias Fink. Controlling waves in space and time for imaging and focusing in complex media. *Nature Photonics*, 6(5):283–292, May 2012.

[3] Roarke Horstmeyer, Haowen Ruan, and Changhuei Yang. Guidestar-assisted wavefront-shaping methods for focusing light into biological tissue. *Nature Photonics*, 9(9):563–571, August 2015.

[4] Stefan Rotter and Sylvain Gigan. Light fields in complex media: mesoscopic scattering meets wave control. *Reviews of Modern Physics*, 89(1), March 2017.

[5] Moonseok Kim, Wonjun Choi, Youngwoon Choi, Changhyeong Yoon, and Wonshik Choi. Transmission matrix of a scattering medium and its applications in biophotonics. *Optics Express*, 23(10):12648, May 2015.

[6] Hyeonseung Yu, Jongchan Park, KyeoReh Lee, Jonghee Yoon, KyungDuk Kim, Shinwha Lee, and YongKeun Park. Recent advances in wavefront shaping techniques for biomedical applications. *Current Applied Physics*, 15(5):632–641, May 2015.

[7] S. M. Popoff, G. Lerosey, R. Carminati, M. Fink, A. C. Boccara, and S. Gigan. Measuring the transmission matrix in optics: an approach to the study and control of light propagation in disordered media. *Physical Review Letters*, 104(10), March 2010.

[8] Hyeonseung Yu, Timothy R. Hillman, Wonshik Choi, Ji Oon Lee, Michael S. Feld, Ramachandra R. Dasari, and YongKeun Park. Measuring large optical

transmission matrices of disordered media. *Physical Review Letters*, 111(15), October 2013.

[9] Mooseok Jang, Yu Horie, Atsushi Shibukawa, Joshua Brake, Yan Liu, Seyedeh Mahsa Kamali, Amir Arbabi, Haowen Ruan, Andrei Faraon, and Changhuei Yang. Wavefront shaping with disorder-engineered metasurfaces. *Nature Photonics*, 12(2):84–90, January 2018.

[10] Anat Daniel, Liat Liberman, and Yaron Silberberg. Wavefront shaping for glare reduction. *Optica*, 3(10):1104, October 2016.

[11] Jian Xu, Haowen Ruan, Yan Liu, Haojiang Zhou, and Changhuei Yang. Focusing light through scattering media by transmission matrix inversion. *Optics Express*, 25(22):27234, October 2017.

[12] Joseph W. Goodman. *Statistical optics*, volume 1. New York, Wiley-Interscience, 1985.

[13] I. M. Vellekoop, E. G. van Putten, A. Lagendijk, and A. P. Mosk. Demixing light paths inside disordered metamaterials. *Optics Express*, 16(1):67, 2008.

[14] Ivo M. Vellekoop. Feedback-based wavefront shaping. *Optics Express*, 23(9):12189, April 2015.

[15] Yaron Bromberg, Ori Katz, and Yaron Silberberg. Ghost imaging with a single detector. *Physical Review A*, 79(5), May 2009.

[16] Chia-Lung Hsieh, Ye Pu, Rachel Grange, and Demetri Psaltis. Digital phase conjugation of second harmonic radiation emitted by nanoparticles in turbid media. *Optics Express*, 18(12):12283, May 2010.

[17] Meng Cui and Changhuei Yang. Implementation of a digital optical phase conjugation system and its application to study the robustness of turbidity suppression by phase conjugation. *Optics Express*, 18(4):3444, February 2010.

[18] Daifa Wang, Edward Haojiang Zhou, Joshua Brake, Haowen Ruan, Mooseok Jang, and Changhuei Yang. Focusing through dynamic tissue with millisecond digital optical phase conjugation. *Optica*, 2(8):728, August 2015.

[19] Yaron Bromberg, Brandon Redding, Sebastien M. Popoff, Ningbo Zhao, Guifang Li, and Hui Cao. Remote key establishment by random mode mixing in multimode fibers and optical reciprocity. *Optical Engineering*, 58(01):1, January 2019.

[20] Roarke Horstmeyer, Benjamin Judkewitz, Ivo M. Vellekoop, Sid Assawaworrarit, and Changhuei Yang. Physical key-protected one-time pad. *Scientific Reports*, 3(1), December 2013.

[21] Pere Clemente, Vicente Durán, Víctor Torres-Company, Enrique Tajahuerce, and Jesús Lancis. Optical encryption based on computational ghost imaging. *Optics Letters*, 35(14):2391, July 2010.

[22] Charles H. Bennett, François Bessette, Gilles Brassard, Louis Salvail, and John Smolin. Experimental quantum cryptography. *Journal of Cryptology*, 5(1):3–28, January 1992.

[23] Sébastien Popoff, Geoffroy Lerosey, Mathias Fink, Albert Claude Boccara, and Sylvain Gigan. Image transmission through an opaque material. *Nature Communications*, 1(1), September 2010.

[24] Joseph W. Goodman. *Speckle Phenomena in Optics*. Viva Books Private Limited, 2008.

[25] Probable error of a correlation coefficient. *Biometrika*, 6(2-3):302–310, September 1908.

[26] Stefan Dziembowski and Krzysztof Pietrzak. Leakage-resilient cryptography. In *2008 49th Annual IEEE Symposium on Foundations of Computer Science*. IEEE, October 2008.

[27] Charles H. Bennett, François Bessette, Gilles Brassard, Louis Salvail, and John Smolin. Experimental quantum cryptography. *Journal of Cryptology*, 5(1):3–28, January 1992.

[28] Isaac Freund, Michael Rosenbluh, and Shechao Feng. Memory effects in propagation of optical waves through disordered media. *Physical Review Letters*, 61(20):2328–2331, November 1988.

[29] Ori Katz, Eran Small, and Yaron Silberberg. Looking around corners and through thin turbid layers in real time with scattered incoherent light. *Nature Photonics*, 6(8):549–553, July 2012.

[30] Ori Katz, Pierre Heidmann, Mathias Fink, and Sylvain Gigan. Non-invasive single-shot imaging through scattering layers and around corners via speckle correlations. *Nature Photonics*, 8(10):784–790, August 2014.

Chapter 5

INTERFEROMETRIC SPECKLE VISIBILITY SPECTROSCOPY (ISVS) FOR HUMAN CEREBRAL BLOOD FLOW MONITORING

This chapter contains unpublished content from a submitted manuscript.

Infrared light scattering methods have been developed and employed to non-invasively monitor human cerebral blood flow. However, the number of reflected photons that interact with the brain is low when detecting blood flow in deep tissue. To tackle this photon-starved problem, we present and demonstrate the idea of interferometric speckle visibility spectroscopy (ISVS). In ISVS, an interferometric detection scheme is used to boost the weak signal light. The blood flow dynamics are inferred from the speckle statistics of a single frame speckle pattern. We experimentally demonstrated the improvement of measurement fidelity by introducing interferometric detection when the signal photon number is insufficient. Our system is able to achieve a frame rate of 100 Hz even when the average signal photoelectron number is less than 1 count/pixel. This photoelectron rate is $\sim$100-fold less than that in common DCS implementations. By using $\sim 2\times10^5$ pixels together with interferometric detection, the ISVS sytem successfully monitors the human brain pulsatile blood flow, as well as the blood flow change when a human subject is doing a breath holding task. This work provides a new technique for cerebral blood flow detection.

5.1 Introduction

Over the last few decades, a variety of non-invasive optical schemes have been developed to study the cerebral blood flow (CBF) dynamics in human brains [1, 2, 3, 4], including near-infrared spectroscopy (NIRS) [1], diffuse correlation spectroscopy (DCS) [2, 3], and diffuse optical tomography (DOT) [4]. The 650–950 nm optical window has relatively low optical absorption and therefore enables light to penetrate through the skin, scalp, and skull and interact with the brain. Returning photons carry information about the CBF and can be used to infer the brain activity via neurovascular coupling [5, 6]. In short, neurovascular coupling describes the connection between brain activity and CBF, since adequate CBF ensures sufficient oxygen is delivered to the tissue [7].

In recent years, there has been a renewed effort to use DCS for such measurements. DCS uses coherent red or near-infrared lasers as light sources and high-bandwidth single-photon counting modules (SPCM) as detectors. Compared to NIRS and DOT that measure reflected light intensity, DCS analyzes the dynamic scattering by monitoring intensity fluctuations. Therefore, DCS measures the flow dynamics rather than the hemoglobin concentration. Compared to the existing functional brain activity detection approaches, such as functional magnetic resonance imaging (fMRI) and electroencephalography (EEG), DCS offers an additional capability with some advantages. In terms of refresh rate, recent work from Wang *et al.* [8] showed a refresh rate of tens of Hz, which is able to well sample the pulsatile effect in CBF. Since the sampling bandwidth of fast fMRI is in the order of 1 Hz [9] and common human cardiac signals (heartbeat) usually have a period of 1-3 Hz, the cardiac signals are not well sampled, which significantly contributes to the noise in fMRI [10]. Typical DCS systems are able to provide a spatial resolution of ~ 1 cm [11, 12]. Non-invasive EEG, the gold standard technique for monitoring brain activity in terms of speed, provides signals from a mixture of multiple underlying brain sources. This results in low spatial resolution of 5–9 cm [13]. Therefore, DCS lies in the niche between fMRI and EEG, where fMRI has high spatial resolution (~ 2 mm) [12] but relatively low temporal resolution (~ 1 Hz) and EEG has high temporal resolution (> 1 kHz) [14], but low spatial resolution (5–9 cm).

The performance of DCS is ultimately constrained by the total collected photon budget required for a reasonable signal-to-noise ratio (SNR). Since DCS exploits only a few speckle grains from the scattered light, in order to get a sufficient number of signal photons for a relatively accurate measure on the blood flow dynamics, the required measurement time of the detector for one data point (one measurement of CBF) is typically no less than tens of milliseconds. There is therefore a tradeoff between the measurement time and the sensitivity of the system: a high SNR measurement requires relatively long measurement time, which results in a relatively low sampling rate. This tradeoff is fundamentally caused by the limitation of photon budgets and can be mitigated by using multi-channel DCS, which in turn scales up the costs of the system [15, 8]. Furthermore, the multi-channel DCS also scales up the requirement of data throughputs, which also brings technical issues in practical implementations.

To tackle the limitation of the shortage of signal photons, people use a camera sensor with thousands to millions pixels as the detector in place of the SPCM.

By using a camera sensor, the system can collect more photons with the same measurement time compared to DCS, or collect the same number of photons with a shorter measurement time. Because the number of pixels is large while the data throughput is limited, the temporal sampling speed is typically not sufficient to well sample the temporal intensity fluctuation. Even though, the temporal dynamics of blood flows can be inferred from the speckle statistics of the captured frame. This method is termed speckle visibility spectroscopy (SVS), or speckle contrast spectroscopy [16, 17, 18, 19, 20]. In the SVS-based approach, a whole speckle pattern containing many speckle grains is captured using a detector array (e.g., a CCD camera), and the statistics of the blurred speckle pattern is used to calculate the speckle decorrelation time. With a given camera integration time that is longer than the speckle decorrelation time, different speckle decorrelation times result in speckle frames with different extent of blurring. Since a speckle pattern recorded by a detector array can contain thousands to millions of speckle grains, the photon budget limitation is mitigated. In this case, a single decorrelation time measurement does not require tens of millisecond as compared to DCS, therefore resulting in a higher refresh rate.

While SVS relaxes the requirements for temporal fidelity, it suffers from camera noise as commercial camera sensors are usually noisier than SPCMs when the signal light intensity is low. When detecting "deep photons" — those interacting with tissues at larger depths (>1 cm) — the amount of reflected photons reaching the detector array can be less than 1 photon/pixel within the camera exposure time. In these cases, the camera noise would overwhelm the detected deep photons. The direct way to overcome this problem would be to increase the camera exposure time. Similar to the aforementioned tradeoff between SNR and measurement time, the increase of exposure time will result in a decrease in the refresh rate.

Here we propose and demonstrate the idea of interferometric SVS, or ISVS, which circumvents the camera noise problem and is able to measure the blood flow dynamics even when the number of available signal photons is limited (below 1 photoelectron per pixel). Interferometric detection is able to overcome camera noise by boosting the weak signal term in the heterodyne cross-term, and as such, the ISVS system is able to achieve a reasonable SNR even when the mean pixel value number from the signal light is smaller than 1. A novel interference speckle spatial statistics analysis is derived to quantify the speckle decorrelation time. By using ISVS, we demonstrate high speed (100 Hz) non-invasive *in-vivo* cerebral blood flow

monitoring on the human forehead, under the condition where the number of signal photoelectrons per pixel is ~ 0.95. In this case, the camera sensor noise is ~1.2 photoelectrons per pixel. The direct measurement will yield an SNR of ~0.61 for each pixel due to the photoelectron shot noise and the detector noise. By using ISVS, the detector noise effect can be mitigated and the single pixel measurement SNR is dominant by shot noise. Therefore, in the interferometric detection regime, the single pixel SNR should be ~0.95 due to shot noise, and $\sim 2\times10^5$ camera pixels are used to scale up the overall SNR by $\sqrt{2\times10^5} \approx 450$ times to 430. We also design a breath holding task for a human subject and implement ISVS to monitor the CBF, showing that the relative CBF (rCBF) changes in accordance to brain stimulation caused by the task can be revealed by ISVS.

5.2 Results

Principle

The ISVS principle is based on an interferometer, where the weak diffused light containing the information is boosted by a reference beam and recorded by the camera (See Fig. 5.1(a)). The image sequence recorded on the camera can be reconstructed to provide a sequence that contains blood flow information, where each camera frame corresponds to one data point in the reconstructed sequence. Assuming the diffused light has a limited spatial bandwidth, the complex field of the diffused light is obtained via an off-axis holography configuration [21], by directly reconstructing the measured output intensity of the interferometer. In this configuration, the total instantaneous interference pattern I_t at the position $\mathbf{r}=(x, y)$ in the observation plane is

$$\begin{aligned} I_{\mathrm{t}}(\mathbf{r}) &= |E_{\mathrm{R}}|^2 + |E_{\mathrm{S}}(\mathbf{r})|^2 + 2|E_{\mathrm{R}}||E_{\mathrm{S}}(\mathbf{r})|\cos\Big(k_0 x\sin\theta + \phi_{\mathrm{S}}(\mathbf{r})\Big) \\ &= I_{\mathrm{R}} + I_{\mathrm{S}}(\mathbf{r}) + 2\sqrt{I_{\mathrm{R}} I_{\mathrm{S}}(\mathbf{r})}\cos\Big(k_0 x\sin\theta + \phi_{\mathrm{S}}(\mathbf{r})\Big), \end{aligned} \tag{5.1}$$

where E_{R} is the complex field of the plane wave reference beam, $E_{\mathrm{S}}(\mathbf{r})$ is the complex field of the diffused light, $\phi_{\mathrm{S}}(\mathbf{r})$ is the phase difference between the reference beam and the diffused light field, k_0 is the wave-vector in free space, and θ is the tilt angle of the oblique reference beam. Thanks to the off-axis holography, the Fourier transform of $I_{\mathrm{t}}(\mathbf{r})$ in Eq. (5.1) provides three separate lobes (see Fig. 5.4A), where the central lobe is the Fourier transform of the DC terms (first two terms in Eq. (5.1)) and the two side lobes are the Fourier transform of the interference term (third term in Eq.(5.1)). The reconstructed signal $I_{\mathrm{rec}}(\mathbf{r})$ is with $I_{\mathrm{R}}=|E_{\mathrm{R}}|^2$ and $I_{\mathrm{S}}(\mathbf{r})=|E_{\mathrm{R}}(\mathbf{r})|^2$. Here $I_{\mathrm{rec}}(\mathbf{r})$ contains the information of the diffused light. It is worth noting that

the instantaneous analysis is valid for a given time (e.g. $t=0$), whereas the detector has a non-zero integration time to record the intensities. Nevertheless, this analysis is indicative of the SNR advantage through interferometry: for most speckle grains, the intensity of a speckle grain is smaller than the reference beam intensity, resulting in $I_{\mathrm{rec}}(\mathbf{r}) > I_{\mathrm{S}}(\mathbf{r})$. Thus the signal experiences a significant boost, which can salvage extremely weak signals from being buried under the detector noise. Note that this basic argument is not accurate for the intensities measured in the experiment, since the detector measures the intensities for a given integration time, rather than giving an instantaneous value. A careful analysis below shows the exposure time T reduces the energy of the heterodyne terms by a less-than-unity 'visibility factor'.

We now move forward to quantitatively demonstrate how ISVS is able to distinguish between decorrelation events of different timescales. The analysis is dependent on interference speckle spatial statistics, which is exploited for the first time in CBF measurements. In Fig. 5.1, the interference pattern recorded by the camera is

$$\begin{aligned} I(\mathbf{r}) \quad &= \int_0^T \Big[|E_{\mathrm{R}}|^2 + |E_{\mathrm{S}}(\mathbf{r},t)|^2 + 2|E_{\mathrm{R}}||E_{\mathrm{S}}(\mathbf{r},t)| \\ &\quad \times \cos\Big(k_0 x \sin\theta + \phi_{\mathrm{S}}(\mathbf{r},t)\Big)\Big] dt, \end{aligned} \tag{5.2}$$

where $t = 0$ defines the beginning of the exposure and T is the exposure time. Since the third interference term in the integral has a different location on Fourier space, one can filter it out to get the complex field information. Let us define the interference signal as $H(\mathbf{r}) = \frac{1}{T}\int_0^T 2|E_{\mathrm{R}}||E_{\mathrm{S}}(\mathbf{r},t)|\cos\phi_{\mathrm{S}}(\mathbf{r},t)\, dt$. It can be rewritten as $H(\mathbf{r}) = \frac{1}{T}\int_0^T |E_{\mathrm{R}}||E_{\mathrm{S}}(\mathbf{r},t)|e^{i\phi_{\mathrm{S}}(\mathbf{r},t)}dt + \frac{1}{T}\int_0^T |E_{\mathrm{R}}||E_{\mathrm{S}}(\mathbf{r},t)|e^{-i\phi_{\mathrm{S}}(\mathbf{r},t)}dt$. We can then pick the first one of the phase conjugated pairs and define the ISVS signal $S(\mathbf{r})$ as

$$S(\mathbf{r}) = \frac{1}{T}\int_0^T |E_{\mathrm{R}}||E_{\mathrm{S}}(\mathbf{r},t)| \exp\Big(i\phi_{\mathrm{S}}(\mathbf{r},t)\Big)\, dt. \tag{5.3}$$

The second moment of $S(\mathbf{r})$ will contain the field decorrelation function $g_1(t) = \langle E_{\mathrm{S}}(\mathbf{r},t_0)\, E_{\mathrm{S}}^*(\mathbf{r},t_0{+}t)\rangle_{t_0} / \langle |E_{\mathrm{S}}(\mathbf{r},t_0)|^2\rangle_{t_0}$ after the mathematical derivation shown in Eq. (5.4) below (See more details in Section 5.4 and Ref. [22]):

$$\begin{aligned} &\langle |S(\mathbf{r})|^2 \rangle \\ &= \frac{I_{\mathrm{R}}}{T^2}\Big\langle \int_0^T \int_0^T dt_1 dt_2\; E_{\mathrm{S}}(\mathbf{r},t_1) \exp\Big(i\phi_{\mathrm{S}}(\mathbf{r},t_1)\Big) E_{\mathrm{S}}(\mathbf{r},t_2) \exp\Big(-i\phi_{\mathrm{S}}(\mathbf{r},t_2)\Big)\Big\rangle \\ &= \frac{I_{\mathrm{R}}\bar{I}_{\mathrm{S}}}{T}\int_0^T 2(1-\frac{t}{T}) g_1(t)\, dt, \end{aligned} \tag{5.4}$$

where $\langle\bullet\rangle_{t_0}$ denotes the expected value over t_0, $\langle\bullet\rangle$ denotes the expected value over space, I_{R} is the intensity of the reference beam, and $\bar{I}_{\mathrm{S}}$ is the mean intensity of the

signal beam. Both of I_R and $\bar{I_S}$ can be calibrated before the experiment. We then define the visibility factor

$$F = \frac{\langle |S(\mathbf{r})|^2 \rangle}{I_R \bar{I_S}} = \frac{1}{T} \int_0^T 2(1 - \frac{t}{T}) g_1(t)\, dt \tag{5.5}$$

which ranges from 0 to 1 for different $g_1(t)$.

As we can see from Eq. (5.5), the visibility factor F is a function of $g_1(t)$ and the camera exposure time T. If the sample is static (i.e., $g_1(t) = 1$ for $0 < t < T$), $F = 1$, indicating that the interference fringes have high contrast. If the complex field of the diffuse light decorrelates very quickly compared to T, (i.e., $g_1(t) = 1$ for $0 < t < \tau$ and $g_1(t) = 0$ for $\tau < t < T$ where $\tau \ll T$), $F = \frac{2\tau}{T}$, indicating that the interference fringes have low contrast. This matches with the intuition that multiple decorrelation events happening within the camera exposure time blur out the interference fringes and yield a low fringe visibility.

Figure 5.1(b) intuitively shows the relation between the visibility factor and the decorrelation time scale. Let us consider two cases: a static optical field (top row in Fig. 5.1(b) and a decorrelating optical field (bottom row in Fig. 5.1(b)). If the optical field is static, the amplitude and phase of one speckle grain is fixed within the camera exposure time T and thus the interference fringes have high visibility. If the optical field is decorrelating within the camera exposure time, the pattern recorded on the camera will be the summation of different interference patterns with difference amplitudes and phases. The summation of the patterns from uncorrelated sample field will cause a low fringe visibility. As the decorrelation time shrinks relative to the camera exposure time T, the number of decorrelating events within T grows, therefore leading to lower fringe visibility.

System characterization and measurement fidelity improvements

To verify and characterize the performance of the system, we used two ground glass diffusers (Thorlabs, DG20 Series) as the samples. The schematic is shown in Fig. 5.2(a) (more details in Fig. 5.5A). The first one had controlled rotating speeds and the other one is static. A laser beam illuminated the rotating diffuser and a range of rotation speeds were applied. The scattered light from the first rotating diffuser illuminated the second static diffuser and was collected by the optical system. The static diffuser was used to eliminate the speckle pattern "smearing" effect that is present when using a single rotating diffuser. The decorrelation times were computed by measuring the time traces of the intensity fluctuations using a single

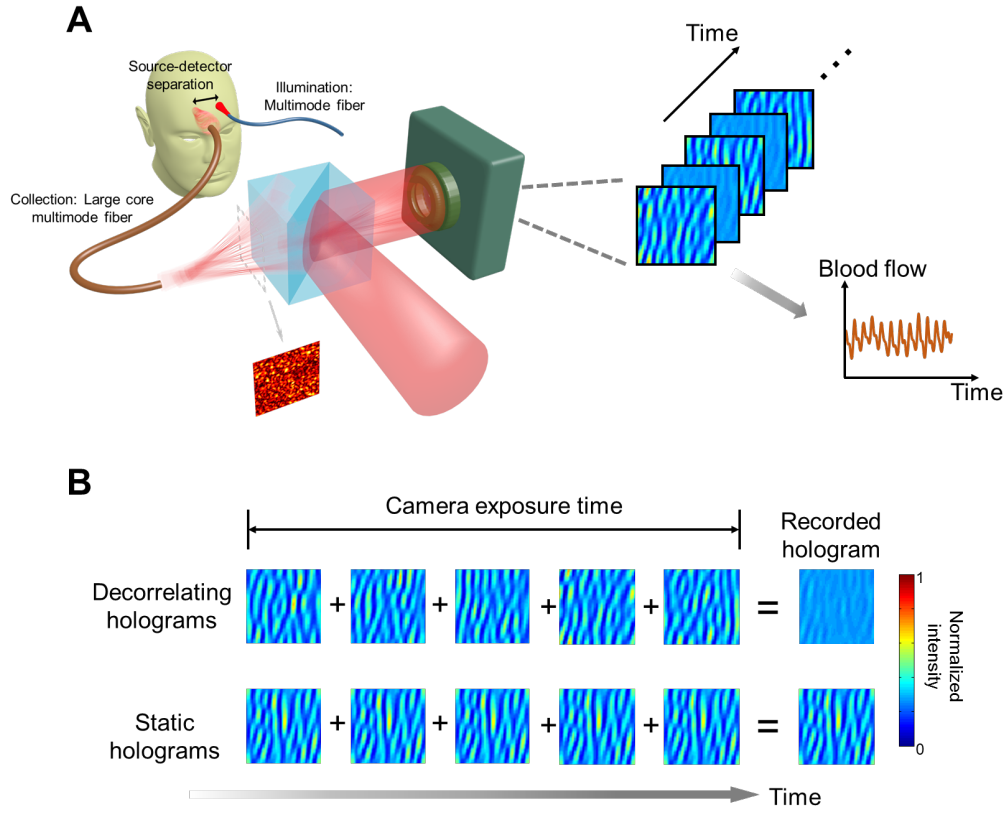

Figure 5.1: Principle of ISVS. (a) Schematic of ISVS setup. A beam illuminates the subject and the diffused light collected by the optical system interferes with a reference beam on a camera. The sequence of the interference patterns is used to reconstruct the signal trace that contains blood flow information. (b) Difference between decorrelating and static diffused optical field recorded in a single camera frame. When the diffused optical field is decorrelating, the camera integration sums the independent holograms and results in a low fringe visibility hologram; when the diffused optical field is static, the same hologram lasts during the whole camera integration time and results in a high fringe visibility hologram.

photon counting module (SPCM) in the optical setup. Then, by mapping rotation speed to the measured decorrelation time, we were able to simulate a dynamic sample with configurable decorrelation times.

First, we verified the mathematical model of the ISVS visibility factor by experimental results. The blue curve in Fig. 5.2(b) depicts the measured ISVS visibility factors under different camera exposure times (T) to decorrelation time (τ) ratios, T/τ, where the decorrelation time τ of the scattering light was measured by analyzing the autocorrelation of the time traces captured by the SPCM in parallel to the ISVS measurement. The error bars on vertical axis were calculated from 10 ISVS measurements, and the error bars on horizontal axis were calculated from 10 DCS measurements. The red curve is the theoretical model calculation (See Eq. 5.10), showing good correspondence with the experimental results.

Using the theoretical model, we then mapped the measured visibility factors to decorrelation times (Fig. 5.2(c) vertical axis) and compared them to the DCS measured decorrelation times (Fig. 5.2(c) horizontal axis). The black dotted curve is the line with the slope equal to 1. The agreement between the ISVS and DCS measured speckle decorrelation times shows the ability of the system to quantitatively measure decorrelation time.

Finally, we showed that the signal boost from the interferometric detection scheme resulted in a measurement with higher fidelity compared to direct detection, when the number of signal photons from the sample was low. In this experiment, we performed direct SVS measurements and used the model from Ref. [17] to calculate the scattered light decorrelation time. As shown in (Fig. 5.2(d), when the number of photon-electrons excited by the signal beam was large (> 5 e^-/pixel), both SVS and ISVS provided results close to the one in the DCS measurement, which served as the ground truth. As the signal beam became weaker, SVS measured decorrelation times deviated from the ground truth and got larger. In the low photon budget regime (e.g., < 1 e^-/pixel) where mean intensity on the camera was low, the detector noise dominated the spatial speckle fluctuation, resulting in a high contrast, i.e., the ratio between the standard deviation and the mean value of the frame is high. For SVS, this camera-noise caused high contrast pattern may have a similar contrast as a frame with high contrast speckles. In this case, the model will inaccurately provide a long decorrelation time that is close to a static speckle pattern. In comparison, the interference term of ISVS is not significantly impacted by the camera noise and ISVS should provide an accurate measurement even when the detected signal photon

count is low.

System operation on rats

We implemented an ISVS system to monitor blood flow in rats. The monitoring was performed in the dorsal skin and brain in a reflection-mode configuration. A nude rat was first anesthetized and then its dorsal skin was shaved and mounted to a clip device. A collimated laser beam illuminated the skin and the light diffused by the skin was detected by the ISVS system. The pulsatile effect of the blood flow from the dorsal skin flap measured by the ISVS system is presented in Fig. 5.6A. Additionally, another nude rat was anesthetized and a portion of its scalp removed. A collimated laser beam illuminated the skull and the light diffused from the skull and brain was detected by the ISVS system. The pulsatile CBF results from ISVS measurement are shown in Fig. 5.6B. In the rat brain experiment, the bregma area was imaged by the system (Fig. 5.6C) and the central part of the imaging area was ~ 1 cm from the laser illumination spot. In both dorsal skin and brain blood flow measurements, a customized pulse monitor was synchronized with the optical system and monitored the blood flow in the tail, confirming that the detected pulsatile ISVS signals indeed originate from the pulsatile nature of the heart beating. A schematic of the experimental setup is shown in Fig. 5.5B and details of the anesthesia and surgery are in Section 5.4. All of the procedures and the dosage of chemicals followed the protocols of the Institutional Animal Care and Use Committee at California Institute of Technology. Animal husbandry and all experimental procedures involving animal subjects were approved by the Institutional Animal Care and Use Committee (IACUC) and by the Office of Laboratory Animal Resources at the California Institute of Technology under IACUC protocol 1770-18.

Human experiment design and operation

To demonstrate the performance of ISVS for *in vivo* measurements of CBF dynamics, we implemented an ISVS system on human subjects, as depicted in Fig. 5.3(a). The schematic of a more detailed optical setup can be found in Section5.4 and Fig. 5.5C. A beam splitter was added to split the light onto a single-photon-counting-module (SPCM) as a reference for photon count rates, as well as a DCS measurement. A healthy adult human subject sat on a medical chair with his head placed inside a head immobilizer. Non-contact source and detector fibers were mounted above the subject's forehead over the prefrontal cortex area. To have a sufficient number of illumination photons for this measurement, the laser beam

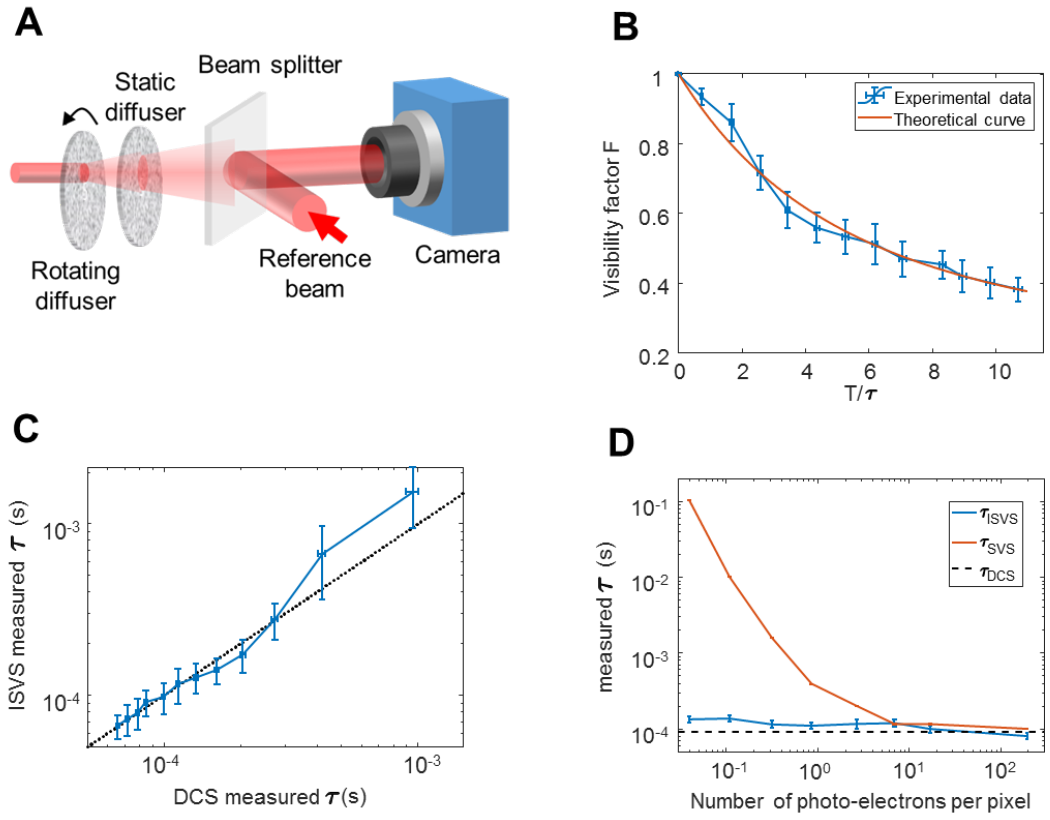

Figure 5.2: Characterization of ISVS by using rotating diffusers. (a) Schematic of the characterization experiment using two rotating diffusers. (b) Experimentally measured visibility factor F in different T/τ (blue curve), and the theoretical model curve (red curve). The vertical error bars are calculated from 30 ISVS measurements, and the horizontal error bars are calculated from 10 DCS measurements. (c) The comparison between the ISVS measured τ and DCS measured τ. The blue curve is the experimental result, and the black dotted line is the line of unity slope. (d) Comparing measured τ from interferometric (ISVS, blue curve) and direct (SVS, red curve) detection in different light intensities. The horizontal axis shows the mean number of photo-electrons on each pixel of the camera. The error bars are calculated from 30 ISVS and SVS measurements. The decorrelation time measured by DCS (black dashed line) serves as the ground truth.

from the 671-nm source was coupled to a multimode fiber (Thorlabs M31L02, ~ 3000 modes). The collimated 56 mW laser beam with a 6-mm spot size resulted in a $< 2\text{mW/mm}^2$ irradiance for skin exposure – within the limit stipulated by American National Standard Institute (ANSI). The diffused light at various source-detector (S-D) separations (S-D = 1.5 cm and 0.75 cm) was then collected via a large core multimode fiber (Thorlabs M107L02, core diameter 1.5 mm) containing ~ 6 million modes. The output of this fiber was channeled through the sample arm of the interferometer. About 2×10^5 camera pixels were used to capture the photons. A human protocol comprising of all detailed experimental procedures were reviewed and approved by the Caltech Institutional Review Board (IRB) under IRB protocol 19-0941, informed consent was obtained in all cases, and safety precautions were implemented to avoid accidental eye exposure.

We first demonstrated that the ISVS system was able to monitor the blood flow in humans when the reflected light signal was low. When the S-D separation was 1.5 cm, the photon count rate read by the SPCM was ~ 1500 counts/second, while the dark count rate of the SPCM was ~ 180 counts/second. This photon rate is ~ 100 fold less than the light budget in conventional DCS experiments [8]. Due to the experimental resources, the laser wavelength is 671 nm, at which biological tissue has a higher absorption coefficient than wavelength 785 nm in common DCS settings. The intensity decorrelation curve $g_2(t)$ is shown in Fig. 5.3(b) after a DCS measurement by the SPCM with a measurement time of 50 s. To obtain the pulsatile signal from the DCS measurement, the SPCM trace is divided into sub traces with the time duration of 10 ms for each sub trace. The blood flow index (BFI) is calculated from each sub trace, based on the tissue scattering parameters used in Ref. [23]. As shown in Fig. 5.3(c), there is no obvious pulsatile signal retrieved from the DCS measurement. Therefore, under this experimental condition, the photon count rate was not sufficient for DCS to monitor the pulsatile signal with a reasonable SNR. The ISVS system with a camera exposure time of 2 ms and an FPS of 100 Hz yielded a pulsatile signal trace, shown by the blue color line in Fig. 5.3(d). The filtered signal trace is the red color line in Fig. 5.3(d). The measured ISVS visibility factor was used to calculate the decorrelation time, and the decorrelation time was used to calculate the BFI. The raw and filtered BFI traces are presented in blue and red curves in Fig. 5.3(e), respectively. The Fourier transform of the raw BFI trace is shown in Fig. 5.3(f), and the heart-beat frequency ~ 1.1 Hz and its harmonics are highlighted. In this experimental configuration, the average photoelectron number of the signal beam on each camera pixel was ~ 0.95, where

the detector noise was ~ 1.2 photoelectrons. In this case, the SNR for each pixel was $\sim 0.95/\sqrt{0.95 + 1.2^2} = 0.61$ with a direct measurement. With a shot noise dominant interferometric measurement, the single pixel SNR can achieve 0.95. By using $\sim 2 \times 10^5$ camera pixels, the overall SNR can be scaled up by $\sqrt{2 \times 10^5} \approx 450$ times to 430. It is worth mentioning that, due to the dynamic scattering interaction between the light and the blood flow, the contrast of the speckle pattern was much lower than unity, predicted by the static speckle statistics. This in fact makes direct detection even harder to retrieve the contrast of the pattern and the information of the blood flow.

In order to demonstrate the capability of ISVS for human brain activity detection, we established a straightforward brain stimulation experiment (breath-holding task) for a healthy human subject. The experiment was based upon the fact that the stoppage of the subject's breathing increases the CBF due to vasomotor reactivity from rising pCO_2 [24, 25]. CO_2 pressure will raise during breath holding [25] due to metabolism, and the rising CO_2 pressure can cause the increase of blood flow [24]. In the experiment, the subject first breathed normally for ~ 2 minutes, then did an exhalation breath holding for ~ 15 s, and finally started to recover by having normal breathing again.

The S-D separations in the breath holding task were set to be 1.5 cm and 0.75 cm. Since the ~ 1 Hz pulsatile blood flow change naturally presented in the measurement, we set the sampling rate as 12 Hz. At this sampling rate the pulsatile signal was present, where data processing could filter it. The system recorded the ~ 10 s before the breath holding, the entire ~ 15 s of breath holding, and the ~ 16 s after the breath holding. We performed ISVS measurements in 3 cases: (i) an S-D separation of $d_1 = 1.5$ cm while the subject went through a breath-holding task, (ii) an S-D separation of $d_1 = 0.75$ cm while the subject went through a breath-holding task, and (iii) an S-D separation of $d_2 = 1.5$ cm while the subject breathed normally. The representative recorded traces for case (i), (ii), and (iii) are shown in Fig. 5.3(g) and Fig. 5.3(h), respectively. For each case, five repetitive experiments were conducted to avoid single experiment outlier.

To see the rCBF change due to the breath holding task, the mean values and standard deviations of rCBF during 2–4 s (Phase 1), 10–12 s (Phase 2, first several seconds of breath holding), 22–24 s (Phase 3, last several seconds of breath holding), and 37–39 s (Phase 4) were calculated and plotted, as shown in Fig. 5.3(i). The increase of rCBF values in Phase 3 at the S-D separation of 15 mm (case (i)) is clearly shown

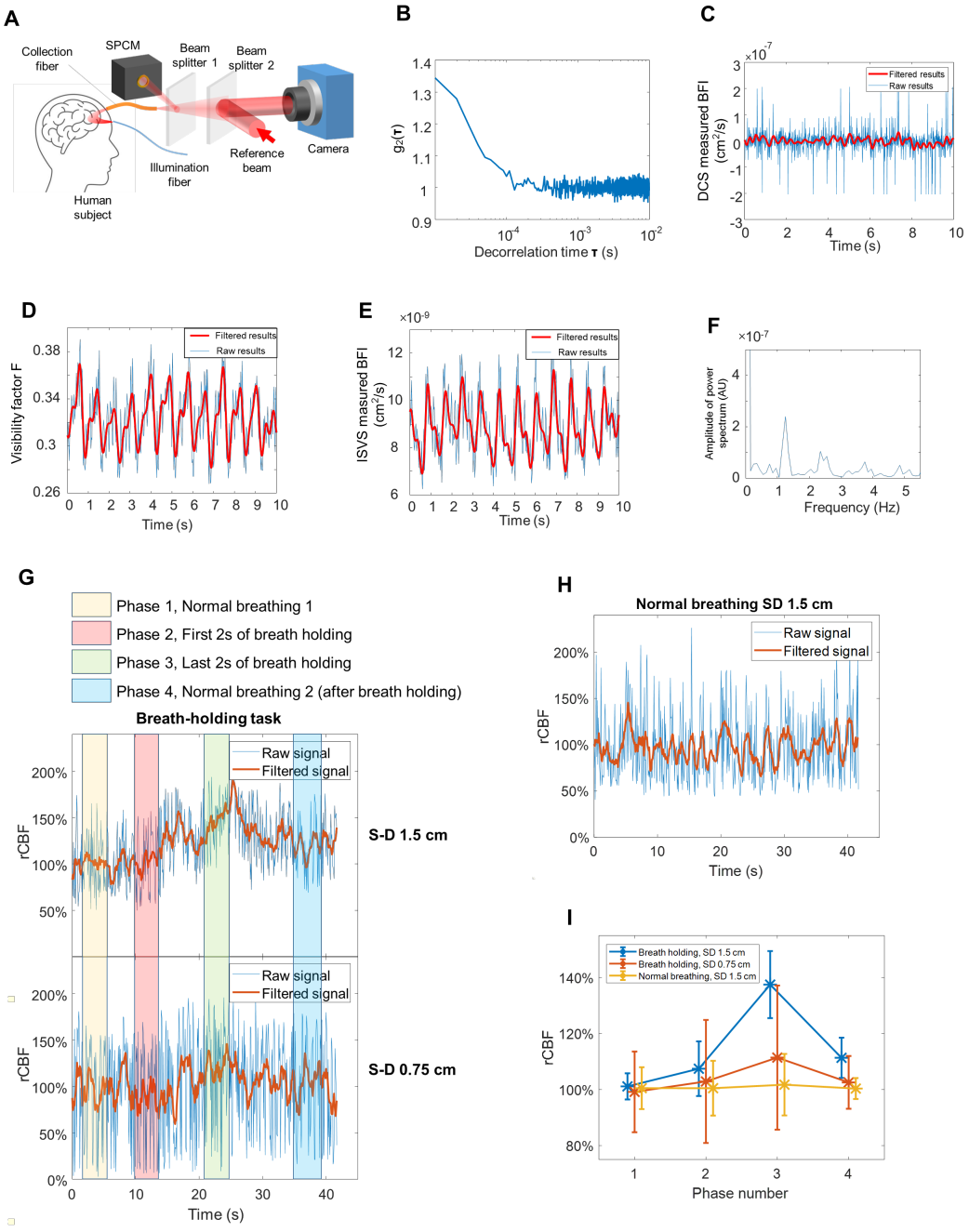

Figure 5.3: ISVS experimental results on a human subject. (a) Schematic of the human experiment. The illumination came from a multimode fiber, and the diffused light was collected by a large core multimode fiber. The output light of the large core multimode fiber was directed into the ISVS setup, where the diffused light and the reference beam were combined by a beam splitter and recorded by the camera.

Figure 5.3: (Continued) (b) The intensity correlation function $g_2(t)$ from a SPCM recording trace with time duration of 50 s. The decorrelation time is ~50 μs. (c) The BFI trace calculated from DCS. The entire intensity fluctuation trace is divided into sub traces, then the BFI is calculated from each sub trace. The BFI sampling rate is 100 Hz. (d) The ISVS visibility factor measured at 100 Hz on the forehead of the human subject. The blue curve shows the original data points, and the red curve is a low-pass filtered version of the blue curve. (e) Blood flow index calculated from the visibility factor. The blue curve was calculated from the original data points, and the red curve was low-pass filtered from the blue curve. (f) A Fourier transform of the blue curve in (e) shows the heart beat frequency at ~1.1 Hz and its harmonics. (g) ISVS measured rCBF traces when the human subject was doing the breath holding task. The subject exhaled and started holding their breath at ~10 s and kept it until around ~15 s, after which the normal breathing was resumed. (h) ISVS measured rCBF trace when the human subject breathed normally. (i) Statistical analysis of rCBF change at different phases. Each data point and the error bar were calculated from 5 measurement curves from one human subject.

by the blue line in Fig. 5.3(i). In this case (S-D separation of 1.5 cm), some of the light interacted with the cerebral blood flow, as the previous research from Selb *et al.* [26] showed that the blood flow change could be seen at an S-D separation larger than 1 cm. The increase of rCBF values in Phase 3 at the S-D separation of 7.5 mm (case (iii)) was not as clear as that in case (i), as shown by the red line in Fig. 5.3(i). In this case (S-D separation of 0.75 cm), most of the light interacted with the forehead skin rather than the brain, hence the breath holding task did not have the same significant impacts on the signal. The normal breathing measurements at the S-D separation of 1.5 cm (case (iii)) as a reference did not have significant change of rCBF, as shown by the yellow line Fig. 5.3(i).

5.3 Discussion

Here we demonstrated the concept of ISVS, characterized the performance of ISVS, and implemented it in human cerebral blood monitoring. The interferometric detection and camera parallel measurement of multiple speckles allowed us to sample the weak signal light with high fidelity and a high frame rate. By using the sensitive ISVS system, we monitored the pulsatile blood flow in brain as well as the cerebral blood flow change during a breath holding task. The photon rate in our demonstration was ~100 fold less than the photon rate in conventional DCS measurements.

From a more general perspective, diffusing correlation spectroscopy-based methods can in general be categorized as time domain (DCS and interferometric DCS [15])

Table 5.1: Overview of the mainstream non-invasive CBF imaging techniques. The last column is added to place ISVS in perspective.

	O^{15}PET	SPECT	XeCT	CT-P	DCS-MRI	ASL-MRI	Doppler Ultrasound	DCS	ISVS
Bedside	No	Sometimes	No	No	No	No	Yes	Yes	Yes
Contrast Agent	Yes	Yes	Yes	Yes	Yes	No	No	No	No
Radiation	Yes	Yes	Yes	Yes	No	No	No	No	No
Acq. Time	5–9 min	10–15 min	10 min	40 sec	1 min	5–10 min	10–20 min	0.5–6 sec	1–10 ms
Parameters	CBF	CBF	CBF	MTT	MTT	CBF	BFV	CBF	CBF
Quantitative	Yes	Sometimes	Yes	Yes	N/A	Yes[1]	N/A	Relative[2]	Relative
Spatial Resolution	~5 mm	~5 mm	~5 mm	~1.5 mm	~2 mm	~5 mm	N/A	~10 mm	~10 mm
Intrascan time	10 min	10 min	20 min	10 min	25 min	0 min	0 min	0 min	0 min
Instrument Cost	High	High	Moderate	Moderate	High	High	Low	Low	Low

or spatial domain (SVS and ISVS) methods. Both of them use corresponding mathematical models to describe the light-tissue interaction and speckle statistics to infer the temporal dynamics of signals of interest, such as cerebral blood flow. Time domain methods (e.g., DCS, interferometric DCS) directly sample one or several dynamical speckles temporally using high speed detectors, while spatial domain methods, including ISVS, sample speckles spatially using detector arrays. Since the SNR of the decorrelation time measurement is tied to the number of signal photons, getting a higher SNR usually requires more signal photons. The more signal photons in time domain methods inevitably lead to longer measurement time, while in spatial domain methods that leads to more camera pixels. Therefore, in spatial domain methods, scaling up of the number of camera pixels will scale up the SNR of signal data points without increasing the measurement time, given high enough data throughputs.

Another property of ISVS is that it does analysis on complex fields directly. As shown in Eq. (5.3), the off-axis holography scheme allows us to reconstruct the complex field and incorporate the field correlation function $g_1(t)$ directly into the visibility factor. In conventional methods such as time domain DCS or spatial domain SVS, it is usually necessary to measure the intensity and use the Siegert relation [27] to get the information of the field correlation function $g_1(t)$. There are several conditions required for the Siegert relation to be valid, such as the Gaussian statistics and ergodicity requirements for the speckle field [28]. When light interacts with static parts in tissue and diffuses to the detection plane, such as surface reflection or shallow skin diffusion, there will be a static speckle field adding on the dynamic speckle field. This static speckle field breaks the Gaussian statistics and ergodicity requirements, and the Siegert relation in this case does not hold. ISVS circumvents the Siegert relation and is able to directly retrieve the information of the field correlation function $g_1(t)$.

The goal for future development of ISVS is to improve the stability of the light collection part in the system. As we use a large core multimode fiber to collect the signal light, it is highly sensitive to environmental perturbation, such as vibration. The perturbation can cause significant changes in mode mixing in the fiber and results in a decorrelating speckle pattern at the output of the fiber even if the input optical field of the fiber is static. If the speckle decorrelation time caused by environmental perturbation is comparable to the signal light decorrelation time, the contribution from environments can overwhelm the signal itself. One viable solution to this problem is to use a fiber bundle to replace the large core multimode fiber. The mode mixing between the individual fibers in the bundle is less than that in the large core multimode fiber, thus it is less sensitive to environmental perturbation.

Before concluding the discussion section, we would like to speculate on the potential role of ISVS within the currently used clinical methods of accessing the information of CBF. Table 5.1, which is adapted from Refs. [12] and [29], outlines the features of the various non-invasive CBF measurement modalities, including ISVS. Since ISVS shares the similar light illumination and collection architectures with DCS, it inherits multiple advantages brought from DCS, such as bedside availability, endogenous contrast, radiation free, short data acquisition time, and low cost. Due to the multi-channel property brought by the camera, the data acquisition time for each measurement is significantly shortened compared to DCS. The shortened data acquisition time T_{acq} could help improve the sampling bandwidth up to $1/T_{\text{acq}}$, which can be up to hundreds or even thousands of Hz. In some cognitive tasks, such as cerebral blood flow signals during walking [30], high sampling speeds are required to record the quickly-changing signals for data analysis.

5.4 Appendix

Optical setup

The optical setup of the ISVS system is shown in Fig. 5.5. The beam from the laser (CrystaLaser, CL671-150) is split into a reference beam and a sample beam by a polarized beam splitter. The reference beam is coupled into a single mode fiber (FB1, Thorlabs, PM460-HP) for spatial filtering. The filtered beam is collimated by a single lens (L1) and illuminates on the camera (Phantom S640). The sample beam is coupled into a multimode fiber (FB2, Thorlabs M31L02) and the output beam is collimated and illuminates on the forehead of the human subject. The diffused light from the human subject is collected by a large core multimode fiber (Thorlabs M107L02). The output light field of the large core fiber is relayed onto the camera by

a 4-f system (L2 and L3). A beam splitter (BS2) combines the reference beam and sample beam. A custom designed aperture (AP) is put on the Fourier plane of the 4-f system. A polarizer (P) is put in the sample arm to filter out the cross-polarization portion of the diffused light. To record the scattered light from the sample using conventional DCS methods, a beam splitter (BS1) is added in front of BS2 and an SPCM (PerkinElmer, SPCM-AQRH-14) records the scattered light intensity.

System implementation on rat experiments

In the dorsal skin flap blood flow monitoring experiments, isoflurane (1-5%) administered in an induction box followed by maintenance on a nose cone was used to induce anesthesia on a regular laboratory rat. The dorsal skin flap of the rat was shaved and clipped on a glass slide. The rat was put on a 3-D translational stage and the illumination beam illuminated the dorsal skin flap. A 4-f system (L2 and L3, Fig. 5.5B) in the optical setup imaged the skin that diffused light.

In the dorsal skin flap blood flow monitoring experiments, ketamine 80-100 mg/kg and xylazine 8-10 mg/kg given via the intraperitoneal route was used to anesthetize a regular laboratory rat. The skin on the head and the scalp on top of the skull were surgically removed. The rat was put on a 3-D translational stage and the bregma and lambda areas were identified and illuminated by a collimated beam. A 4-f system (L2 and L3, Fig. 5.5B) in the optical setup imaged the part of skull that diffused light. The distance between the illumination spot and the imaging field of view was set about 1 cm.

Fourier plane aperture design

To maximize the bandwidth of the signal in the spatial frequency domain, we specifically designed the shape of the aperture on the Fourier plane of the light collection 4-f system (L2 and L3, Fig. 5.5A). This rectangular shape (shown in Fig. 5.7A) is different from conventional circular aperture shapes (shown in Fig. 5.7B), since here we cared primarily about collecting the maximum number of speckles rather than isotropic resolution in conventional imaging. The lateral size of the aperture was designed to avoid aliasing when performing off-axis holography.

The mathematical derivation of visibility factor

In this section, we derive the second moment of the interference term $S(\mathbf{r})$ in Eq. 5.4 in the main text. Previous work from [22] has shown similar theoretical derivation as shown below, where they analyzed the interferometric detection for dynamic

speckles in ultrasound modulated optical tomography.

$$
\begin{aligned}
&\langle |S(\mathbf{r})|^2 \rangle = \langle S(\mathbf{r}) \times S^*(\mathbf{r}) \rangle \\
&= \frac{1}{T} \Big\langle \int_0^T |E_\mathrm{R}||E_\mathrm{S}(\mathbf{r},t_1)| e^{i\phi_\mathrm{S}(\mathbf{r},t_1)} dt_1 \times \int_0^T |E_\mathrm{R}||E_\mathrm{S}(\mathbf{r},t_1)| e^{-i\phi_\mathrm{S}(\mathbf{r},t_1)} \Big\rangle dt_1 \\
&= \frac{I_R}{T^2} \int_0^T \int_0^T dt_1 dt_2 \Big\langle |E_\mathrm{S}(\mathbf{r},t_1)| e^{i\phi_\mathrm{S}(\mathbf{r},t_1)} |E_\mathrm{S}(\mathbf{r},t_2)| e^{-i\phi_\mathrm{S}(\mathbf{r},t_2)} \Big\rangle \\
&= \frac{I_R}{T^2} \int_0^T \int_0^T dt_1 dt_2 \Big\langle E_\mathrm{S}(\mathbf{r},t_1) E_\mathrm{S}^*(\mathbf{r},t_2) \rangle \\
&= \frac{I_R \bar{I_S}}{T^2} \int_0^T \int_0^T dt_1 dt_2 \; g_1(t_1 - t_2). \qquad (5.6)
\end{aligned}
$$

Here $g_1(t)$ is the field decorrelation function. Changing the integration variable by $\begin{cases} t = t_1 \\ \tau = t_1 - t_2 \end{cases}$, the integration in Eq. 5.6 can be written as

$$
\begin{aligned}
&\int_0^T \int_0^T dt_1 dt_2 g_1(t_1 - t_2) = \int_0^T \int_{-t}^t d\tau g_1(\tau) \\
&= \int_0^T \int_\tau^T dt g_1(\tau) + \int_{-T}^0 \int_{-\tau}^T dt g_1(\tau) \\
&= \int_0^T 2(1 - \frac{\tau}{T}) g_1(\tau) d\tau = \int_0^T 2(1 - \frac{t}{T}) g_1(t) \qquad (5.7)
\end{aligned}
$$

given $g_1(t)$ is symmetric. Therefore, Eq. 5.7 can be reduced to

$$
\langle |S(\mathbf{r})|^2 \rangle = \frac{I_R \bar{I_S}}{T^2} \int_0^T 2(1 - \frac{t}{T}) g_1(t). \qquad (5.8)
$$

The visibility factor is defined as $F = \frac{S(\mathbf{r})^2}{I_R \bar{I_S}} = \frac{1}{T} \int_0^T 2(1 - \frac{t}{T}) g_1(t)$ (shown in Eq. 5.5 in the main text). If $g_1(t)$ has a form of $g_1(t) = e^{-t/\tau}$ where τ is the speckle decorrelation time, after substituting in Eq. 5.8, we can get

$$
F = \frac{S(\mathbf{r})^2}{I_R \bar{I_S}} = \frac{2\tau}{T} [1 + \frac{\tau}{T} (e^{-\tau/T} - 1)]. \qquad (5.9)
$$

As $\tau \ll T$, $\tau/T \ll 1$ and the visibility factor F converges to $2\tau/T$.

In real cases, the visibility factor calculated from Eq. 5.9 has a non-zero offset. Even when no signal light photons hit the camera, there is still spatial fluctuations in the cropped side lobes due to camera noise. Taking square and summing up all the pixels give a non-zero offset that is related to camera noise. Therefore, in the

main text Fig. 2B, we use a camera noise corrected model to describe the visibility factor. The red curve in Fig. 2B has the expression of the corrected visibility factor F as

$$F = (1-\beta) + \beta\frac{2\tau}{T}[1 + \frac{\tau}{T}(e^{-\tau/T} - 1)] \tag{5.10}$$

where β equals 0.9.

Supplementary figures

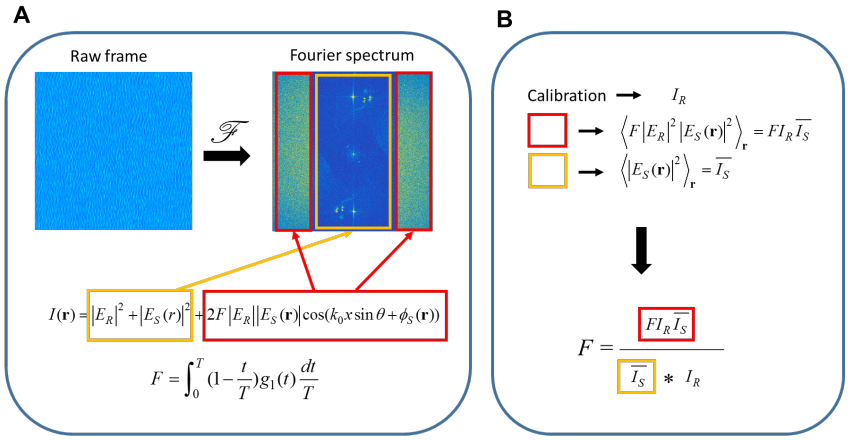

Figure 5.4: Flowchart of data processing. (A) The raw frame is Fourier transformed and three lobes contain the information of the reference beam and sample beam. The yellow enclosed circle and rectangle contain the intensity information of the reference beam and sample beam, and the red enclosed circle and rectangle contain the information of the visibility factor and the complex fields. (B) The reference beam calibration provides the mean value of the reference beam intensity, the red enclosed rectangle in (A) provides the mean value of the energy in one of the interference lobes, and the yellow enclosed rectangle in (A) provides the mean value of the sample beam intensity after subtracting the reference beam mean intensity. $< \cdot >$ denotes the ensemble average over space.

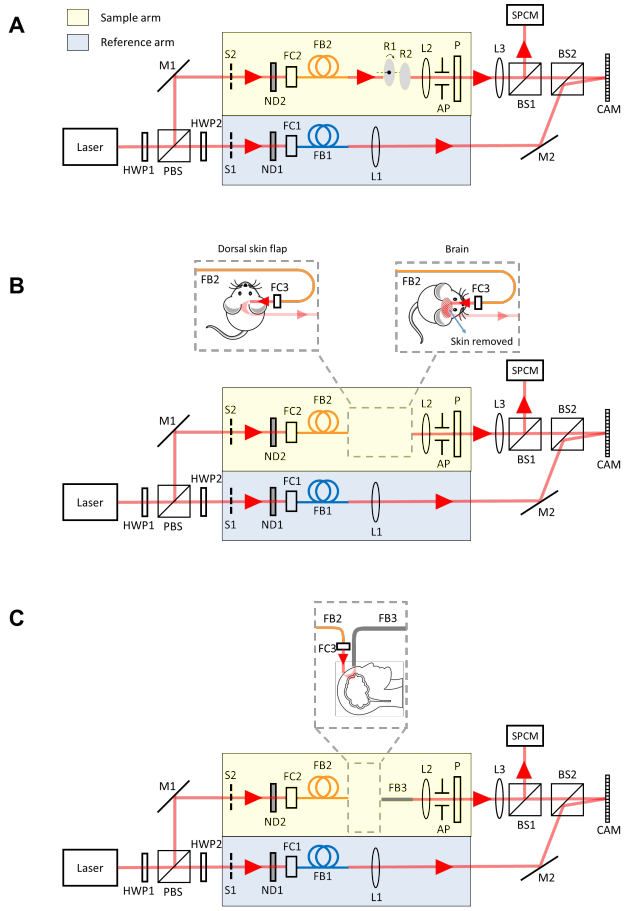

Figure 5.5: Schematic of the optical setup. (A) Optical setup for diffuser experiments. (B) Optical setup for animal experiments. (C) Optical setup for human experiments. AP, aperture; BS, beam splitter; CAM, camera; FB, fiber; FC, fiber coupler; HWP, half-wave plate; L, lens; M, mirror; ND, neutral-density filter; P, polarizer; SPCM, single photon counting module.

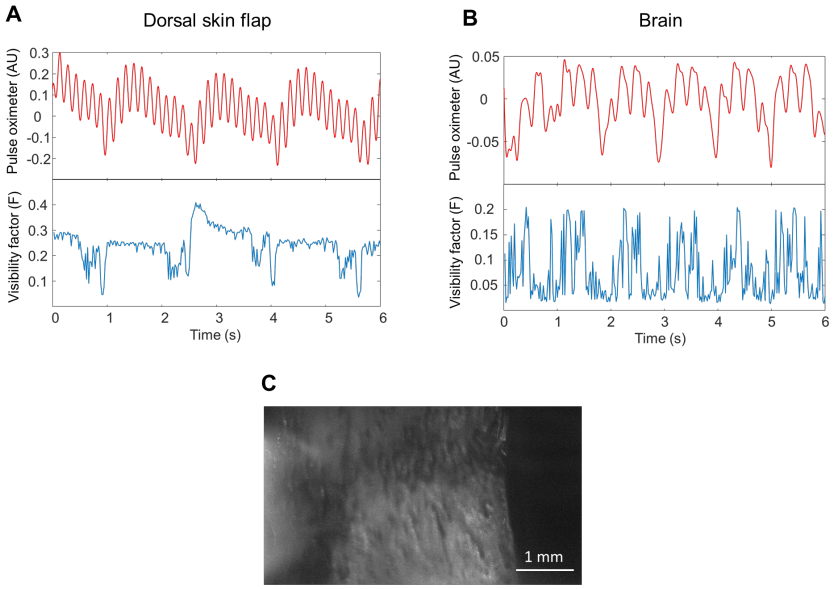

Figure 5.6: Results of rat experiments. (A) The results clearly show the breathing signal at 1.5 Hz from both the pulse oximeter and ISVS visibility factor signals (four big dips). Pulsatile signals at 3.5 Hz are shown in the pulse oximeter but not clearly shown in ISVS from the dorsal skin flap. This might be due to less arterial vessels in dorsal skin flap. (B) The results show the breathing signal at 1.0 Hz from both the pulse oximeter and ISVS visibility factor signals. Pulsatile blood flow signals in ISVS couple with the breathing signals in brain signal measurements. (C) The wide field image of the brain bregma area of the rat using white LED illumination. The pulse oximeter in both measurements samples at 1 kHz. The camera frame rate in the ISVS system in both measurements is set at 50 Hz and the exposure time is set as 16 ms.

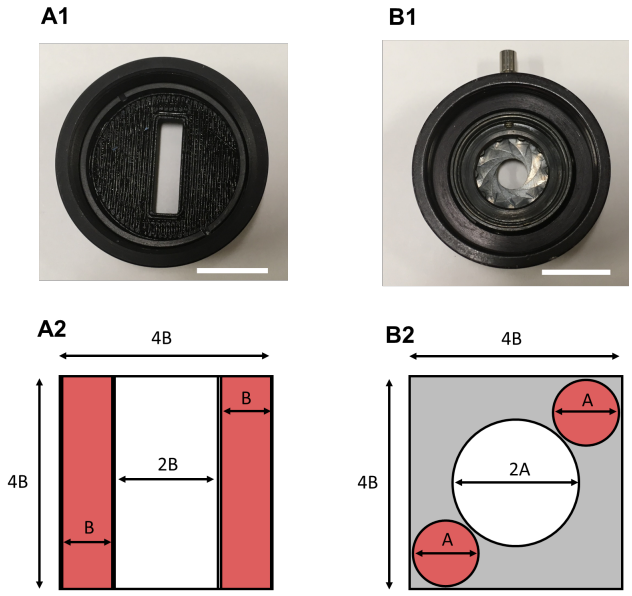

Figure 5.7: Fourier plane aperture design. (A1) Rectangular aperture. (A2) The Fourier spectrum of an off-axis hologram with a rectangular aperture. (B1) Circular aperture. (B2) The Fourier spectrum of an off-axis hologram with a circular aperture. Mathematically, it can be shown that $A = \frac{4\sqrt{2}}{3+\sqrt{2}}B \approx 1.28B$. Therefore, the circular aperture uses $\frac{2\pi A^2/4}{(4B)^2} \approx 16\%$ (red circles in (B2) of the Fourier space while the rectangular aperture uses 50% (red rectangles in (A2)) of the Fourier space. The larger area in Fourier space allows higher light collection efficiency. Scale bar, 1 cm.

References

[1] F. Jobsis. Noninvasive, infrared monitoring of cerebral and myocardial oxygen sufficiency and circulatory parameters. *Science*, 198(4323):1264–1267, December 1977.

[2] Cecil Cheung, Joseph P Culver, Kasushi Takahashi, Joel H Greenberg, and A G Yodh. In vivocerebrovascular measurement combining diffuse near-infrared absorption and correlation spectroscopies. *Physics in Medicine and Biology*, 46(8):2053–2065, July 2001.

[3] Theodore J. Huppert, Solomon G. Diamond, Maria A. Franceschini, and David A. Boas. HomER: a review of time-series analysis methods for near-infrared spectroscopy of the brain. *Applied Optics*, 48(10):D280, March 2009.

[4] Adam T. Eggebrecht, Silvina L. Ferradal, Amy Robichaux-Viehoever, Mahlega S. Hassanpour, Hamid Dehghani, Abraham Z. Snyder, Tamara Hershey, and Joseph P. Culver. Mapping distributed brain function and networks with diffuse optical tomography. *Nature Photonics*, 8(6):448–454, May 2014.

[5] H. C. Lou, L. Edvinsson, and E. T. MacKenzie. The concept of coupling blood flow to brain function: revision required? *Ann. Neurol.*, 22:289, 1987.

[6] U. Dirnagl, K. Niwa, U. Lindauer, and A. Villringer. Coupling of cerebral blood flow to neuronal activation: role of adenosine and nitric oxide. *American Journal of Physiology-Heart and Circulatory Physiology*, 267(1):H296–H301, July 1994.

[7] Erin M. Buckley, Ashwin B. Parthasarathy, P. Ellen Grant, Arjun G. Yodh, and Maria Angela Franceschini. Diffuse correlation spectroscopy for measurement of cerebral blood flow: future prospects. *Neurophotonics*, 1(1):011009, June 2014.

[8] Detian Wang, Ashwin B. Parthasarathy, Wesley B. Baker, Kimberly Gannon, Venki Kavuri, Tiffany Ko, Steven Schenkel, Zhe Li, Zeren Li, Michael T. Mullen, John A. Detre, and Arjun G. Yodh. Fast blood flow monitoring in deep tissues with real-time software correlators. *Biomedical Optics Express*, 7(3):776, February 2016.

[9] Laura D. Lewis, Kawin Setsompop, Bruce R. Rosen, and Jonathan R. Polimeni. Fast fMRI can detect oscillatory neural activity in humans. *Proceedings of the National Academy of Sciences*, 113(43):E6679–E6685, October 2016.

[10] Jonathan C. W. Brooks, Olivia K. Faull, Kyle T. S. Pattinson, and Mark Jenkinson. Physiological noise in brainstem fMRI. *Frontiers in Human Neuroscience*, 7, 2013.

[11] Turgut Durduran, Guoqiang Yu, Mark G. Burnett, John A. Detre, Joel H. Greenberg, Jiongjiong Wang, Chao Zhou, and Arjun G. Yodh. Diffuse optical measurement of blood flow, blood oxygenation, and metabolism in a human

brain during sensorimotor cortex activation. *Optics Letters*, 29(15):1766, August 2004.

[12] Turgut Durduran and Arjun G. Yodh. Diffuse correlation spectroscopy for non-invasive, micro-vascular cerebral blood flow measurement. *NeuroImage*, 85:51–63, January 2014.

[13] Borís Burle, Laure Spieser, Clémence Roger, Laurence Casini, Thierry Hasbroucq, and Franck Vidal. Spatial and temporal resolutions of EEG: is it really black and white? a scalp current density view. *International Journal of Psychophysiology*, 97(3):210–220, September 2015.

[14] Xin Zhang, Xu Lei, Ting Wu, and Tianzi Jiang. A review of EEG and MEG for brainnetome research. *Cognitive Neurodynamics*, 8(2):87–98, November 2013.

[15] Wenjun Zhou, Oybek Kholiqov, Shau Poh Chong, and Vivek J. Srinivasan. Highly parallel, interferometric diffusing wave spectroscopy for monitoring cerebral blood flow dynamics. *Optica*, 5(5):518, April 2018.

[16] Andrew K. Dunn, Hayrunnisa Bolay, Michael A. Moskowitz, and David A. Boas. Dynamic imaging of cerebral blood flow using laser speckle. *Journal of Cerebral Blood Flow & Metabolism*, 21(3):195–201, March 2001.

[17] R. Bandyopadhyay, A. S. Gittings, S. S. Suh, P. K. Dixon, and D. J. Durian. Speckle-visibility spectroscopy: a tool to study time-varying dynamics. *Review of Scientific Instruments*, 76(9):093110, September 2005.

[18] Andrew K. Dunn. Laser speckle contrast imaging of cerebral blood flow. *Annals of Biomedical Engineering*, 40(2):367–377, November 2011.

[19] Claudia P. Valdes, Hari M. Varma, Anna K. Kristoffersen, Tanja Dragojevic, Joseph P. Culver, and Turgut Durduran. Speckle contrast optical spectroscopy, a non-invasive, diffuse optical method for measuring microvascular blood flow in tissue. *Biomedical Optics Express*, 5(8):2769, July 2014.

[20] Mingjun Zhao, Siavash Mazdeyasna, Chong Huang, Nneamaka Agochukwu-Nwubah, Alisha Bonaroti, Lesley Wong, and Guoqiang Yu. Noncontact speckle contrast diffuse correlation tomography of blood flow distributions in burn wounds: a preliminary study. *Military Medicine*, 185(Supplement_1):82–87, September 2019.

[21] Mitsuo Takeda, Hideki Ina, and Seiji Kobayashi. Fourier-transform method of fringe-pattern analysis for computer-based topography and interferometry. *Journal of the Optical Society of America*, 72(1):156, January 1982.

[22] Altaf Hussain, Wiendelt Steenbergen, and Ivo M. Vellekoop. Imaging blood flow inside highly scattering media using ultrasound modulated optical tomography. *Journal of Biophotonics*, 11(1):e201700013, July 2017.

[23] T. Durduran, R. Choe, W. B. Baker, and A. G. Yodh. Diffuse optics for tissue monitoring and tomography. *Reports on Progress in Physics*, 73(7):076701, June 2010.

[24] A. Murray Harper. The inter-relationship between aPco2 and blood pressure in the regulation of blood flow through the cerebral cortex. *Acta Neurologica Scandinavica*, 41(S14):94–103, January 2009.

[25] C. M. Hesser, B. Katsaros, and G. Matell. Pulmonary and tissue gas exchange during breath holding with oxygen. *Respiration Physiology*, 5(1):78–90, June 1968.

[26] Juliette Selb, David A. Boas, Suk-Tak Chan, Karleyton C. Evans, Erin M. Buckley, and Stefan A. Carp. Sensitivity of near-infrared spectroscopy and diffuse correlation spectroscopy to brain hemodynamics: simulations and experimental findings during hypercapnia. *Neurophotonics*, 1(1):015005, August 2014.

[27] A. J. F. Siegert. On the fluctuations in signals returned by many independently moving scatterers, Radiation Laboratory, Massachusetts Insitute of Technology, 1943.

[28] Dawid Borycki, Oybek Kholiqov, and Vivek J. Srinivasan. Interferometric near-infrared spectroscopy directly quantifies optical field dynamics in turbid media. *Optica*, 3(12):1471, December 2016.

[29] Max Wintermark, Musa Sesay, Emmanuel Barbier, Katalin Borbély, William P. Dillon, James D. Eastwood, Thomas C. Glenn, Cécile B. Grandin, Salvador Pedraza, Jean-Francois Soustiel, Tadashi Nariai, Greg Zaharchuk, Jean-Marie Caillé, Vincent Dousset, and Howard Yonas. Comparative overview of brain perfusion imaging techniques. *Stroke*, 36(9), September 2005.

[30] Arthur Gatouillat, Héloïse Bleton, Jessie VanSwearingen, Subashan Perera, Scott Thompson, Traci Smith, and Ervin Sejdić. Cognitive tasks during walking affect cerebral blood flow signal features in middle cerebral arteries and their correlation to gait characteristics. *Behavioral and Brain Functions*, 11(1), September 2015.

Chapter 6

DIFFUSING WAVE SPECTROSCOPY: A UNIFIED TREATMENT ON TEMPORAL SAMPLING AND SPATIAL ENSEMBLE METHODS

This chapter contains unpublished content from a manuscript in preparation.

Diffusing wave spectroscopy (DWS) is a well-known method to measure the temporal dynamics of dynamic samples. In DWS, dynamic samples scatter the incident coherent light, and the information of the temporal dynamics is encoded in the scattered light. To record and analyze the light signal, there exist two types of methods – temporal sampling methods and spatial ensemble methods. Temporal sampling methods, including diffuse correlation spectroscopy (DCS), use one or multiple large bandwidth detectors to well sample and analyze the temporal light signal to infer the sample temporal dynamics. Spatial ensemble methods, including speckle visibility spectroscopy (SVS), use a high-pixel-count camera sensor to capture a speckle pattern and use the speckle contrast to infer sample temporal dynamics. The two methods seem independent but there are fundamental similarities in terms of their measurement accuracy. In this work, to our knowledge, for the first time we theoretically and experimentally demonstrate that the measurement accuracy of the two sets of methods has a unified expression that is determined by the physical conditions. The fundamental limitations of both methods are the number of independent measurements (NIM) and photon budget. Under the shot noise dominant condition, with the same experimental NIM and photon budget, the two sets of methods should provide sample dynamic measurements with similar accuracy. By applying temporal sampling methods and spatial ensemble methods simultaneously to monitor the human cerebral blood flow (CBF), we experimentally observe that spatial ensemble methods have a higher signal-to-noise ratio (SNR) in CBF measurements, mainly due to more NIM achieved by spatial ensemble methods compared to temporal sampling methods. By using the spatial ensemble method, we achieved the blood pulsatile flow measurement with a 100-fold lower photon flux than the common experimental conditions in conventional temporal sampling methods.

6.1 Introduction

Diffusing wave spectroscopy (DWS) [1, 2] is a well-established approach that is used to measure the temporal dynamical properties of dynamic samples, such as in vivo blood flow monitoring [3], air turbulence quantification [4], and particle diffusion in liquid solution [5]. A common experimental setting of DWS is to use a coherent laser source to illuminate the dynamic sample and measure the scattered light. The scattered light forms a dynamic speckle pattern in which the information of the sample dynamics is encoded, therefore the sample temporal dynamics can be inferred by analyzing the intensity of scattered light. Recently, DWS has been widely applied in biomedical and clinical areas [3, 6, 7, 8, 9, 10, 11], especially in monitoring cerebral blood flow (CBF). In such applications, researchers typically utilize red or near-infrared light to illuminate the brain through skin, probe the dynamic scattering light that interacts with the brain, and analyze the recorded light signal to infer the information of CBF.

Since the dynamic of the light signal is tied to the temporal dynamic of the dynamic sample, there exist two sets of methods to measure the light signal to attain the information of the temporal dynamic – one is to use temporal sampling methods, and the other one is to use spatial ensemble methods. Both methods share the similar light illumination systems (Fig. 6.1a), and the difference is that they collect and analyze the light signal differently.

Temporal sampling methods, including diffuse correlation spectroscopy [1, 3, 4, 5, 6, 7], utilize one or multiple large bandwidth detectors to record the intensity fluctuation of one or a few speckle grains, and analyze the temporal signal to reconstruct the information of the temporal dynamics. The recorded intensity fluctuation trace $I(t)$, where t denotes time, is autocorrelated and normalized to approximate the intensity correlation function $g_2(t)$, i.e., $g_2(t) = \frac{<I(t_1)I(t_1-t)>}{<I(t_1)^2>}$ where $< \cdot >$ denotes the average over time variable t_1. According to the Siegert relation [12], the intensity correlation function $g_2(t) = 1 + |g_1(t)|^2$, where $g_1(t) = \frac{<E(t_1)E(t_1-t)>}{<E(t_1)^2>}$ is the electric field ($E(t)$) correlation function. Speckle decorrelation time is introduced to describe the time scale during which decorrelation happens. Generally, speckle decorrelation time τ is defined as the time point when the temporal autocorrelation function $g_1(t)$ drops below a certain threshold. A common model is $g_1(t) = \exp(-t/\tau)$ and the time instant that $g_1(t)$ drops to $1/e$ is defined as the decorrelation time. The autocorrelation function of the intensity fluctuation signal can be used to approximate $g_2(t)$, and it then can be calculated to obtain the speckle decorrelation time and scattering

dynamics (Fig. 6.1b). Figure 6.1c gives examples of field decorrelation functions with a short decorrelation time and a long decorrelation time.

Typical spatial ensemble methods, including speckle visibility spectroscopy (SVS) [13, 14] (a.k.a. speckle contrast spectroscopy [9]) and laser speckle contrast imaging (LSCI) [11, 15], use a camera sensor as a detector to record a frame of the speckle pattern. The camera exposure time is longer than the speckle decorrelation time (empirically one order of magnitude longer than the decorrelation time), therefore multiple different speckle patterns sum up within the exposure time, yielding a blurring speckle pattern. The decorrelation time is then calculated from the degree of blurring – more specifically, from the speckle contrast over the speckles in the whole frame. The speckle contrast γ relates with $g_1(t)$ in the form of $\gamma^2 = \int_0^T 2(1-\frac{t}{T})|g_1(t)|^2 dt$ (See Ref. [13] and Section 6.6). From the measured speckle pattern, we can calculate γ to get the information of $g_1(t)$, and consequently obtain the information of the sample dynamics (Fig. 6.1b). Generally, shorter decorrelation time will cause a lower contrast speckle frame. Figure 6.1d gives examples of speckle frames with a short decorrelation time and a long decorrelation time.

Since the aforementioned two sets of methods share similar optical illumination but use different detection principles, it is worth exploring the fundamental limitations and jointly analyzing the performance of the two methods. Some of the previous research have investigated the performance of the two individual methods from some aspects. For instance, ref [16] discusses the effect of finite sampling time in temporal sampling methods; ref [14] discusses the effect of shot noise in spatial ensemble methods. Here, we jointly realize a unified analysis on the performance of the two sets of methods, and show the equivalence of the measurement accuracy of the two methods. Interestingly, we find a unified expression for the two methods with respect to the measurement accuracy. The accuracy of decorrelation time measurements from both sets of methods is determined by the number of independent measurements (NIM) and the amount of photon flux. In temporal sampling methods, NIM is the number of decorrelation events recorded by the detector, while in spatial ensemble methods, it is the number of collected speckle grains. The NIM equivalence of the two methods fundamentally is due to the equivalence of speckle spatial ensemble and temporal ensemble.

Under typical experimental conditions where photon shot noise is the dominant noise source in the measurement, the two sets of methods should provide decorrelation measurements with similar accuracy, given the same the number of independent

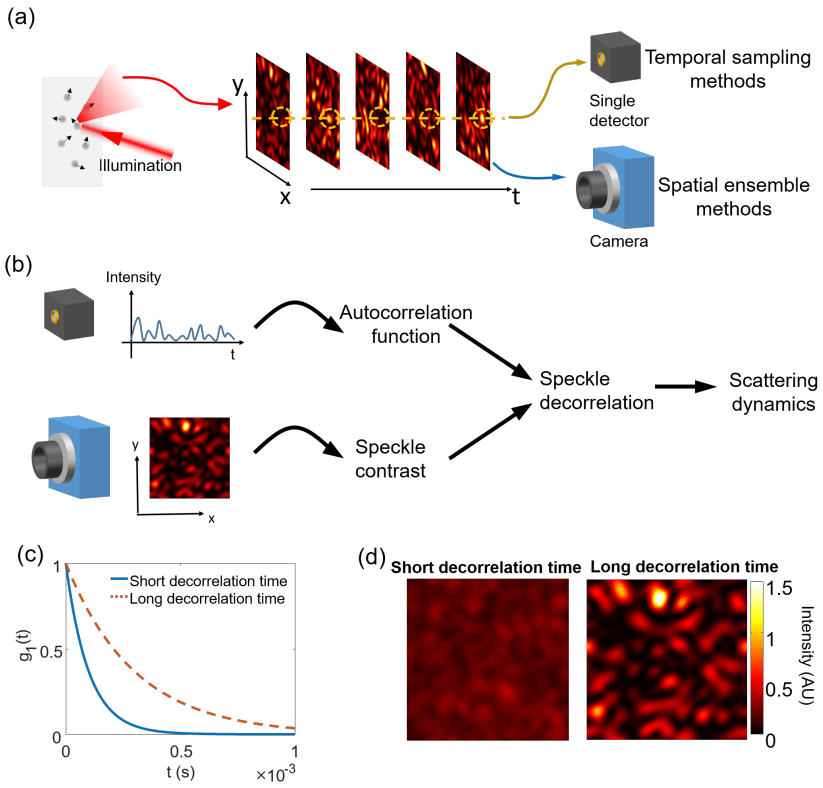

Figure 6.1: An overview of scattered light dynamics measurement. (a) After the illumination light interacts with the dynamic scatterers, the scattered light forms a set of dynamic speckle patterns. Temporal sampling methods usually use a high speed detector to record the intensity temporal fluctuation, while spatial ensemble methods usually use a camera sensor to record the speckle patterns. (b) Temporal sampling methods calculate the autocorrelation function of the recorded intensity fluctuation to obtain the speckle decorrelation time. Spatial ensemble methods calculate the speckle contrast and use mathematical models to obtain the speckle decorrelation time. In both methods, the calculated speckle decorrelation time is used to infer the scattering dynamics. (c) Examples of field decorrelation functions with a short and a long decorrelation times in temporal sampling methods. (d) Examples of speckle frames with a short and a long decorrelation times in spatial ensemble methods.

measurements (NIM) and photon flux. In the experiment, we observe that spatial ensemble methods have higher signal-to-noise ratio (SNR) in CBF measurements with a fixed sampling rate, mainly due to more NIM achieved by a camera sensor compared to a single-photon-counting-module (SPCM) per unit time.

6.2 Theory

To start the quantitative analysis on the two sets of methods, let us first define the NIM for temporal sampling methods and spatial ensemble methods. In temporal sampling methods, NIM is defined as $2T/\tau$, where T is the time duration of the measured temporal trace, and τ is the speckle field decorrelation time. The constant 2 in $2T/\tau$ is introduced to match the conversion between $g_1(t)$ and $g_2(t)$. The SNR of the measured decorrelation time τ, which is defined as the expected decorrelation time τ devided by $error(\tau)$ (error of τ in the measurement), has the form of (Section 6.6, Eq. 6.38)

$$SNR_{temporal} = \frac{\sqrt{2}}{e} \frac{1}{\sqrt{1 + \frac{2}{N_\tau} + \frac{2}{N_\tau^2}\frac{\tau}{\Delta T}}} \sqrt{M_{temporal}}. \tag{6.1}$$

Here, N_τ is the average number of photons in one speckle grain per time τ, and $M_{temporal}$ is the NIM in temporal sampling methods. The detailed derivation is shown in Section 6.6.

In spatial ensemble methods, the NIM is defined as the number of independent speckle grains captured by the camera sensor. In typical cases where the size of speckle grains is larger than the camera pixel size, we can use the mutual coherence function [17] to estimate the speckle size. The SNR of the measured decorrelation time τ has the form of (Section 6.6, Eq. 6.27)

$$\begin{aligned} SNR_{spatial} &= \frac{1}{\sqrt{2}} \frac{1}{1 + \frac{1}{N_\tau}} \sqrt{M_{spatial}} \\ &= \frac{1}{\sqrt{2}} \frac{1}{\sqrt{1 + \frac{2}{N_\tau} + \frac{1}{N_\tau^2}}} \sqrt{M_{spatial}}. \end{aligned} \tag{6.2}$$

N_τ has the same definition as in the temporal sampling methods. $M_{spatial}$ is the NIM in spatial ensemble methods. The detailed derivation is shown in Section 6.6.

Equations 6.2 and 6.1 reveal that the two sets of methods have similar dependency on photon flux N_τ and NIM. The unified mathematical expression shows the equivalence of spatial ensemble and temporal sampling. The SNR of both methods scales up with NIM in a square root relation. From a mathematical perspective, we are estimating a statistical parameter (decorrelation time τ) from the data, and the accuracy (SNR of τ) of the estimation increases with the number of independent sampling points (NIM in this case) according to central limit theorem. The photon flux affects the SNR of the decorrelation time measurements in another manner. Only when

N_τ is smaller or comparable to one, which means on average there is only one or less photon in one speckle grain per decorrelation time τ, the SNR of the measured decorrelation time τ starts to be affected by N_τ. Fundamentally, the dependency of N_τ comes from shot noise. When N_τ is large, i.e. $N_\tau >> 1$, shot noise is negligible compared to the light fluctuation induced by the scatterers. When N_τ is small, i.e. N_τ is smaller or comparable to 1, the light intensity fluctuation induced by shot noise is larger or comparable to the fluctuation induced by the scatterers.

From Eqs. 6.1 and 6.2, we notice that the SNR of the two sets of methods only differ by a constant when $N_\tau >> 1$. However, when $N_\tau << 1$, temporal sampling methods tend to behave worse than spatial ensemble methods, due to a larger constant factor in front of N_τ^2. Under the photon sufficient condition where $N_\tau >> 1$ and the same NIM, the two methods yield the decorrelation time measurement with similar accuracy. Since the SNR "saturates" with respect to N_τ when $N_\tau >> 1$, the practical way of high accuracy decorrelation time measurements is to increase NIM under the photon sufficient condition ($N_\tau >> 1$).

6.3 Experiment

We performed experiments to verify the SNR equations (Eq. 6.1 and Eq. 6.2) of decorrelation time measurements in both temporal sampling and spatial ensemble methods. The experimental setup is shown in Fig. 6.3. A laser beam (laser model number: CrystaLaser, CL671-150, wavelength 671 nm) is coupled into a multimode fiber FB1, and the output beam from the fiber illuminates the sample (in the gray dashed line box). The scattered light is collected by a 4-f system (L1 and L2), and is split onto a camera and an SPCM (PerkinElmer, SPCM-AQRH-14), respectively. In the diffuser experiment where we verified the models for the two sets of methods, the light passes a rotating diffuser and a static diffuser, and the scattered light is directly collected by the 4-f system. In the human experiment where we demonstrated the NIM advantage of spatial ensemble methods over temporal sampling methods, the light illuminates the skin of the human subject, and diffused light at a source-detector (S-D) separation of 1.5 cm is collected by a large core multimode fiber FB2 (Thorlabs M107L02, core diameter 1.5 mm, containing 6 million modes) and directed to the 4-f system.

In the human experiment, the 56 mW laser beam with a 6-mm spot size results in a $< 2mW/mm^2$ irradiance for skin exposure – within the limit stipulated by American National Standard Institute (ANSI). The output of this fiber was channeled to the

camera. A human protocol comprising of all detailed experimental procedures were reviewed and approved by the Caltech Institutional Review Board (IRB) under IRB protocol 19-0941, informed consent was obtained in all cases, and safety precautions were implemented to avoid accidental eye exposure.

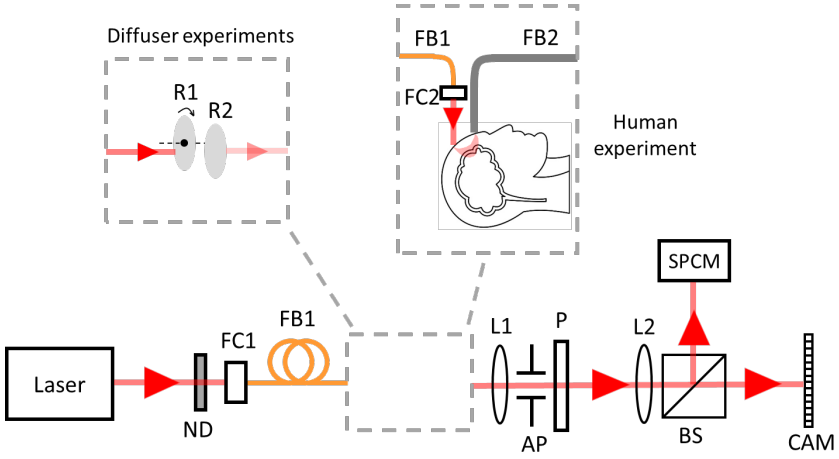

Figure 6.2: Experimental setup. AP, aperture; BS, beam splitter; CAM, camera; FB, fiber; FC, fiber coupler; L, lens; ND, neutral density filter; P, polarizer; R, rotating diffuser; SPCM, single photon counting module.

The experimental results confirm our theoretical analysis. We first verified the relation between SNR and NIM, given a fixed photon flux N_τ. Figure 6.3 shows the relation between the SNR and the NIM under the photon sufficient case, for both temporal sampling and spatial ensemble methods. In the experiment, N_τ is set to be $\sim$ 10. In both methods, the square of the SNR scales up linearly with the NIM, as predicted by the theoretical analysis. Due to the approximation in the theoretical analysis (Section 6.6) and experimental imperfections such as detector noise and non-perfect control of the diffuser rotating speed, the experimental SNR^2 scales up slower compared to the theoretical line. This results in a gap between the experimental dots and the theoretical line in the log-log plot (Fig. 6.3c,d). The experimentally measured decorrelation times at different NIM are demonstrated in Fig. 6.3a,b. Both methods can consistently measure the decorrelation time, with less errors as NIM increases. Figure 6.3e shows examples of the autocorrelation functions from intensity temporal fluctuation traces with different NIM. Under such photon sufficient condition, less NIM will cause the "shape deviation" from the expected autocorrelation function. Intuitively speaking, the number of sampled decorrelation events is not statistically sufficient to be representative for the whole decorrelation process. Figure 6.3f shows a speckle frame from the spatial ensemble

method, with the enclosed red and white boxes containing different numbers of speckle grains. The speckle contrast calculated from a small enclosed box will give a relatively large error from the expected contrast. Similar as in the temporal sampling method, here in the spatial ensemble method, a small enclosed box does not contain a statistically sufficient number of speckle grains to be representative for all the speckle grains in the frame.

We then verified the relation between SNR and photon flux N_τ, given a fixed NIM. Figure 6.3 shows the relation between the SNR and N_τ when NIM is set to be 300, for both temporal sampling and spatial ensemble methods. In both methods, the SNR does not change much under the photon sufficient case (N_τ>10), while it starts to decrease when N_τ is comparable to 1. Figure 6.3e shows examples of the autocorrelation functions from intensity temporal fluctuation traces with different N_τ. In this case, a small N_τ will cause more fluctuation in the calculated autocorrelation function. Different from the case of small NIM where the autocorrelation function remains smooth but has a "shape deviation" from the expected autocorrelation function, a small N_τ here contributes more "noise" on the calculated autocorrelation function. From Eqs. 6.31 and 6.32 in Section 6.6, the fluctuation of the autocorrelation function fundamentally comes from the autocorrelation operation of the noise in the intensity measurement. Figure 6.3f shows speckle frames from the spatial ensemble method with different N_τ. The low N_τ speckle frame looks noisier than the high N_τ frame due to more shot noise. The shot noise would also contribute to the contrast calculation and subsequently introduces more errors.

We then implemented both methods to measure human CBF. To well sample the pulsatile effect due to heartbeats, the sampling rate for both methods is set as 18 Hz. The experimental results demonstrate that the spatial ensemble method can reveal the pulsatile effect of the blood flow, while the single channel temporal sampling method cannot.

Under the experimental condition, the photon flux is $\sim N_\tau = 0.1$, and the total photon rate is ~1000/(pixel·second), which is in the photon starved situation. Figure 6.3a shows the measured decorrelation time of the blood flow by the temporal sampling method (DCS). No obvious pulsatile effect is shown in the plot because of the low measurement SNR. Figure 6.3c1–6.3c3, corresponding to different enclosed boxes in Fig. 6.3b, show the measured speckle decorrelation time of the blood flow by the spatial ensemble method (SVS) over different numbers of pixels used in the measurement. In the spatial ensemble method, the measurement SNR increases as

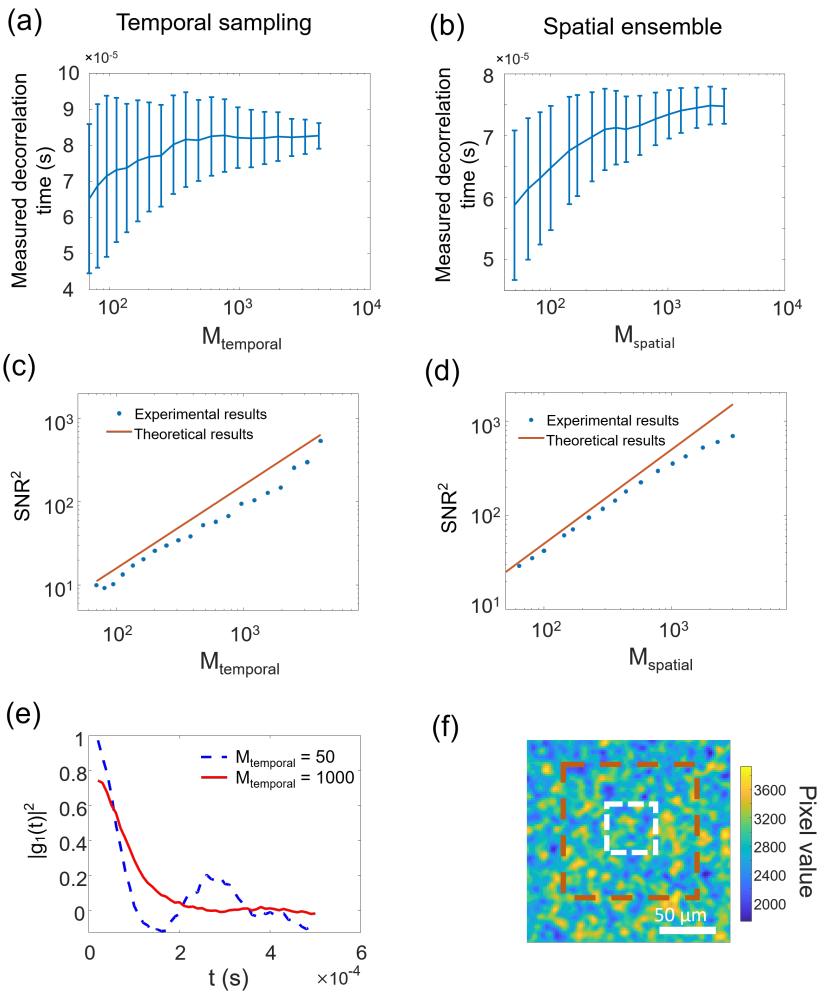

Figure 6.3: The performance of temporal sampling and spatial ensemble methods with respect to different NIM. (a) Temporal sampling measured speckle decorrelation time with respect to varying NIM. The error bar is calculated from 30 data points. (b) Spatial ensemble measured speckle decorrelation time with respect to varying NIM. The error bar is calculated from 30 data points. (c) The square of SNR with respect to varying NIM in the temporal sampling methods. (d) The square of SNR with respect to varying NIM in the spatial ensemble methods. (e) Examples of the autocorrelation functions from intensity temporal fluctuation traces with different NIM. (f) An examples of a speckle frame used to calculate speckle contrast. The red enclosed box indicates a large NIM, and the white enclosed box indicates a small NIM.

the number of pixels used on the camera increases. When the number of pixels is larger than 3025, the pulsatile effect is clearly shown by the spatial ensemble method.

The reason to the above performance difference between the two sets of methods

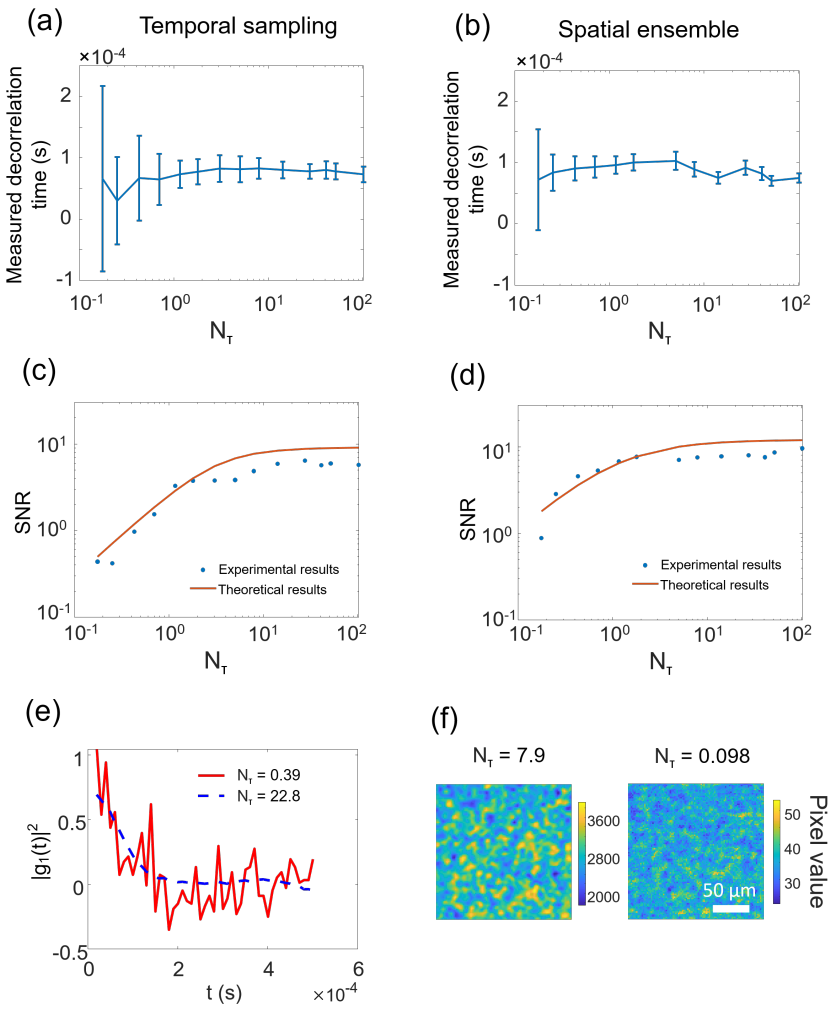

Figure 6.4: The performance of temporal sampling and spatial ensemble methods with respect to different N_τ. (a) Temporal sampling measured speckle decorrelation time with respect to varying N_τ. The error bar is calculated from 30 data points. (b) Spatial ensemble measured speckle decorrelation time with respect to varying N_τ. (c) SNR with respect to varying N_τ in the temporal sampling methods. The error bar is calculated from 30 data points. (d) SNR with respect to varying N_τ in the spatial ensemble methods. (e) Examples of the autocorrelation functions from intensity temporal fluctuation traces with different N_τ. (f) Examples of the speckle frames with different N_τ.

is tied to the achievable NIM. Under the experimental condition, the photon flux is limited by safety limit. Therefore, a high SNR measurement can only be achieved by a large NIM. In temporal sampling methods, a larger NIM is achieved by measuring more decorrelation events ($2T/\tau$), while in spatial ensemble methods, a larger NIM is achieved by measuring more speckles. Since the sampling rate is fixed to 18 Hz

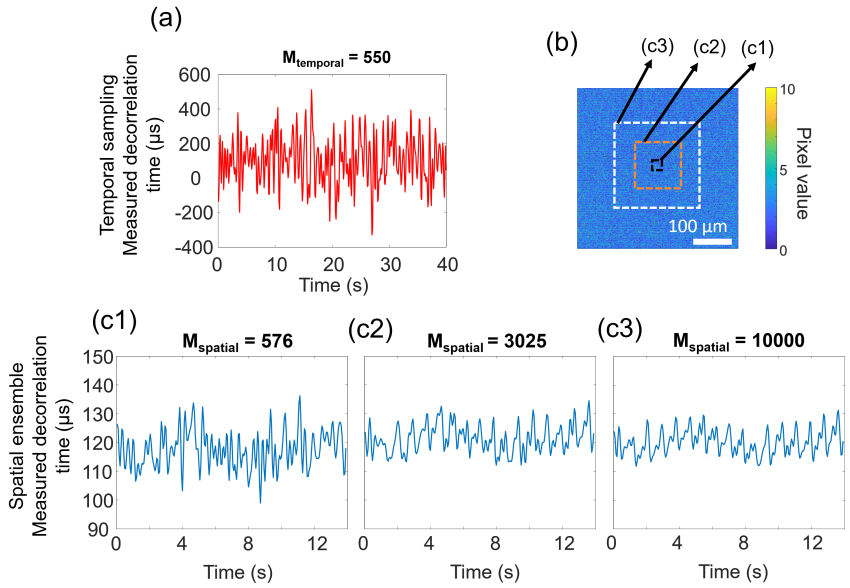

Figure 6.5: Human CBF induced speckle decorrelation time measurement results from temporal sampling and spatial ensemble methods. (a) Results from the temporal sampling method. (b) A speckle frame from the spatial ensemble method. The white, orange, and black boxes enclose 10000, 3025, and 576 speckle grains, respectively. (c) Results from the spatial ensemble method, with different NIM ($M_{spatial}$).

(56 ms sampling time) and the speckle decorrelation time is mostly determined by CBF (decorrelation time 0.1 ms), the NIM in temporal sampling is fixed to 550. In spatial ensemble methods, increasing the NIM (measuring more speckles) does not affect the sampling rate. In the experiment, the NIM in the spatial ensemble method can achieve more than 10^4. The difference of achievable NIM between the temporal sampling method and the spatial ensemble method determines the performance difference of the two sets of methods in the speckle decorrelation time measurement.

In previous temporal sampling methods, to achieve a similar CBF sampling rate with a reasonable measurement SNR, the required photon flux is ~100k/(speckle·second) [18]. In the meantime, costly SPCMs are required to measure the temporal intensity fluctuation. In our demonstrated spatial ensemble method, the photon flux is ~1k/(speckle·second), and a common camera sensor is used to measure the diffusing photons. Therefore, the use of a camera sensor relaxes the requirement of the photon budget by two orders of magnitude, and has the potential to allow us to do deeper tissue measurement.

6.4 Discussion

Our results summarize the performance of the two sets of DWS decorrelation time measurements, temporal sampling and spatial ensemble methods, and demonstrate that they only depend on NIM and photon flux under the shot noise dominant condition. When $N_\tau >> 1$, i.e. the photon flux is sufficient, the bottle neck of the measurement accuracy is limited by NIM. Since the SNR of the measurement scales up with NIM by a similar constant in the two sets of methods, we can conclude that they have similar "NIM efficiency", i.e., each independent measurement represents "similar amount" of information. However, for one independent measurement, temporal sampling methods require 10 data points or more to construct the decorrelation function, while spatial ensemble methods only require one pixel if we match the speckle size and pixel size. Therefore, spatial ensemble methods can have higher "data efficiency".

Based on the current technology, common camera sensors usually support larger data throughputs than common high bandwidth single detectors. Combining with the higher "data efficiency", spatial ensemble methods should yield more NIM per unit time than temporal sampling methods. Therefore, at the current stage, spatial ensemble methods tend to provide better performance compared to temporal domain methods given the same light illumination and collection architecture. As an example shown in the experimental results, CBF measurement experiment demonstrate the advantage of spatial ensemble methods over temporal sampling methods. Since commercial camera sensors can have millions of pixels, while in Fig. 6.3c we show that ~3k pixels are sufficient to monitor the blood flow, there is potential for spatial ensemble methods to do parallel measurements in multiple regions of human brains by using a single camera sensor.

There is a paradox that if the camera exposure time is much longer than the speckle decorrelation time, spatial ensemble methods will have an extremely low contrast, which might be difficult to be measured accurately. However, this paradox in fact does not hold because the SNR expression in Eq. 6.2 is independent on the camera exposure time. In fact, the accuracy of the contrast measurement is mainly determined by the accuracy of the intensity variance measurement (from Section 6.6, Eq. 6.19), while the mean intensity only scales the intensity variance. Section 6.6, Eq. 6.19 shows that the intensity variance measurement only depends on the NIM in the measurement if the camera exposure time is much longer than the speckle decorrelation time. Therefore, the accuracy of the contrast measurement also only

depends on the NIM, with no dependency on the contrast value itself.

In general, the analysis of temporal sampling and spatial ensemble methods can be extended to interferometric measurements. In this case, the counterparts of DCS and SVS are IDCS and ISVS [19, 20], respectively. We expect that similar results will also hold in the interferometric schemes, as the mathematical derivations are similar for the direct detection discussed in this work and interferometric detection.

The drawback of spatial ensemble methods is that they can only provide a measure of the decorrelation time scale, but cannot quantify the exact shape of the decorrelation function. In practice, the combination of the two sets of methods should be able to comprehensively measure the scattering dynamics with high "data efficiency". Temporal sampling methods can be applied first to quantify the shape of the decorrelation function, while spatial ensemble methods can be applied later to efficiently monitor the relative change of the dynamic scattering.

6.5 Summary

In conclusion, we performed systematical analysis on temporal sampling methods and spatial ensemble methods for DWS dynamic scattering measurements. Our theoretical and experimental results demonstrate that the accuracy of two sets of methods is dependent on the number of independent measurements and the photon flux. The two sets of methods have similar dependency on the NIM and photon flux. Under the condition where the photon flux is sufficient, the two sets of methods have similar measurement accuracy. We implemented the two sets of methods simultaneously to measure the human CBF, and observed that spatial ensemble methods were able to quantify the CBF with better accuracy than temporal sampling methods, due to larger achievable NIM. We hope our findings could provide the researchers in the field with a guideline to choosing appropriate approaches for dynamic scattering quantification.

6.6 Appendix

SNR of decorrelation time measurements in spatial ensemble methods

When the light is reflected from the dynamic sample, the light intensity at position r and time t, $I_r(t)$, can be decoupled into two parts,

$$I_r(t) = I_{r,S}(t) + n(t), \tag{6.3}$$

where $I_{r,S}(t)$ is the intensity of one speckle of the signal light that is perturbed by the scattering media, and $n(t)$ is the intensity fluctuation from noise, such as shot

noise and detector noise. By the definition of noise, $n(t)$ has zero mean. $I_{r,S}(t)$ follows exponential distribution due to speckle statistics [17]. For convenience, we define the AC part of $I_{r,S}(t)$ and $I_r(t)$ as $\tilde{I}_{r,S}(t)$ and $\tilde{I}_r(t)$, respectively, therefore we have

$$\tilde{I}_r(t) = \tilde{I}_{r,S}(t) + n(t). \tag{6.4}$$

Here, both $\tilde{I}_{r,S}(t)$ and $\tilde{I}_r(t)$ are zero mean, and

$$\langle \tilde{I}_{r,S}(t) \rangle = \sqrt{\langle \tilde{I}_{r,S}(t) \rangle} = I_0 \tag{6.5}$$

due to speckle statistics [17]. Here, $\langle \cdot \rangle$ denotes the expected value and I_0 is the expected value of $I_{r,S}(t)$.

Define the signal S_r recorded on the camera pixel located at position r as

$$S_r = \int_0^T \alpha I_r(t) dt, \tag{6.6}$$

where α is the factor that relates the photon numbers to photoelectrons on camera pixels, including detector quantum efficiency, light collection efficiency, and other experimental imperfections, and T is the camera exposure time.

The speckle contrast γ among the whole camera frame is defined as

$$\gamma = \sqrt{\frac{\langle (S_r - \langle S_r \rangle)^2 \rangle}{\langle S_r \rangle^2}} \text{ or } \gamma^2 = \frac{\langle (S_r - \langle S_r \rangle)^2 \rangle}{\langle S_r \rangle^2}. \tag{6.7}$$

The numerator of the γ^2 is

$$\begin{aligned} \gamma_{up}^2 &= \langle (S_r - \langle S_r \rangle)^2 \rangle \\ &= \langle (\int_0^T \alpha \tilde{I}_r(t) dt)^2 \rangle \\ &= \langle \int_0^T \int_0^T \alpha^2 \tilde{I}_r(t_1) \tilde{I}_r(t_2) dt_1 dt_2 \rangle . \end{aligned} \tag{6.8}$$

Substituting equation 6.4 into Eq. 6.8, we have

$$\begin{aligned} \gamma_{up}^2 &= \langle \int_0^T \int_0^T \alpha^2 \tilde{I}_{r,S}(t_1) \tilde{I}_{r,S}(t_2) dt_1 dt_2 \rangle + \langle \int_0^T \int_0^T \alpha^2 n(t_1) n(t_2) dt_1 dt_2 \rangle \\ &= \alpha^2 \langle \tilde{I}_r^2 \rangle \int_0^T \int_0^T g_S(t_1 - t_2) dt_1 dt_2 + \alpha^2 \langle n^2 \rangle \int_0^T \int_0^T g_n(t_1 - t_2) dt_1 dt_2 \\ &= \alpha^2 \langle \tilde{I}_r^2 \rangle T \int_0^T 2(1 - \frac{t}{T}) g_S(t) dt + \alpha^2 \langle n^2 \rangle T \int_0^T 2(1 - \frac{t}{T}) g_n(t) dt. \end{aligned} \tag{6.9}$$

Here, $g_S(t)$ is the correlation function of the mean-removed signal light intensity, and $g_n(t)$ is the correlation function of noise. If we assume $g_S(t) = e^{-2t/\tau}$ and $g_n(t) = e^{-t/\tau_n}$, where τ is the decorrelation time of the speckle decorrelation time and τ_n (related to the detector bandwidth BW, 1/BW) is the noise decorrelation time, the above equation can be simplified as

$$\gamma_{up}^2 = \alpha^2 \langle \tilde{I}_r^2 \rangle T\tau + 2\alpha^2 \langle n^2 \rangle T\tau_n. \tag{6.10}$$

If the detector is working under the shot noise dominant scheme, where the mean of the number of photoelectrons is equal to the standard deviation of the number of photoelectrons, we have

$$\begin{aligned} \alpha I_0 T &= \langle (\int_0^T \alpha n(t) dt)^2 \rangle \\ &= 2\alpha^2 \langle n^2 \rangle T\tau_n. \end{aligned} \tag{6.11}$$

Substituting the above equation and Eq. 6.5 into Eq. 6.10, the numerator of the contrast square can be further simplified as

$$\gamma_{up}^2 = \alpha^2 I_0^2 T\tau + \alpha I_0 T. \tag{6.12}$$

The denominator of γ is

$$\gamma_{down} = \langle S_r \rangle = \alpha I_0 T. \tag{6.13}$$

Hence, the contrast has the expression of

$$\begin{aligned} \gamma^2 &= \frac{\gamma_{up}^2}{\gamma_{down}^2} \\ &= \frac{\alpha^2 I_0^2 T\tau + \alpha I_0 T}{(\alpha I_0 T)^2} \\ &= \frac{\tau}{T} + \frac{1}{\alpha I_0 T} \\ &= \frac{\tau}{T} + \frac{1}{N_T} \end{aligned} \tag{6.14}$$

where N_T is the number of the photoelectrons in one speckle within the camera exposure time. Conventional speckle statistics without considering shot noise predicts that the speckle contrast scales with respect to $1/\sqrt{N_{pattern}}$, where $N_{pattern}$ is the number of independent decorrelation patterns recorded by the camera sensor within the exposure time. Intuitively, $N_{pattern}$ is $\sim T/\tau$ since the ratio provides the number of decorrelation events within the camera exposure time. Here, the extra term $1/N_T$

in Eq. 6.14 is due to shot noise, i.e., depending on the photon budget. If the number of photoelectrons is sufficient, i.e., $1/N_T << \tau/T$, we can discard this term and the expression degenerates to the conventional form.

In experiment, we can only collect a finite number of speckles and use the ensemble average to approximate the contrast. Hence, the contrast square calculated from one camera frame $\hat{\gamma}^2$ is a statistical estimation:

$$\hat{\gamma}^2 = \frac{\langle (S_r - \langle S_r \rangle)^2 \rangle_{finite}}{\langle S_r \rangle_{finite}}. \tag{6.15}$$

Here, $\langle \cdot \rangle_{finite}$ denotes the ensemble average over the finite speckles in one camera frame. Therefore, both the numerator and denominator of the contrast square $\hat{\gamma}^2$ are estimated from the finite speckles. To evaluate the accuracy of the estimation, we need to estimate the errors of both numerator and denominator in Eq. 6.15.

Given a random variable X, if we use a sample average $1/N_{independent} \sum_{i=1}^{N_{independent}} X_i$ with $N_{independent}$ independent measurements to estimate its expected value $\langle X \rangle$, the error between the sample average and the expected value is about $\sqrt{V(X)/N_{independent}}$, where $V(\cdot)$ denotes the variance of the random variable X. In our calculation, $N_{independent}$, the number of independent measurements (NIM) in spatial ensemble method, is the number of speckle grains in the camera frame, which is termed $M_{spatial}$.

Let us first calculate the variance of the numerator (γ_{up}^2) of the γ^2. The variance of γ_{up}^2 is

$$\begin{aligned} V(\gamma_{up}^2) &= \langle (S_r - \langle S_r \rangle)^4 \rangle - \langle (S_r - \langle S_r \rangle)^2 \rangle^2 \\ &= \alpha^4 \int_0^T \int_0^T \int_0^T \int_0^T \langle \tilde{I}_r(t_1) \tilde{I}_r(t_2) \tilde{I}_r(t_3) \tilde{I}_r(t_4) \rangle \, dt_1 dt_2 dt_3 dt_4 \\ &\quad - \alpha^2 \langle \int_0^T \int_0^T \tilde{I}_r(t_1) \tilde{I}_r(t_2) dt_1 dt_2 \rangle \, . \end{aligned} \tag{6.16}$$

The first term in the above equation takes the expected value of four random variables multiplied together. If $\hat{I}_r$ is a Gaussian random variable, the bracket can be expanded as

$$\begin{aligned} &\langle \tilde{I}_r(t_1) \tilde{I}_r(t_2) \tilde{I}_r(t_3) \tilde{I}_r(t_4) \rangle = \langle \tilde{I}_r(t_1) \tilde{I}_r(t_2) \rangle \langle \tilde{I}_r(t_3) \tilde{I}_r(t_4) \rangle \\ &+ \langle \tilde{I}_r(t_1) \tilde{I}_r(t_3) \rangle \langle \tilde{I}_r(t_2) \tilde{I}_r(t_4) \rangle + \langle \tilde{I}_r(t_1) \tilde{I}_r(t_4) \rangle \langle \tilde{I}_r(t_2) \tilde{I}_r(t_3) \rangle \, . \end{aligned} \tag{6.17}$$

Here, even though $\tilde{I}_r$ is not a Gaussian random variable, we still take the formula as an approximation, and this approximation actually holds with tolerable errors based on our experimental results. Equation 6.16 then becomes

$$
\begin{aligned}
V(\gamma_{up}^2) \approx \alpha^4 \int_0^T \int_0^T \int_0^T \int_0^T (&\langle \tilde{I}_r(t_1)\tilde{I}_r(t_2)\rangle \langle \tilde{I}_r(t_3)\tilde{I}_r(t_4)\rangle \\
+ \langle \tilde{I}_r(t_1)\tilde{I}_r(t_3)\rangle &\langle \tilde{I}_r(t_2)\tilde{I}_r(t_4)\rangle + \langle \tilde{I}_r(t_1)\tilde{I}_r(t_4)\rangle \langle \tilde{I}_r(t_2)\tilde{I}_r(t_3)\rangle) dt_1 dt_2 dt_3 dt_4 \\
- \alpha^4 \langle \int_0^T \int_0^T \tilde{I}_r(t_1)\tilde{I}_r(t_2) dt_1 dt_2 \rangle^2 & \\
= 2\alpha^4 \langle \int_0^T \int_0^T \tilde{I}_r(t_1)\tilde{I}_r(t_2) dt_1 dt_2 \rangle^2 &= 2(\gamma_{up}^2)^2.
\end{aligned}
\tag{6.18}
$$

Therefore, if there are $M_{spatial}$ independent speckles in spatial ensemble methods, the numerator of $\hat{\gamma}_{up}^2$ has a form of

$$
\hat{\gamma}_{up}^2 = \gamma_{up}^2 \pm \frac{\sqrt{2}\gamma_{up}^2}{\sqrt{M_{spatial}}} = \gamma_{up}^2 (1 \pm \sqrt{\frac{2}{M_{spatial}}}). \tag{6.19}
$$

Here, the term after the ± denotes the standard error of the statistical estimation.

Next, let us calculate the error of the denominator (γ_{down}) of γ. It is simply

$$
\sqrt{\frac{V(S_r)}{M_{spatial}}} = \sqrt{\frac{\langle (S_r - \langle S_r \rangle)^2 \rangle}{M_{spatial}}} = \sqrt{\frac{\gamma_{up}^2}{M_{spatial}}}. \tag{6.20}
$$

Therefore, the denominator $\hat{\gamma}_{down}^2$ has a form of

$$
\hat{\gamma}_{down}^2 = (\gamma_{down} \pm \sqrt{\frac{\gamma_{up}^2}{M_{spatial}}})^2 \approx \gamma_{down}^2 \pm \frac{2\gamma_{up}\gamma_{down}}{\sqrt{M_{spatial}}}. \tag{6.21}
$$

Finally, by combining equations 6.15, 6.19, and 6.21, the expression of the estimation of $\hat{\gamma}^2$ is

$$
\begin{aligned}
\hat{\gamma}^2 = \frac{\hat{\gamma}_{up}^2}{\hat{\gamma}_{down}^2} &\approx \frac{\gamma_{up}^2}{\gamma_{down}^2} (1 \pm \sqrt{\frac{1}{M_{spatial}}} \sqrt{2 + \frac{4\gamma_{up}^2}{\gamma_{down}^2}}) \\
&= (\frac{\tau}{T} + \frac{1}{N_T})(1 \pm \sqrt{\frac{1}{M_{spatial}}} \sqrt{2 + 4(\frac{\tau}{T} + \frac{1}{N_T})}).
\end{aligned}
\tag{6.22}
$$

Hence, the estimation of the contrast is

$$
\hat{\gamma} = \sqrt{\frac{\tau}{T} + \frac{1}{N_T}} (1 \pm \frac{1}{2} \sqrt{\frac{1}{M_{spatial}}} \sqrt{2 + 4(\frac{\tau}{T} + \frac{1}{N_T})}). \tag{6.23}
$$

In SVS, we usually set the camera exposure T much greater than the decorrelation time τ, e.g., $T >> \tau$, and the number of photons collected by one camera pixel N_T

is also much greater than 1, e.g., $N_T >> 1$. In this case, in the above equation, the second term in the second square root in the error part can be dropped and the estimation of the contrast square $\hat{\gamma}$ can be approximated as

$$\hat{\gamma} = \sqrt{\frac{\tau}{T} + \frac{1}{N_T}}(1 \pm \sqrt{\frac{1}{2M_{spatial}}}). \tag{6.24}$$

Rewriting the above equation, we have

$$\tau = T\hat{\gamma}^2(1 \pm \sqrt{\frac{1}{2M_{spatial}}}) - \frac{T}{N_T}. \tag{6.25}$$

The SNR of the decorrelation time in spatial ensemble methods is

$$\begin{aligned} SNR_{spatial} &= \frac{\tau}{err(\tau)} = \frac{\tau}{T\hat{\gamma}^2\sqrt{\frac{1}{2M_{spatial}}}} \\ &= \frac{1}{1 + \frac{T}{\tau N_T}}\sqrt{\frac{M_{spatial}}{2}}. \end{aligned} \tag{6.26}$$

Here, $err(\tau)$ is the standard error of τ, which is equal to $T\hat{\gamma}^2\sqrt{\frac{1}{2M_{spatial}}}$. As we define N_τ as the number of photoelectrons on each camera pixel per time interval τ, we find $N_\tau = \frac{N_T}{T}\tau$. The above Eq. 6.26 can be simplified as

$$SNR_{spatial} = \frac{1}{\sqrt{2}}\frac{1}{1 + \frac{1}{N_\tau}}\sqrt{M_{spatial}}. \tag{6.27}$$

SNR of decorrelation time measurements in temporal sampling methods

In temporal sampling methods, a fast photodetector with a sufficient bandwidth, such as a single-photon-counting-module (SPCM), is used to well sample the temporal trace $I_r(t)$, and the decorrelation time τ is computed from the intensity correlation function $G_2(t)$:

$$G_2(t) = \frac{1}{T}\alpha^2 \int_0^T I_r(t_1)I_r(t_1 - t)dt_1. \tag{6.28}$$

In practice, the correlation is performed between the mean-removed intensity fluctuation:

$$\tilde{G}_2(t) = \frac{1}{T}\alpha^2 \int_0^T \tilde{I}_r(t_1)\tilde{I}_r(t_1 - t)dt_1, \tag{6.29}$$

where $\tilde{G}_2(t)$ denotes the intensity correlation function of the two mean-removed intensity traces, $\tilde{I}_r(t)$ is the AC part of the intensity fluctuation, t_1 is the time variable for integral, and t is the time offset between the two intensity traces.

By substituting Eq. 6.4 into Eq. 6.29, we have

$$\tilde{G}_2(t) = \frac{1}{T}\alpha^2 \int_0^T [\tilde{I}_{r,S}(t_1) + n(t_1)][\tilde{I}_{r,S}(t_1 - t) + n(t_1 - t)]dt_1. \tag{6.30}$$

The expected value of $\tilde{G}_2(t)$ is

$$\langle \tilde{G}_2(t) \rangle = \alpha^2 I_0^2 g_S(t) + \alpha^2 \langle n^2 \rangle g_n(t). \tag{6.31}$$

Same as the definition before, $g_S(t)$ is the correlation function of the mean-removed signal light intensity, and $g_n(t)$ is the correlation function of noise.

When we use the finite time average to estimate the expected value of $\tilde{G}_2(t)$, we need to calculate the variance of $\tilde{G}_2(t)$:

$$\begin{aligned}
V[\tilde{G}_2(t)] &= \frac{1}{T}(\langle \tilde{G}_2(t)^2 \rangle - \langle \tilde{G}_2(t) \rangle^2) \\
&= \frac{1}{T} \langle \int_0^T \int_0^T \alpha^4 \tilde{I}_r(t_1)\tilde{I}_r(t_1 - t)\tilde{I}_r(t_2)\tilde{I}_r(t_2 - t)dt_1 dt_2 \rangle - \frac{1}{T^2} \langle \tilde{G}_2(t)^2 \rangle^2 \\
&\approx \frac{2\alpha^4}{T^2} \int_0^T \int_0^T \langle \tilde{I}_r(t_1)\tilde{I}_r(t_2) \rangle^2 dt_1 dt_2 \\
&= \frac{2\alpha^4}{T^2} \int_0^T \int_0^T [I_0^2 g_S(t) + \langle n^2 \rangle g_n(t)]^2 dt_1 dt_2 \\
&\approx 2(\alpha^4 I_0^4 \frac{\tau}{2T} + \alpha^3 I_0^3 \frac{1}{T} + \alpha^2 I_0^2 \frac{1}{T\tau_n}).
\end{aligned} \tag{6.32}$$

Hence, if we calculate the correlation function $\tilde{G}_2(t)$ by using a finite long measurement trace and use it to estimate $\langle \tilde{G}_2(t) \rangle$, we have the following estimation form

$$\begin{aligned}
\tilde{G}_2(t) &= \langle \tilde{G}_2(t) \rangle \pm \sqrt{V[\tilde{G}_2(t)]} \\
&= [\alpha^2 I_0^2 g_S(t) + \alpha^2 \langle n^2 \rangle g_n(t)] \pm \sqrt{2(\alpha^4 I_0^4 \frac{\tau}{2T} + \alpha^3 I_0^3 \frac{1}{T} + \alpha^2 I_0^2 \frac{1}{T\tau_n})}.
\end{aligned} \tag{6.33}$$

Since $g_n(t)$ usually has much shorter decorrelation time compared to $g_S(t)$, to estimate the speckle decorrelation time τ, we can use the part of the correlation curve where $g_n(t)4$ drops close to 0 while $g_S(t)$ is still close to unity. In this case,

the part of the the correlation curve $\hat{G}_2(t)$ is

$$\begin{aligned}\hat{G}_2(t) &= [\alpha^2 I_0^2 g_S(t) \pm \sqrt{2(\alpha^4 I_0^4 \frac{\tau}{2T} + \alpha^3 I_0^3 \frac{1}{T} + \alpha^2 I_0^2 \frac{1}{T\tau_n})} \\ &= \alpha^2 I_0^2 [g_S(t) \pm \sqrt{2(\frac{\tau}{2T} + \frac{1}{\alpha I_0 T} + \frac{1}{\alpha^2 I_0^2 T\tau_n})}].\end{aligned} \tag{6.34}$$

In the experiment, τ_n can be approximated as the inverse of the detector bandwidth, or equivalently the time interval ΔT between two data points. In the following calculation, we will substitute τ_n by ΔT.

When we use the decorrelation curve to estimate a parameter associated with the curve, such as decorrelation time, there exist different fitting models to retrieve the parameter. Here, for simplicity, the estimated decorrelation time $\hat{\tau}$ can be chosen by taking the time point where the decorrelation curve drops to $1/e$. In this case, the error of the estimated decorrelation time $err(\tau)$ is

$$\begin{aligned}err(\tau) &= \frac{1}{|\frac{dg_S}{dt}|_{g_S(t)=1/e}|} \sqrt{2(\frac{\tau}{2T} + \frac{1}{\alpha I_0 T} + \frac{1}{\alpha^2 I_0^2 T\Delta T})} \\ &= \frac{e}{2}\tau \sqrt{2(\frac{\tau}{2T} + \frac{1}{\alpha I_0 T} + \frac{1}{\alpha^2 I_0^2 T\Delta T})}.\end{aligned} \tag{6.35}$$

Hence, the decorrelation time τ can be estimated from the calculated decorrelation time τ as

$$\tau = \hat{\tau}(1 \pm \frac{e}{\sqrt{2}} \sqrt{\frac{\tau}{2T} + \frac{1}{\alpha I_0 T} + \frac{1}{\alpha^2 I_0^2 T\Delta T}}). \tag{6.36}$$

The SNR of the decorrelation time in temporal sampling methods is

$$SNR_{temporal} = \frac{\tau}{err(\tau)} = \frac{\sqrt{2}}{e} \frac{1}{\sqrt{\frac{\tau}{2T} + \frac{1}{\alpha I_0 T} + \frac{1}{\alpha^2 I_0^2 T\Delta T}}}. \tag{6.37}$$

As defined in the main text, the NIM in temporal domain methods $M_{temporal} = \frac{2T}{\tau}$, and taking the fact that $\alpha I_0 T = \frac{1}{2} M_{temporal} N_\tau$, the SNR equation 6.37 can be rewritten as

$$SNR_{temporal} = \frac{\sqrt{2}}{e} \frac{1}{\sqrt{1 + \frac{2}{N_T} + \frac{2}{N_T^2}\frac{\tau}{\Delta T}}} \sqrt{M_{temporal}}. \tag{6.38}$$

References

[1] D. J. Pine, D. A. Weitz, P. M. Chaikin, and E. Herbolzheimer. Diffusing wave spectroscopy. *Physical Review Letters*, 60(12):1134–1137, March 1988.

[2] Jörg Stetefeld, Sean A. McKenna, and Trushar R. Patel. Dynamic light scattering: a practical guide and applications in biomedical sciences. *Biophysical Reviews*, 8(4):409–427, October 2016.

[3] Theodore J. Huppert, Solomon G. Diamond, Maria A. Franceschini, and David A. Boas. HomER: a review of time-series analysis methods for near-infrared spectroscopy of the brain. *Applied Optics*, 48(10):D280, March 2009.

[4] Gerard M. Ancellet and Robert T. Menzies. Atmospheric correlation-time measurements and effects on coherent doppler lidar. *Journal of the Optical Society of America A*, 4(2):367, February 1987.

[5] D. A. Boas, L. E. Campbell, and A. G. Yodh. Scattering and imaging with diffusing temporal field correlations. *Physical Review Letters*, 75(9):1855–1858, August 1995.

[6] Turgut Durduran and Arjun G. Yodh. Diffuse correlation spectroscopy for non-invasive, micro-vascular cerebral blood flow measurement. *NeuroImage*, 85:51–63, January 2014.

[7] T. Durduran, R. Choe, W. B. Baker, and A. G. Yodh. Diffuse optics for tissue monitoring and tomography. *Reports on Progress in Physics*, 73(7):076701, June 2010.

[8] Shuai Yuan, Anna Devor, David A. Boas, and Andrew K. Dunn. Determination of optimal exposure time for imaging of blood flow changes with laser speckle contrast imaging. *Applied Optics*, 44(10):1823, April 2005.

[9] Mingjun Zhao, Chong Huang, Daniel Irwin, Siavash Mazdeyasna, Ahmed Bahrani, Nneamaka Agochukwu, Lesley Wong, and Guoqiang Yu. EMCCD-based speckle contrast diffuse correlation tomography of tissue blood flow distribution. In *Biophotonics Congress: Biomedical Optics Congress 2018 (Microscopy/Translational/Brain/OTS)*. OSA, 2018.

[10] Andrew K. Dunn, Hayrunnisa Bolay, Michael A. Moskowitz, and David A. Boas. Dynamic imaging of cerebral blood flow using laser speckle. *Journal of Cerebral Blood Flow & Metabolism*, 21(3):195–201, March 2001.

[11] David A. Boas and Andrew K. Dunn. Laser speckle contrast imaging in biomedical optics. *Journal of Biomedical Optics*, 15(1):011109, 2010.

[12] A. J. F. Siegert. On the fluctuations in signals returned by many independently moving scatterers, Radiation Laboratory, Massachusetts Insitute of Technology, 1943.

[13] R. Bandyopadhyay, A. S. Gittings, S. S. Suh, P. K. Dixon, and D. J. Durian. Speckle-visibility spectroscopy: a tool to study time-varying dynamics. *Review of Scientific Instruments*, 76(9):093110, September 2005.

[14] Ichiro Inoue, Yuya Shinohara, Akira Watanabe, and Yoshiyuki Amemiya. Effect of shot noise on x-ray speckle visibility spectroscopy. *Optics Express*, 20(24):26878, November 2012.

[15] Andrew K. Dunn. Laser speckle contrast imaging of cerebral blood flow. *Annals of Biomedical Engineering*, 40(2):367–377, November 2011.

[16] Robert Zwanzig and Narinder K. Ailawadi. Statistical error due to finite time averaging in computer experiments. *Physical Review*, 182(1):280–283, June 1969.

[17] Joseph W. Goodman. *Speckle Phenomena in Optics*. Viva Books Private Limited, 2008.

[18] Detian Wang, Ashwin B. Parthasarathy, Wesley B. Baker, Kimberly Gannon, Venki Kavuri, Tiffany Ko, Steven Schenkel, Zhe Li, Zeren Li, Michael T. Mullen, John A. Detre, and Arjun G. Yodh. Fast blood flow monitoring in deep tissues with real-time software correlators. *Biomedical Optics Express*, 7(3):776, February 2016.

[19] Wenjun Zhou, Oybek Kholiqov, Shau Poh Chong, and Vivek J. Srinivasan. Highly parallel, interferometric diffusing wave spectroscopy for monitoring cerebral blood flow dynamics. *Optica*, 5(5):518, April 2018.

[20] J. Xu, A. K. Jahromi, J. Brake, J. E. Robinson, and C. Yang. Interferometric speckle visibility spectroscopy (isvs) for human cerebral blood flow monitoring, 2020. eprint: `arXiv:2009.00002`.

INDEX